Doctoral Dissertation
Doctoral Program in Material Science and Technology (34th Cycle)

Make it greener: Exploring novel biobased materials in photopolymerization processes

Camilla Noè

Supervisor(s):

Prof. Marco Sangermano, Supervisor, Politecnico di Torino, Department of Applied Science and Technology, Torino, Italy
Prof. Minna Hakkarainen, Co-Supervisor, KTH Royal Institute of Technology, Department of Fibre and Polymer Technology, Stockholm, Sweden

Doctoral Examination Committee:

Prof. Alberto Jiménez-Suárez, Rey Juan Carlos University, Materials Science and Engineering Area, Móstoles, Spain, (Referee)
Prof. Paula Bosch, Spanish National Research Council, Instituto de Ciencia y Tecnología de Polímeros, Madrid, Spain, (Referee)
Prof. Galder Kortaberria, University of the Basque Country, Chemical and Environmental Engineering Department, San Sebastian, Spain
Prof. Yves Leterrier, Ecole Polytechnique Fédérale de Lausanne, EPFL, Lausanne, Switzerland
Prof. Sabrina Grassini, Politecnico di Torino, Department of Applied Science and Technology, Torino, Italy

Politecnico di Torino
2022

Declaration

I hereby declare that the contents and organization of this dissertation constitute my own original work and does not compromise in any way the rights of third parties, including those relating to the security of personal data.

Camilla Noè

Turin, 2022

* This dissertation is presented in partial fulfillment of the requirements for **Ph.D. degree** in the Graduate School of Politecnico di Torino (ScuDo).

I would like to dedicate this thesis to my loving parents, beloved sister, and sweetest grandmother.

In memory of Mario Noè, Lucia Pinto and Enrico Ciocatto

Acknowledgment

I would like to express my deepest thanks to my supervisor Marco Sangermano. Thank you for giving me the opportunity to work with you and for guiding me during these years. Your passion for the photopolymerization processes and your commitment to different projects have been inspiring to me. Thank you for all our discussions which helped me understand my weak and strong points and for all the tips that to give me, I will treasure them.

I would also like to express my deep gratitude to my co-supervisor Minna Hakkarainen, who kindly hosted me in her department making me feel part of the group already from the first day. Thanks for your wise scientific inputs that have widened my knowledge in polymer chemistry.

I would like to thank Andrea Cosola for his unconditional support. Thanks for your patience and for always having faith in me. You are always by my side and there when I need help. You have been amazing!

I would like to thank my best friends Greta Masserano and Giulia Santopolo for all the help and friendship you gave me during these years. Our video call really saved me.

Special thanks to my family that always supported me. Thanks for all the unconditional love and patience. Your presence is what sustained me this far.

Thanks to my closest friends/ co-workers for having accompanied me through this journey: Lorenzo Vigna, Matteo Caprioli, Marina D'Aloisio, Luisa Baudino and Marco Franzoso.

I would also thank all the following people that helped me during these years:

My friends and collegues: Ignazio Roppolo, Ying Zhang, Leonardo Iannucci, Martina Cattaruzza, Elisa Gaggero, Annalisa Chiappone, Stefano Gazzotti, Irene Carmagnola, Chiara Tonda-Turo, Michael Zanon, Lorenzo Pezzana, Angelo

Romano, Simone Lantean, Andrea Baggio, Matteo Turani, Alberto Giubilini, Carlo Trentalange, Daniele Testore, Cristian Mendes, Simone Garino, Leila Es Sebar and Alessio Truncali.

My Swedish friends and co-workers: Wenxian Xuan, Maria Iggarded, Erik Landberg, Jowan Rostami, Niklas Wahlmstrong, Karin Adolfsson, Charalampos Pronotis, Linnea Cederholm, Jenevieve Gocheco Yao, Zhaoxuan Feng, Martin Sterner, and Astrid Ahlinder.

Abstract

In a continuously evolving world, the invention of plastics can be considered one of the greatest revolutions. From their first discovery, it was clear that polymers can replace different natural materials like wood, stones, and metals since they are lightweight, strong, and flexible and can be shaped in many ways. Over time, polymers have progressively changed how we live, playing, nowadays, a fundamental role in our life. For those reasons, plastic production has exponentially increased over the years and it is expected to overcome 400 million metric tons in 2022. Unfortunately, their production is causing increasing environmental concern due to the high greenhouse emission and toxic products released into the water, soil, and air giving rise to potential threats to human health. Therefore, many scientists are currently working to find greener and more sustainable replacements for fossil-fuel-based polymers. Among the available substituted, biobased polymers stand out since they are based on renewable resources and their production can have lower CO_2 impact. Currently, the biobased market is dominated by thermoplastic while there remains a huge need for the development of green thermosets.

In this context, this thesis presents the development of new biobased thermosetting polymers by means of the UV-curing process.

Chapter 1 presents a brief introduction to biobased polymers and the most common photopolymerization techniques, while the experimental part, which represents the main body of the thesis, is divided into three major topics: UV-

curable starch-based hydrogels and organo/hydrogels (Chapter 2), Biobased UV-curable coatings (Chapter 3) and Biobased UV-curable composites (Chapter 3).

The first experimental work focuses on the modification of maize starch with methacrylic groups to make it light processable. The obtained methacrylated starch (MA-Starch) was initially used to produce photocrosslinkable hydrogels that can be 3D-printed *via* a digital light processing (DLP) printer and have good cell cytocompatibility, therefore they possess promising applicability in tissue engineering and as cell carriers (Chapter 2.1). Subsequently, the MA-Starch was mixed with acrylated cyclodextrin to produce a new class of UV-curable bio-sorbents for the removal of methylene blue from wastewater (Chapter 2.2).

The second experimental work is based on the development of UV-curable biobased coatings. This work is divided into two sections; the first one is focused on the investigation of cationically photocurable epoxy-based coatings, while the second one is based on radical photocurable methacrylate-based coatings.

In the initial part of the chapter, the reactivity and the mechanical properties of three different biobased epoxy monomers deriving from phloroglucinol, vanillin, and castor oil are investigated (3.1.2). Then the possibility to successfully UV-cure three different epoxy cardanols derivatives is presented. The mechanical properties of the obtained thermosets were analyzed considering the chemical structures of the monomer (3.1.3). Subsequently, 12 epoxidized vegetable oils (EVOs), derived from different resources and differing according to their glycidyl index, were selected and crosslinked. The scope of this investigation was to demonstrate the existence of a correlation between the number of epoxy rings and the final thermo-mechanical properties of the thermosets (3.1.4). Further developments of this study are then presented. Moreover, the influence of the starting glycidyl index on the metal adhesion and corrosion protection effectiveness of three EVO- based coatings is analyzed in section 3.1.5.

The second part of Chapter 3 is dedicated to the study of UV-curable MA-starch films. The obtained films possess a high adhesion to glass and are biodegradable. Their biodegradability was assessed by studying the enzymatic degradation of the coatings by α-amylase from *Bacillus licheniformis* (3.2.1).

Chapter 4 presents the last experimental work that was conducted, which was based on the study of two different classes of fully biobased composites. The first class consists of the DLP 3D-printing of acrylated soybean oil composites, reinforced with a lignocellulose waste derived from the macadamia nut industry. The cytotoxicity, adhesion and cell proliferation with human fibroblast cells of the 3D-printed objects were investigated to demonstrate their suitability as scaffolds for bioengineering purposes (4.2). The second part of Chapter 4 instead concerns the radical induced cationic frontal photopolymerization (RICFP) of diglycidylether of vanillyl alcohol, reinforced with two types of fabric mats: unidirectional non-woven cellulose fibers and flax woven fibers. The RICFP reaction considerably reduced the curing time and thus improved the efficiency of composite fabrication. Moreover, the mechanical properties of these fully bio-based composites were compared with the one obtained by other epoxy composites that were RICFP cured with a petroleum-based resin and reinforced with the same biobased fabrics (4.3).

Altogether the results presented in this manuscript show new possible strategies to produce and expand the biobased thermosetting polymer field.

Table of contents

First Chapter

1 General Introduction

1.1 What are biobased materials and why do we need them?

The term *bio* is a Greek word whose translation means *life*. Thus, the term refers to materials composed or derived from biomass, which include forest, agricultural waste and aquatic plants [1].

Among biobased materials, biobased polymers are attracting widespread interest as an alternative to petroleum-based resins due to increasing environmental concern and the depletion of crude oil. In fact, polymer production is dramatically increasing over the years (Fig. 1.1,a) and by 2050, it is expected to account the 20% of worldwide fossil fuel consumption [2]. Therefore, the use of biobased polymers can represent a green alternative since they are based on renewable resources and can possess low CO_2 emissions. However, it is important to stress that the term *biobased* does not include biodegradability in its definition, therefore not every biobased polymer are biodegradable (Fig.1.1,b). Many studies in recent years have focused on bipolymers as confirmed by the increasing amount of publication recorded on the Web of Science and by the high numbers of legislation favouring biobased products [3].

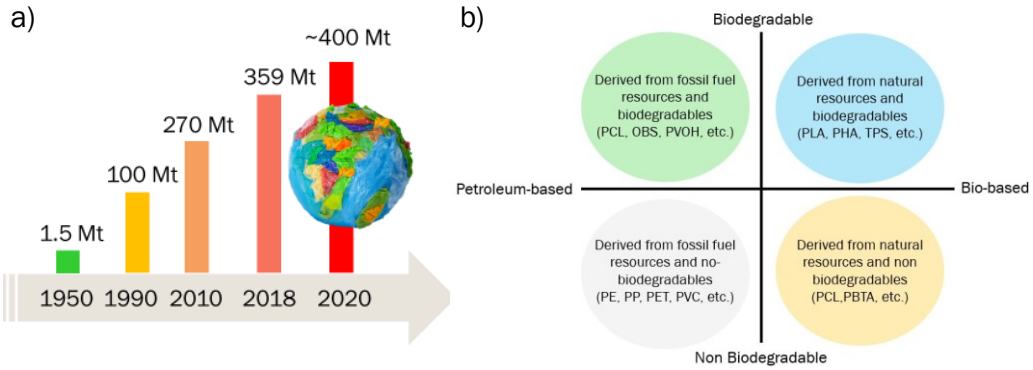

Figure 1.1: a) worldwide annual production of plastics from 1950 to 2020 [4]; b) worldwide production of bioplastics by material type.

However, as can be observed in Fig.1.2, the current biobased polymer market is dominated by thermoplastics which are made of polymer chains non-covalently bounded. While, the market of thermosetting polymers, consisting of covalently bonded chains, is still limited. Therefore, the development of biobased thermosets still represents a great challenge for both industry and academics.

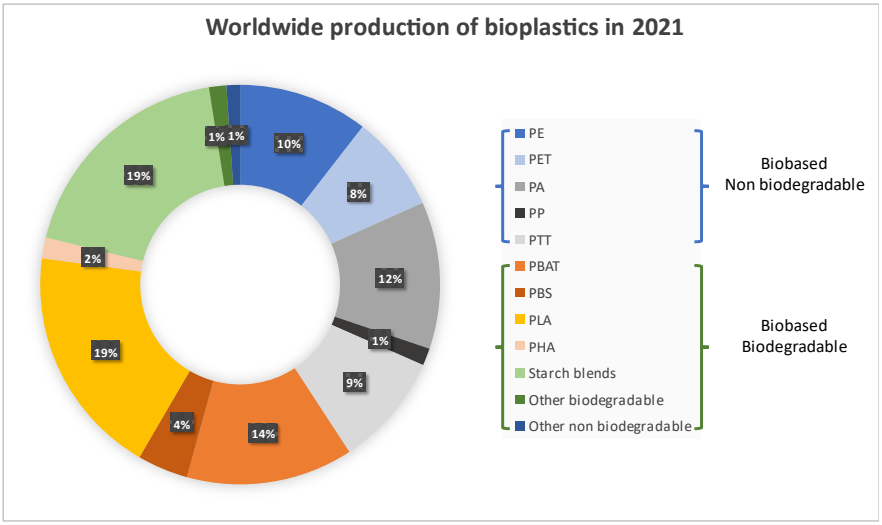

Figure 1.2: The worldwide production of bioplastics by material type [5].

Thermosets are usually formed by liquid monomers or comonomers containing at least two reactive units which can crosslink among themselves after the addition of an external energy source such as heat or light. Among the conventional curing processes, the photocrosslinking one can be considered the greenest since it possesses high curing speed, absence of VOC (Volatile Organic Compound) emission and low energy consumption [6–8].

In this context, this thesis work will focus on the development of different ultraviolet (UV) curable biobased thermosetting polymers and composites deriving from different biorenewable resources.

1.2 Photo-crosslinking processes

In recent decades photopolymerization processes have gained increasing interest as a useful industrial technology due to its remarkable benefits like high productivity, low energy consumption with no heating requirements and high surface quality. Moreover, this technique allows the use of solvent-free resins. At the beginning of the 21st century, several governments applied rigid regulation control on the VOC emission, since those substances can cause air pollution and health problems. Therefore, the photocrosslinking processes, with no hazardous substance emission, started to become very attractive in different fields like paper, coatings, dentistry, resists and printing. In order to start the photopolymerization reaction a photoactive compound called photoinitiator (PhI) has to be added into the formulation. The PhIs are substances able to absorb the light and subsequently generate reactive species. The wavelength range usually used in the photopolymerization processes covers the UV or visible range (Fig.1.3,a) but also other energy sources have been reported like infrared light, X-ray and electron beam [9–11]. The choice of the light wavelength depends on the selected application, for example, UV light is often used in the coatings industry, while visible light is preferred in dental applications. In order to be efficient, a PhI must have a high extinction coefficient which represents its probability to absorb the light in the wavelength of interest [12]. The initiation rate and the light penetration depth depends on the type of PhI. As soon as the PhI absorb the photon, it enters an excited state which can lead to the initiation step. However, while the PhI is in the excited state some quenching mechanisms can take place due to the presence of other components in the formulation or to the oxygen present in the atmosphere as described in the modified Jablonski diagram (Fig.1.3,b). Therefore, an efficient PhI must have an excited state with a short lifetime and a high quantum yield (defined as the ratio of the number of converted photoinitiators to the number of photons absorbed by the initiator) [13].

The photopolymerization processes can be classified into two main categories: radical and cationic depending on the type of active propagating centre. Those processes will be presented in detail in the following sections.

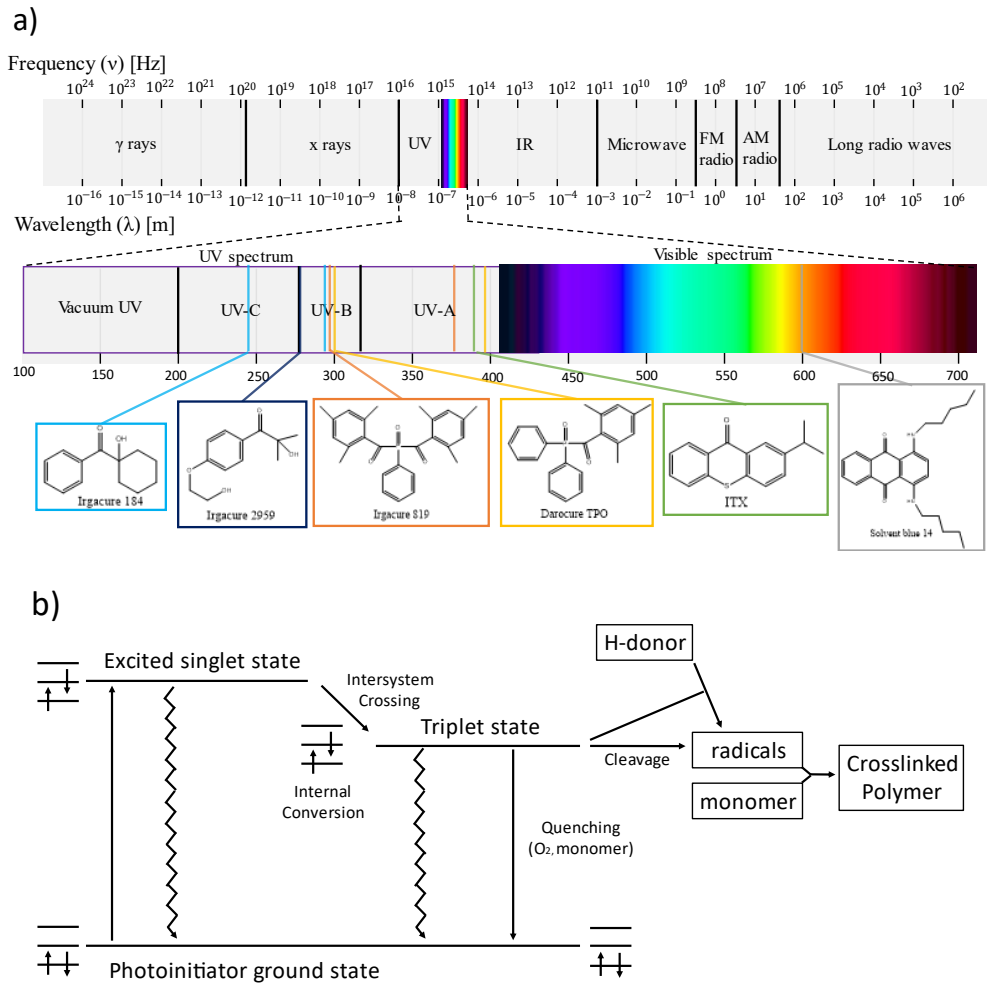

Figure 1.3: a) Wavelength spectrum and most common photoinitiators with thei their major absorption peaks, b) Types of deactivation mechanism of the excited state of the PhI.

1.2.1 Radical UV-curing

Nowadays, the majority of commercially available photocurable resins are based radical photopolymerization which was also the first photopolymerization technique developed. In fact, the first photo-induced reaction leading to the formation of a polymer was reported by Hoffmann, who described the radical photopolymerization of the vinyl bromide in 1860. Subsequently, different PhIs were evaluated to enhance the initiation efficiency of the reaction, like ketones, aldehydes and halogen compounds [14]. The radical photopolymerization proceeds via a chain-growth mechanism mainly involving acrylates and methacrylates, except for the thiol-ene radical reaction which instead proceeds through a step-grow mechanism. The main reason for the use of (meth)acrylates is their extremely fast reactivity. Nevertheless, the methacrylates are usually less reactive than the

acrylates but they are considered less hazardous [15]. The chain-grow mechanism is reported in Fig.1.4., in which *M* represents the monomer and *R·* the radical. As can be observed in Fig.1.4, as PhI absorbs the light energy (*hv*) it will pass into an excited state and generate the initial radical by decomposing. Those radicals will subsequently react with the monomers to initiate the polymerization. Subsequently, the addition of different monomers to the growing macroradical induce the formation of the polymer chains (propagation step). Finally, the reaction terminates with either a mono or bimolecular addition [15]. Interestingly, it is also possible to have unterminated chains trapped into the crosslinked network that can react with other reactive species able to diffuse into the polymer like oxygen.

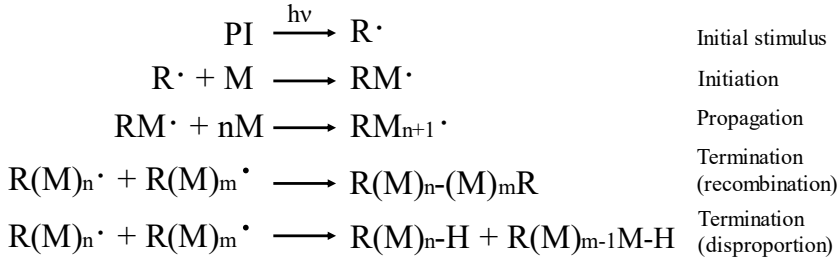

Figure 1.4: Main reactions steps of the radical photopolymerization.

The main drawback of the radical photopolymerization is oxygen inhibition especially for coatings that possess a high surface area. Oxygen can react with the propagating radical forming peroxy radical that terminate the chain growth since it has low reactivity with other monomers. Different methods exist to minimize this problem; 1) an inert atmosphere can be used to avoid the presence of oxygen during the UV-curing, 2) increasing the amount of photoinitiator or the lamp intensity in order to reduce the oxygen diffusion (minimize the light exposure), 3) perform the reaction in water or using an oxygen barrier like wax [16].

1.2.1.1 Radical photoinitiators

In PhIs used in radical (also called free-radical) photopolymerization can be classified into two main categories: Norrish type I and Norrish type II. The light irradiation causes a unimolecular direct bond cleavage in the Norrish type I PhIs, while a bimolecular hydrogen abstraction in the Norrish type II PhIs, in both cases inducing the generation of radicals.

Norrish type I photoinitiators

Norrish type I photoinitiators are unimolecular chromophores that undergo a homolytic bond photocleavage generating free radicals. The first commercialized Norrish type I class of photoinitiators were the benzoin ethers which cleave into benzyl ether radical and benzoyl radical after absorbing the UV-light (Fig.1.5,a). However, formulations containing those PhIs possess a low life pot since the hydrogen of the benzyl ether carbon can be easily abstracted. Therefore, other chromophore compounds were taken into consideration like the ketals. For example, the 2,2-dimethoxy-2-phenylacetophenone possess two advantages over

the benzoin ethers, in fact, it possesses high package stability and after the initial photocleavage leading to the formation of two radicals it undergoes another cleavage leading to the formation of methyl radicals (Fig.1.5,b).

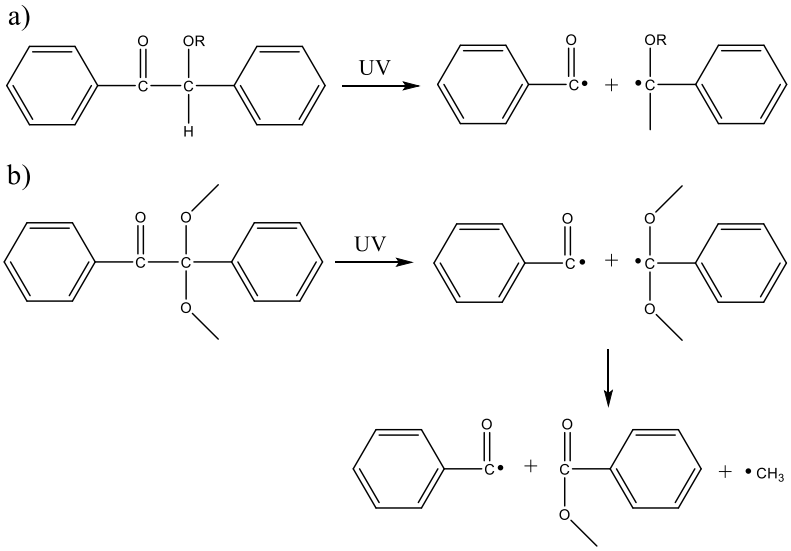

Figure 1.5: a) benzoin ether photocleavage, b) 2,2-dimethoxy-2-phenylacetophenone photocleavage.

Norrish type II photoinitiators

Norrish type II photoinitiators are bimolecular chromophores that can extract hydrogen or electron from a donor after light absorption. Common examples of PhIs belonging to this category are benzophenones, camphorquinone, thioxanthones or dialkyl keynotes (Fig.1.6); while aliphatic amines are common hydrogen donors. This class of PhI is less affected by oxygen inhibition, nevertheless, the excited state of those compounds has a longer life than the Type I PhI, and therefore can be more easily quenched.

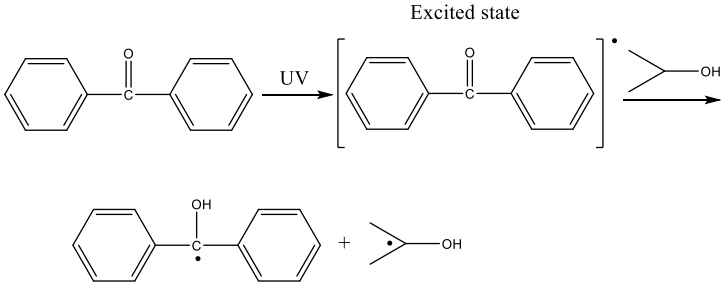

Figure 1.6: Benzophenone photocleavage.

1.2.1.2 Radical UV-curable monomers

As already anticipated before, the radical photopolymerization maily involves (meth)acrylated monomers. The most common are the acrylated polyesters, acrylated polyethers, acrylated polyurethanes, acrylated silicones (Fig.1.7).

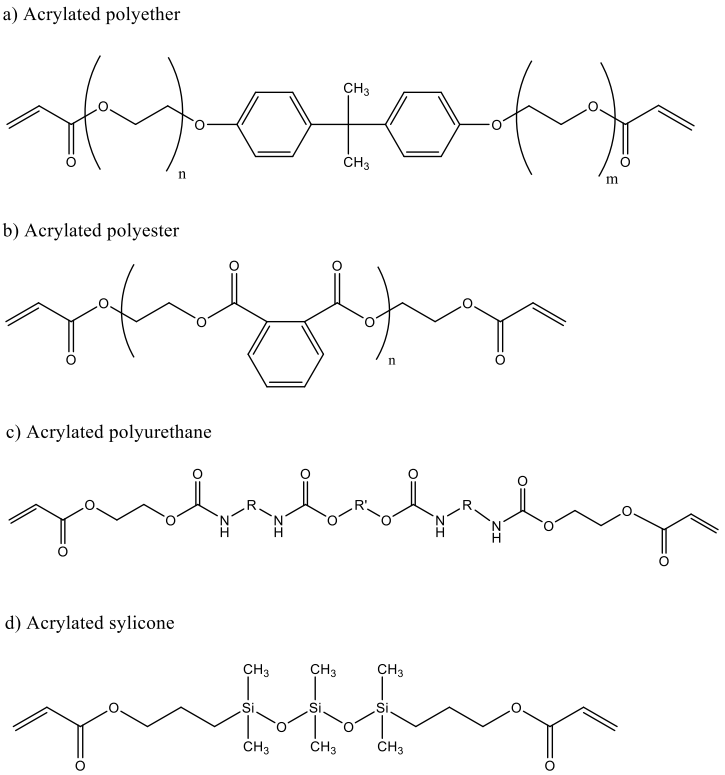

Figure 1.7: Examples of typical acrylated monomers used in free-radical photopolymerization.

Finally, also the thiol-ene system is often used, which is based on an addition stoichiometric reaction between multifunctional thiols and olefins (ene). Those systems are less sensitive to oxygen inhibition but possess an unpleasant smell which hinders their applicability [16].

1.2.2 Cationic UV-curing

This section is based on the review article titled "*Cationic UV-Curing of Epoxidized Biobased Resins*". This article was published in Polymers journal in 2021 (doi.org/10.3390/polym13010089).

Crivello developed the cationic photopolymerization in 1977. Crivello discovered that diaryliodonium salts ($Ar_2I^+MtXn^-$) could generate high acidic solutions when irradiated by UV light. The photolysis of those salts produced Brφnsted acid that could initiate the cationic chain-growth polymerization [17]. The

mechanism of the cationic ring-opening polymerization of epoxides is reported in Fig.1.8.

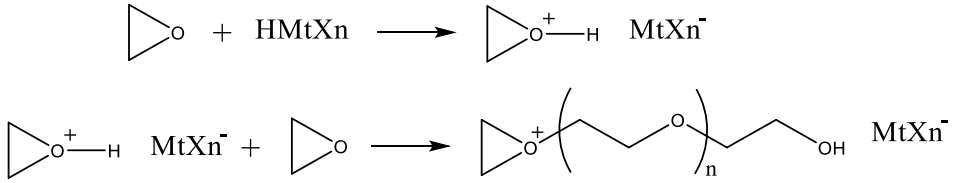

Figure 1.8: mechanism of the cationic ring-opening polymerization of an epoxide.

The cationic UV curing technique has many advantages over the free-radical photopolymerizations, such as:

- It does not require an inert atmosphere during the curing process since it is not affected by oxygen inhibition.
- It can continue after the light source has been removed. This phenomenon, noted as a "dark reaction", can lead to enhanced monomer conversion either in ambient temperature or with a thermal treatment.
- The cationic photocurable monomers are generally not toxic and not irritating.
- The obtained materials are less affected by volume shrinkage upon curing and possess higher thermal resistance [6,8].

1.2.2.1 Cationic photoinitiators

The most used cationic photoinitiators (PhIs) are the onium salts. The onium salts are ionic compounds composed of an organic cation and an inorganic anion. The cationic component absorbs light, so its structure determines the photosensitivity, quantum yield, and the ultimate thermal stability of the salt. The anionic component defines the strength of the generated acid, the initiator efficiency, and the reactivity of the propagating ions pair in the polymerization reaction.

The UV irradiation produces the photoexcitation and, subsequently, the excited singlet state's decay inducing both homolytic and heterolytic cleavages. The most used photoinitiators for photoinduced cationic ring-opening polymerization are diaryliodonium, triarylsulfonium, and dialkyphenacylsulfonium. Their structures are reported in Fig.1.9 where MtXn- represents a weak nucleophilic counterion, such as BF4-, PF6- or SbF6-.

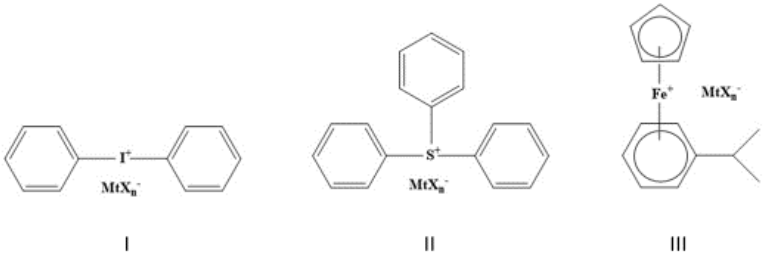

Figure 1.9: Structures of most common cationic photoinitiators.

The simplified photodecomposition of general diaryliodonium salts is shown in Fig.1.10 [18]. The cleavage of the Ar-I bond produces reactive cations, radical-cations, and radicals. Cations and radical-cations react further with proton donor species (solvents or monomers) to form Brønsted-acids, which are the real initiating species [19]. The photolysis of those salts is an irreversible process. The acids photogenerated are called "superacids" since their acidity values in the Hammet scale (H0 values) range from -14 to -30. Higher anionic dimension leads to lower nucleophilicity, and photogeneration of stronger acids. Therefore, even if the anions have no direct role in the photochemistry, their structural dimensions strongly influence the polymerization kinetics [18,20].

Figure 1.10: Simplified photodecomposition of a general diaryliodonium salt.

Generally, the UV activation wavelength region of these photoinitiators ranges from 230 to 300 nm. In order to enhance the performances of the onium salts, different methodologies can be applied:

- Shifting the activation region by introduction of chromophoric groups in the aromatic rings [21].

- Indirect activation of the photoinitiator by free radical oxidation [10,22], electron transfer from a photoexcited molecule and onium salts [23–25], or by the excitation of charge transfer complexes of the salts [26,27].

Another class of photoinitiators is constituted by dialkylphenacylsulfonium salts, that are able to withstand reversible photolysis processes. When irradiated, they form reversible yields and strong Brφnsted acids. The drawback of this reversible system is the short dark polymerization, since in the absence of UV light, the termination reaction rapidly takes place [28,29].

Alkoxypyridinium salts have excellent thermal stability and high solubility [30]. New carbazole scaffold visible light photoinitiator/photosensitizers were recently developed by Lalevée et al. These systems consist of a carbazole unit

connected at two 4,4′-dimethoxydiphenylamine groups in positions 3 and 6 [31]. Other types of onium salts photosensitizers are naphthalene-based compounds. For example, 1-Amino-4-methyl-naphthalene-2-carbonitrile derivatives have been studied by Ortyl as versatile UV and visible light sensitizers [32].

Versace et al. have studied the use of anthraquinone functional phthalocyanine in combination with suitable co-initiators as visible light photoinitiator systems for cationic and free-radical polymerization [33]. The progress in cationic photoinitiators has been in detail analyzed in recent reviews [6,8,34–36].

1.2.2.2 Cationic UV-Curable Monomers

The use of photolatent acids can be exploited to polymerize unsaturated monomers such as vinyl ethers, styrene and N-vinyl carbazole as well as the ring-opening polymerizations of epoxy monomers, cyclic ethers, lactones and cyclic acetals (Fig.1.11). These monomers can polymerize by a cationic chain-growth polymerization mechanism.

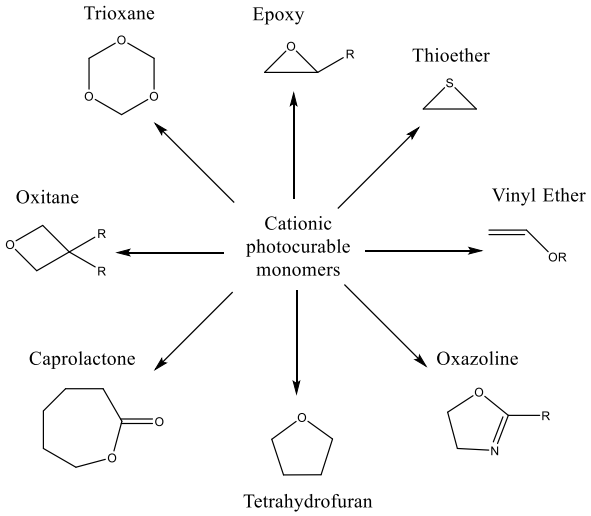

Figure 1.11: Common monomers used in cationic photopolymerization.

Vinyl ether monomers [37,38] were first investigated as a good alternative to the chain growth radical photopolymerization of acrylates because vinyl ethers possess high reactivity, low toxicity and low odour. Nevertheless, under certain conditions, hydrolysis may compete with the polymerization of vinyl ether monomers. The hydrolysis reaction of vinyl ethers with water is catalyzed by the same acid species that catalyze the polymerization reactions.

The commercially most important class of cationically photocurable monomers is nowadays epoxides [39–49] they can undergo cation-induced ring-opening polymerization reaction through an oxiranium ion intermediate. When difunctional epoxides or epoxy-substituted polymers are used as the starting materials, crosslinking readily occurs to generate a three-dimensional polymer network.

Among the different available epoxy monomers, only cycloaliphatic epoxides have reached substantial commercial significance due to their higher reactivity in cationic photopolymerization and also due to excellent adhesion, chemical resistance and mechanical properties of the resulting thermosets.

1.3 Biobased UV-curable building blocks

Among biobased resins, the most used are vegetable oils (VOs) since they are largely available and cheap. Their structure is mainly constituted by triglycerides (90-95%) with different amounts of unsaturation depending on their origin. These unsaturated sites can be easily modified with different types of photocurable functional groups [50] such as epoxy [51] or (meth)acrylated groups [52] (Fig.1.12). However, thermosets deriving from VOs usually possess low mechanical properties due to the presence of flexible aliphatic chains in their structures which limits their usage to non-structural applications. Up to now, VOs have been proposed as matrixes for composites reinforced with cellulose [53], as toughenners in blends with fossil-fuel-based resins [54] and for coatings with good adhesion on steel, glass and alluminium [51]. Interestingly, VOs thermosets are potentially biodegradable since the glycerol ester bonds can be biologically cleaved [55].

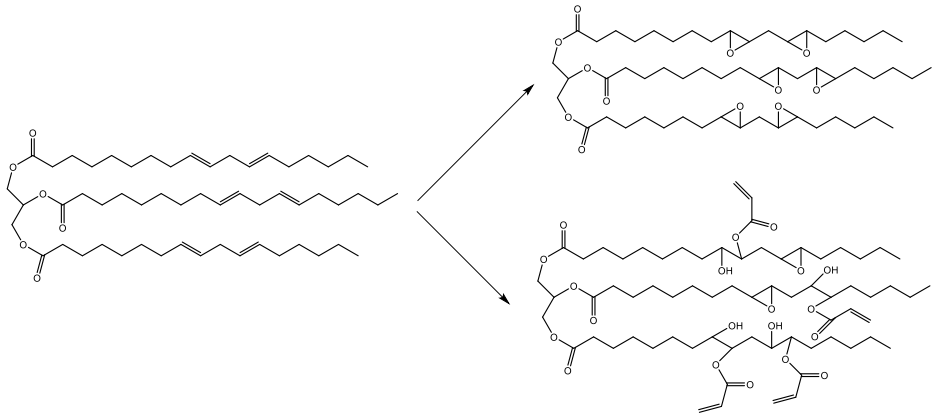

Figure 1.12: Soybean oil structure with two possible modifications.

Another interesting class of biobased feedstock consists of molecules containing rigid backbones like polysaccharides [56] and lignin [57]. The thermosets obtained from those monomers usually show high mechanical properties due to their more rigid structure.

Polysaccharides can derive from different sources like potato, maize (starch, carboxymethylstarch, hydroxypropyl starch), cellulose (carboxymethylcellulose, methylcellulose, etc.), seaweed extracts (alginate, agar, etc.), exoskeleton of crustaceans and insects (chitin, chitosan, etc.), and different types of microbial

gums (xanthan, pullulan, etc.). Different strategies can be used to modify those monomers in order to obtain UV-curable thermosets, which usually possessed superior chemical resistance, mechanical, and thermal properties with respect to the pristine uncured polysaccharides [58]. For example, glycidyl methacrylate, methacrylic anhydride and other vinyl monomers can be used to modify starch, cellulose and chitosan chains to produce UV-curable hydrogels [59–62]. Or glycidyl methacrylate can be grafted on the polysaccharide chains to obtain cationically photocurable coatings (Fig.1.13,a) [63].

Interestingly, not only polysaccharides themselves have been photocured, but also other molecules deriving from them. For example, furanic compounds derived from hemicellulose and cellulose biomass have been successfully epoxidized and cationically photocured to obtain adhesives and coatings (Fig. 1.13,b) [64,65].

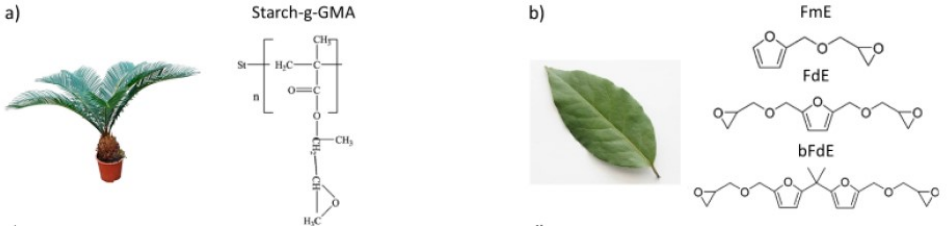

Figure 1.13: examples of a) starch grafted glycidilmethacrylate, b) epoxidized furanic compounds.

Another compound that is recently gaining high interest is lignin which represents around 15 to 30% of wood. The main constituents of lignin are cinnamic alcohols which can be devided in three different main structures: syringyl, p-hydroxyphenyl and guaiacyl, which are formed and conjugated by radical biosynthesis (Fig.1.14,a). However, the specific chemical structure of lignin is still unknown since it does not possess a uniform structure (Fig. 1.14,b) [66]. Lignin have been modified with epoxy and (meth)acrylated groups to make it light processable and subsequently mixed with other photocurable resins to produce coatings with improved mechanical properties [67,68].

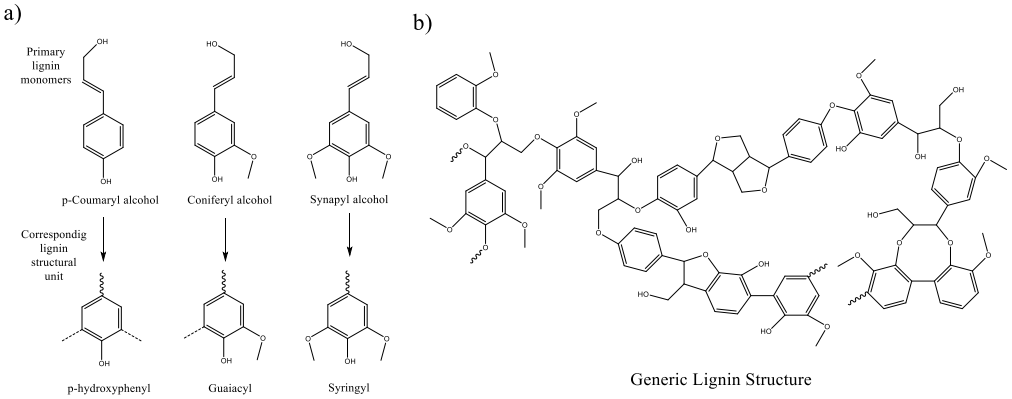

Figure 1.14: a) generic lignin structure, b) three major lignin components.

Lignin can be depolymerized using different strategies to obtain various aromatic monomers, among them only a few are commercially produced on large scale like vanillin and dimethyl sulfoxide [69]. Vanillin is a phenol moiety [70], that can be considered a very promising monomer since it is industrially derived from biomass and vanillin-based thermosets can be re-processed or degraded under acid conditions [71], can be biodegraded in soil [66,72] and possess antimicrobial properties [73]. Vanillin can be modified with (meth)acrylated or epoxy groups (Fig.1.15) to make it photocurable for the production of coatings or for 3D-printable applications [71].

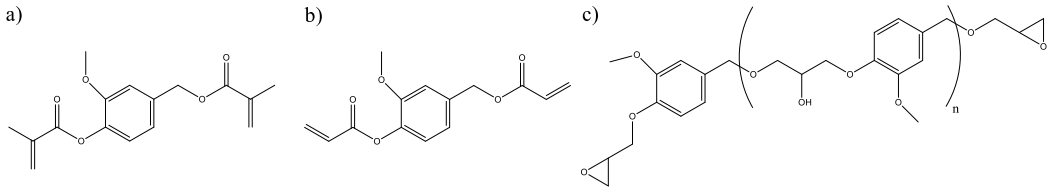

Figure 1.15: a) vanillin dimethacrylate, b) vanillin diacrylate, c) diglycidylether of vanillyl alcohol.

Other biobased molecules largely available are monoterpenes that are volatile by-products of plants processing. Among them, γ-terpinene, α-terpinene, limonene and α-pinene have been epoxidized and cationically photocured [74–77].

A further biobased resin source is the cashew nut shell liquid (CNSL). This liquid can be extracted from the Anacardium occidentalis mesocarp. From the distillation of this liquid, different molecules can be obtained named cardanols, anacardium acid, cardol and methylcardol (Fig.1.16). Cardanols are constituted by a phenol moiety meta substituted by up to four different C_{15} alkyl chains having different unsaturation amounts: 8.4% saturated chains, 48.5% mono-olefinic chains, 16.8% diolefinic chains and 29.33% triolefinic chains. Interestingly, cardanols possess both an aliphatic and aromatic structure, so this peculiar characteristic makes them an interesting starting material for the production of high-value products. Cardanols can be easily modified by grafting glycidyl groups or polyols. Currently, the cardanol market is led by Cardolite® corporation which distributes many cardanol-based resins, modifiers and reactive diluents for the production of coatings or adhesives [78,79].

Second Chapter

2 UV-curable starch-based hydrogels and organo/hydrogels

Hydrogels (HG) are three-dimensional hydrophilic polymeric networks able to adsorb a large quantity of water without dissolving. These networks can be generated by either physical or chemical processes. HGs have applications in various sectors like medical, pharmaceutical, agro-industry, and water treatment [80–84]. HGs based on biopolymers such as polysaccharides and proteins are gaining increasing attention since they are renewable and bacteriologically degradable [85–87]. Among them, starch is an abundant polysaccharide made of two types of D-glucose polymers: one linear called amylose and the other highly branched called amylopectin. The high availability of hydroxyl groups present in the starch chains make it possible to chemically preparing a high number of starch derivatives.

Starch-based hydrogels can partially mimic the extracellular matrix (ECM) of mammals, which is mainly composed of polysaccharides, water, and soluble proteins [88]. This means this type of material is applicable in the field of tissue engineering. Paragraph 2.2 describes how the chemical modification and the UV-curing of maize starch was carried out, followed by the mechanical characterization of the hydrogels and the evaluation of their cytocompatibility with human fibroblast cells. Furthermore, the processability of modified starch by digital light processing (DLP) 3D printing directly from aqueous solution was successfully demonstrated, envisaging a new frontier for tissue engineer and drug delivery.

Starch can also be used as a low-cost adsorbent for waste-water treatment. Paragraph 2.3 describes how a UV-curable starch-based sorbent was obtained from methacrylated starch (MS) and acrylated γ-cyclodextrin (ACy). Cyclodextrins are cyclic oligoamyloses deriving from starch. In this work, γ-cyclodextrin was chosen since it is one of the most interesting absorbents among the starch derivatives. In fact, this macromer possesses a torus structure that can trap different pollutants via the formation of the host-guest inclusion complexes. Paragraph 2.3 also describes

how the photoreactivity and the mechanical properties of MS-ACy organo/hydrogels (OHGs) were evaluated. Subsequently, the sorption capacity and the sorption kinetics of the MS-ACY systems were analyzed using Methylene blue (MB) as dye target. The DLP-printability of the OHGs was successfully proved, suggesting the possibility to obtain application-tailored geometries with enhanced surface area.

2.1 Experimental section

Nuclear Magnetic Resonance (NMR)

Starch and MS were analyzed by Bruker Advance 400 Fourier Transform NMR spectrometer (FT NMR, Bruker, Billerica, MA, USA) operating at 400 MHz. The ^{1}H-NMR was conducted at room temperature. Approximately 7 mg of each sample were dissolved in 1 mL of DMSO-d6. The ^{13}C-NMR was conducted at T=60 °C with 20 mg/mL starch concentration in DMSO-d6 to improve the spectra resolution.

Attenuated Total Reflectance-Fourier Transform Infrared Spectroscopy (ATR-FTIR)

The FTIR spectra of starch, MS, and the crosslinked hydrogels were recorded by Perkin Elmer Spectrum 2000 FTIR spectrometer (Perkin Elmer, Norwalk, CT, USA) equipped with a single reflection attenuated total reflectance (ATR) accessory (golden gate). All samples were analyzed from 4000 to 500 cm^{-1} with 4 cm^{-1} resolutions.

Photorheology and Rheology

The photorheology test was performed by Anton PAAR Modular compact rheometer (Physica MCR 302,Graz, Austria) with a parallel plate configuration (plate diameter = 15 mm) and a quartz bottom plate. All the formulations were tested at T=25°C with a gap value of 300 μm. Different tests were performed in time, stress, and frequency sweep to investigate the reaction kinetics and to evaluate the properties of the obtained thermosets. The time sweep experiment allows monitoring the thermoset formation by following the enhancement of the storage modulus (G') over time. This experiment was conducted at a strain amplitude (γ) of 0.5%, corresponding to a linear viscoelastic region with a constant frequency (ω) of 6 rad/s. After 30 s, a Hamamatsu LC8 lamp (28 $mW*cm^{-2}$) was switched on. Subsequently, an amplitude sweep experiment was conducted on the crosslinked hydrogels from γ=0.01 to 100% at a constant ω= 6 rad/s. After that, a frequency sweep experiment was performed on the freshly cured samples with γ=1% and ω

from 0.1 to 100 rad/s. From the data obtained in the last experiment, it was possible to calculate the thermosets' structure parameters. In fact, the value of G' in the plateau region (G'_p), so in the interval in which the G' value is independent of the ω, represents the region in which the energy applied is stored elastically. In this region, the polymer chains behave like entropic springs, not able to slide by one another since the applied stress velocity is higher than the segment relaxation capability. The network parameters that can be calculated are ν_e, ξ, and M^*_e representing the number of crosslinks, the distance between two entanglements points, and the molar mass between two entanglements points, respectively. The parameters were calculated by following Eq. 2.1,2.2, 2.3

$$\nu_e = \frac{G'_p N_A}{RT} \tag{2.1}$$

$$\xi = \frac{1}{\sqrt[3]{\nu_e}} \tag{2.2}$$

$$M_e^* = \frac{cRT}{G'_p} \tag{2.3}$$

Where c is the concentration, R is the universal gas constant, T is the temperature in Kelvin, G'_p is the storage modulus in the frequency-independent plateau region, and N_A is the Avogadro's number [89].

Compression Test

Compression uniaxial unconfined tests were performed with MTS QTestTM/10 Elite controller using TestWorks® 4 software. The cell load was set at 10N with a cross-head displacement speed of 0.5 mm/min. The test was performed on cylindrical specimens (φ = 10 mm; h = 10 or 11 mm). The data acquisition rate was 20 Hz. The experiments were repeated five times. The compression elastic modulus was calculated as the slope of the linear region of the stress-strain curves.

Swelling behavior

The swelling test was evaluated by a conventional gravimetric test. Air-dried samples were immersed in deionized water at a T=25°C, subsequently taken out at different time intervals and weighted (after removing the free water present on the surface of the sample with a tissue paper). The swelling degree ($S_{w\%}$), the equilibrium swelling ratio percentage ($SD_{eq}\%$), and the equilibrium water content percentage(EWC%) were estimated with the following formula:

$$S_{w\%} = \left(\frac{W_t - W_d}{W_d}\right) * 100, \quad (2.4)$$

$$SD\% = \frac{W_e - W_d}{W_d} \quad (2.5)$$

$$EWC\% = \frac{W_e - W_d}{W_e} * 100, \quad (2.6)$$

where W_t is the weight at time t, W_d is the weight of the dry sample, and W_e is the weight of the sample at the equilibrium state.

Gel Content (G%)

The gel content percentage (G%) was calculated according to Eq. (2.7):

$$G\% = \frac{W_1}{W_o} * 100 \quad (2.7)$$

whereW_1 is the weight of the dry gel after the treatment with deionized water, and W_0 is the weight of the dry sample before the measurement.

Differential Scanning Calorimetry (DSC)

Differential scanning calorimetric analyses were carried out using a Mettler Toledo DSC instrument. The study was conducted in an inert atmosphere (N_2 = 50 µl/min) with a heating rate of 10 °C/min. Approximately 4-6 mg of each sample were sealed in a 100 µL aluminum pan with pierced lids. The experiments were repeated in triplicates.

Cell Viability

A cell viability test was conducted to evaluate the toxicity of the degradation product of MS hydrogels. BJ human fibroblast cells (ATCC® CRL-2522™) were cultured on three different 96-well plates at a cell density of 2 × 104 cells/well for 24 h to reach confluence using DMEM-Dulbecco's Modified Eagle Medium enriched with 10% fetal bovine serum and 1% penicillin/streptomycin (Carlo Erba, Milan, Italy). Simultaneously, three hydrogels prepared with three different MS concentrations (5, 10, and 15 wt%) were soaked for 24 h in 1 mL of DMEM. In each case, 0.1 g of hydrogel was soaked in 1 mL of the medium. After 24 h, the media were collected and filtered through 0.22 µm filters to guarantee sterility. Then, the culture medium was removed from each well of confluent cells and substituted with the supernatant collected from the hydrogels. Controls (CTRL)

were obtained using the normal medium. After 24 h of incubation, the supernatant was carefully removed, and the cell viability assay was performed using non-fluorescent resazurin, which is converted into a highly red fluorescent dye (resorufin) by cell metabolism. Briefly, a volume of 100 µL of 0.1 mg/mL resazurin solution, obtained by diluting a resazurin working solution (1 mg/mL in phosphate-buffered saline-PBS, Sigma Aldrich, Milan, Italy) into DMEM, was added in each well, and the cultures were incubated for 1 h at 37 °C. Then, the fluorescent signal was monitored at 530 nm excitation wavelength and 590 nm emission wavelength using a plate reader (Victor X3, Perkin Elmer, Milan, Italy). Cell viability was calculated as a percentage value compared to CTRL. Six samples for each condition were used, and the experiments were performed three times. GraphPad Prism® software was used for one or two analyses of variance (ANOVA). Values $* p < 0.05$, $**p < 0.01$, $***p < 0.001$ were considered statistically significant.

Field Emission Scanning Electron Microscopy (FESEM)

The morphological characterization of the hydrogels was performed by using a FESEM Zeiss Supra 40 (Oberkochen, Germany). The samples were first lyophilized and then immersed in liquid nitrogen to induce a fragile fracture. Subsequently, the broken specimens were covered with a 5 nm thick film of Platinum.

Adsorption study

The adsorption study of MB was conducted by adding 8 mL of MB solution (40 mg/L) to 8 mg of dried organo/hydrogel at T = 25 °C. Afterwards, the vials were protected from light with an aluminium foil to avoid photocatalytic dye degradation. Then, a fixed amount of supernatant was taken out at different time intervals to monitor the dye adsorption. The MB concentration was determined by UV-visible spectroscopy by following the peak centred at 665 nm. The adsorption capacity at time t (q_m [mg/g]) and the equilibrium adsorption capacity (q_e [mg/g]) were calculated according to Eq. 2.8 and 2.8, respectively.

$$q_m = \frac{(C_0 - C_t) * V}{W} \tag{2.8}$$

$$q_e = \frac{(C_0 - C_e) * V}{W} \tag{2.9}$$

Where C_0 (mg/L) is the initial MB concentration, while C_e (mg/L) and C_t (mg/L) are the MB concentration at time t and at equilibrium, respectively. V (mL) is the volume of MB solution and W (g) is the mass of the dried hydrogel.

Two different kinetic models were then used to evaluate the adsorption rate and the potential rate-controlling step. The kinetic data were analysed using pseudo-first-order and pseudo-second-order models [90], using the Lagergren Equations (2.10 and 2.11).

$$\frac{dq}{dt} = k_1(q_e - q_m) \tag{2.10}$$

$$-\ln\left(\frac{1-q}{q_e}\right) = k_1 t \tag{2.11}$$

where k_1 is the rate constant of pseudo-first-order sorption [1/min]. According to this approximation, a plot of $-\ln((1-q)/q_e)$ vs t gives a straight line with slope k_1.

Equations 2.12 and 2.13 report the second-order kinetic rate equation and its integrated formula respectively [91].

$$\frac{dq}{dt} = k_2(q_e - q)^2 \tag{2.12}$$

$$\frac{t}{q} = \frac{1}{k_2 q_e^2} + \frac{t}{q_e} \tag{2.13}$$

where k_2 is the rate constant of the pseudo-second-order sorption [g/(mg*min)]. According to this approximation, a plot of t/q vs t gives a linear relationship with slope $1/q_e$ and intercept $1/k_2q_e^2$.

2.2 Starch-based hydrogels for biomedical applications

This section is based on the original research article titled "*Light Processable Starch Hydrogels*". This article was published in Polymers journal in 2020 (doi:10.3390/polym12061359) [92].

Maize starch was successfully methacrylated with a simple reaction with methacrylic anhydride to make it UV-curable. Subsequently, the photoreactivity of three different formulations containing 5, 10, and 15 wt% of starch in water and lithium phenyl-2,4,6-trimethyl-benzoyl phosphinate (LAP) as photoinitiator was characterized with a photorheology test. Then, the swelling abilities, the rheological and mechanical properties of the obtained hydrogels were evaluated. The obtained Young's modulus values cover the stiffens of different body tissues, suggesting the

possible applicability of those HG in tissue engineering. To exploit this possibility, a cell viability test was performed on the HG with human fibroblast cells. Finally, the printability of the methacrylated starch-water solution was established.

2.2.1 Materials and Methods

Materials

High-amylose Hylon VII maize starch (70% amylose) was obtained from Ingredion, Goole, UK. Methacrylic anhydride (MA), triethylamine (TEA) (>99%), dimethyl sulfoxide (DMSO) (ACS reagent P99.9%), ethanol absolute, and bis(acyl)phosphaneoxi lithium phenyl-2,4,6-trimethylbenzoyl phosphinate (LAP) were purchased from Sigma Aldrich (Milan, Italy). Acrylated cyclodextrin (ACy) was synthesised and kindly provided by a colleague (Andrea Cosola).

Synthesis of Methacrylated Starch

Typically methacrylated starch was synthetized as followed: approximately 6g of high amylose maize starch (S) were solubilised in 200 mL of DMSO at T=70°C. After the gelatinization of starch (which took approximately 30 minutes), the solution was cooled down at room temperature. Subsequently, methacrylic anhydride was added dropwise at a molar ration of Anidrous Glucose Unit (AGU) :MA=1:2. Triethylamine was used to catalyse the reaction (AGU:TEA=1:0.04). Then the solution was left to react at room temperature for 18h in stirring condition. The final product was three times precipitated in ethanol and solubilized in deionised water to be purified. The final starch-water solution was lyophilized.

Photocuring of Methacrylated Starch hydrogels

Different methacrylated starch (MS) content (5, 10, 15%wt) were solubilized in water (Tab.2.1). It was impossible to further increase the MS concentration because, with 15wt%, its solubility limit was reached. Subsequently, in all the solutions 1phr (weight per hundred resin) of LAP photoinitiator was added. Then the solutions were placed in silicon mould and UV-cured under the UV-DYMAX lamp (115 mW/cm^2) for 1 minute.

Table 2.1: Hydrogels pristine formulations.

Sample name	MS content in water (wt%)	LAP (phr)
MA-Starch5	5	1
MA-Starch10	10	
MA-Starch15	15	

3D-Printing of Methacrylated Starch hydrogels

The MA-Starch10 formulation was 3D printed with stereolithography based ASIGA UV-MAX DLP printer (λ=385 nm, XY resolution of 62 µm). The layer thickness was set to 50µm, the light intensity at 10 mW/cm^2 and the exposure time at 5 s.

2.2.2 Results and discussion

In Scheme 2.1 is reported the starch methacrylation reaction followed by it photocrosslinking that lead to the formation of the hydrogels.

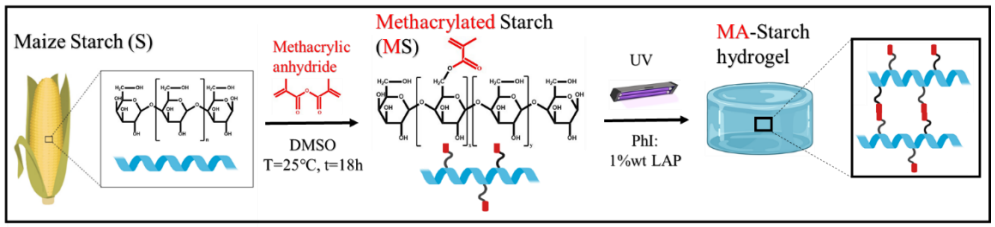

Scheme 2.1: Illustration of the maize starch methacrylation followed by the UV-curing reaction. In this scheme, the MA-Starch shows only the substitution of the secondary alcohol; however, there could also be substitution of the primary alcohols.

The success of the methacrylation reaction was assessed by ^{1}H-NMR, ^{13}C-NMR, and ATR-FTIR spectroscopy. In Fig.2.1 is reported the ^{1}H-NMR of the maize starch (black) and of the methacrylated starch (red). In the black spectrum, there can be observed the typical starch peaks. The peaks at δ=4.57, 5.40, 5.49 ppm are assigned to the O-H protons in 2, 3, 6 positions, respectively; the peaks at δ= 3.59, 3.66 ppm represent the C-H protons in 2, 3, 4, 5 positions, while the peak at δ=5.11 ppm is assigned to α-carbon C-H of the anhydroglucose carbon in 1 position. The spectrum also presents a huge peak at δ=3.35 ppm, which is assigned to the adsorbed water on the starch chains [93]. In the red spectrum (MS), new peaks can be seen at δ=1.9 ppm, δ=5.66-6.07 ppm, which represent the methyl group and methacrylic double bond, respectively. Those additional peaks confirm the successful modification of the starch structure. The MS spectrum shows broader peaks with respect to the starch one. This outcome can be ascribed to the formation of different starch-chains structures during the methacrylation reaction. From the integrals of the ^{1}H-NMR peaks, it is possible to calculate the degree of substitution (DOS) of the -OH groups using Eq.2.7.

$$DOS = \left(\frac{\frac{I_{1.9}}{3}}{I_{5.11}}\right)/3 \qquad (2.7)$$

Where $I_{1.9}$ and $I_{5.11}$ are the integrals of the peaks of the methyl protons and the proton in the anhydrous glucose unit (AGU) in 1 position, since, in every AGU, there are three hydroxyl groups, the formula is divided by 3. The final DOS is 0.08, which can also be seen as one methacrylated group every fourth glucose ring. This result is like one previously reported of a starch methacrylation with glycidyl methacrylate [94].

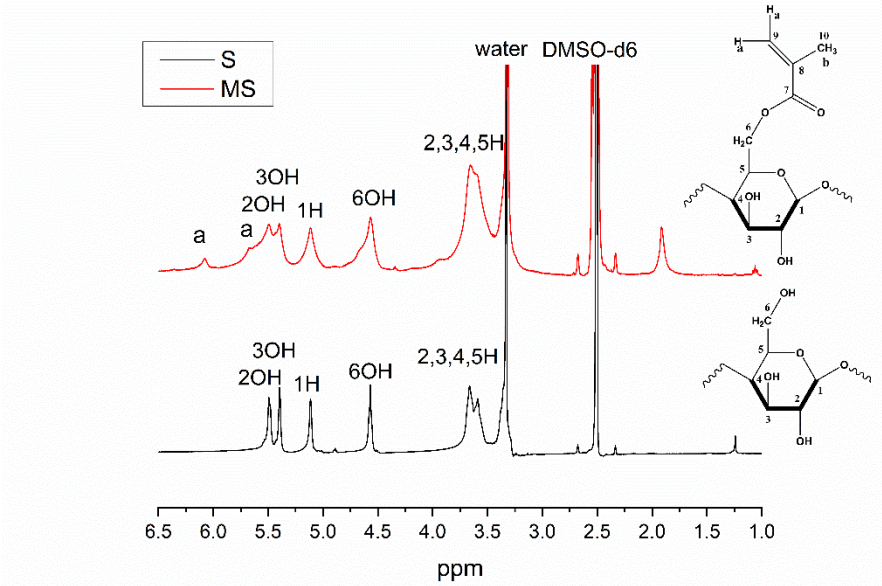

Figure 2.1: ^{1}H-NMR of Starch (S) and Methacrylated starch (MS) with peaks assignment.

The ^{13}C-NMR spectra of S and MS are shown in Fig.2.2. In the starch spectrum, the carbon atoms of the starch AGU can be clearly observed. The signals at δ=61.09, 72.12, 72.55, 73.74, 79.37 and 100.54 ppm are attributed to the C6, C5, C2, C3, C4 and C1 of the AGU starch. While in the modified starch spectrum it can be notice the presence of new peaks at δ=18.45 ppm, at δ=136.61-127.75 ppm, and δ=170.38 ppm representing the CH_3, C=C and C=O, respectively. This result further confirms the success of the methacrylation reaction.

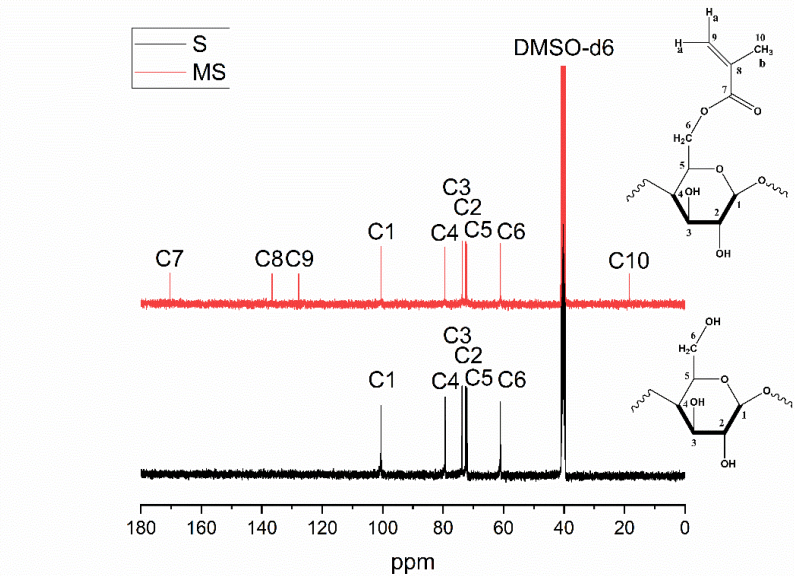

Figure 2.2: ^{13}C-NMR of Starch (S) and Methacrylated starch (MS) with peaks assignment.

FTIR analysis was also used to prove the successful starch modification. In Fig.2.3 are reported the spectra of starch and MS. All the typical starch signals could be observed and analyzed. In the starch-spectrum are displayed the typical starch functional groups. At 3320 cm^{-1} it can be found a broad peak which represents the -OH groups vibrations. At 2925 cm^{-1} it can be observed the -CH_2- stretching vibration peak. While the band at 1638 cm^{-1} is assigned to the hydroxyl groups of the absorbed water in the amorphous region of starch. The peaks at 1148 and 1076 cm^{-1} represent the C-O-C symmetric stretching of cyclic ether group and C-H bending vibration, respectively. While the peaks at 994 and 927 cm^{-1} are attributed to the C-O-C stretching and skeletal vibration of the α-1,4 glycosidic linkage, respectively. The peak at 855 cm^{-1} represents the C(1)-H and CH_2 deformation vibrations. Finally, the peak at 762 cm^{-1} is assigned to the C-C stretching vibration [95,96]. Four new peaks can be observed in the MS spectrum. The peaks at 1640 and 1709 cm^{-1} can be assigned to the C-O and C=O stretching vibration, while the peaks at 1300 and 815 cm^{-1} represents the C=CH_2 out of plane bending vibrations [97–99].

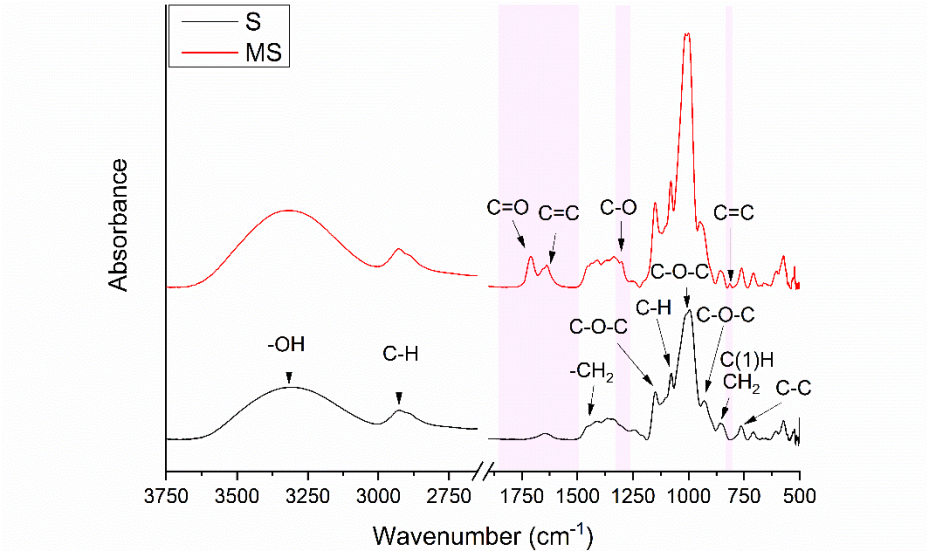

Figure 2.3: FTIR spectra of Starch (Black) and Methacrylated Starch (Red).

Three MS formulations were prepared as described in the materials and methods section and subsequently tested with an amplitude sweep experiment to identify the linear viscoelastic region (LVR). The photocrosslinking kinetics of those formulations was subsequently studied using a photorheology test. In this test, the reaction is followed by the changes in the rheological properties of the material, especially the enhancement of the storage modulus (G'). The crosslinking reaction can be considered completed when G' reaches a plateau. As it can be observed from Fig.2.4, both the MA-Starch10 and MA-Starch15 formulations started to react as soon as the lamp was switched on and their G' reached a plateau after 90 s. On the contrary, the MA-Starch5 formulation shows a delay in the curing process (induction time), and its G' reached a plateau after 120s. This result can be possibly due to the low concentration of starch in water, which, combined with the achieved low DOS, can have partially reduced the kinetics of the radical reaction.

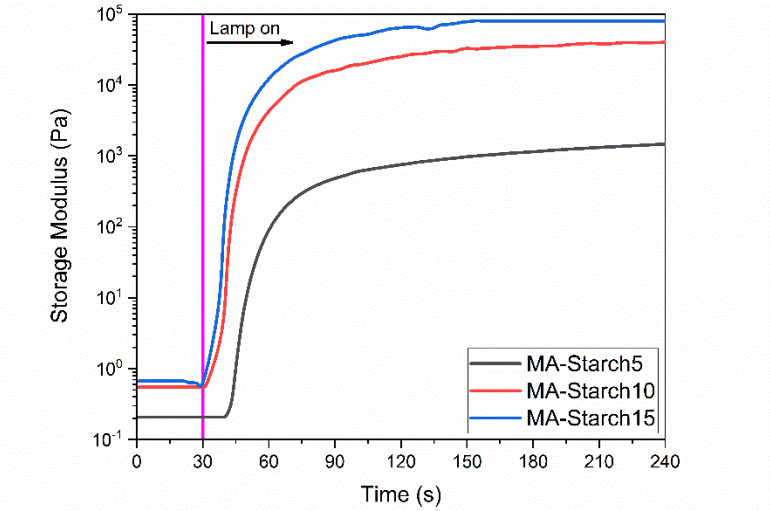

Figure 2.4: Storage modulus G' as a function of time. The lamp was switched on after 30 seconds.

Subsequently, the mechanical, rheological, and swelling properties of the obtained hydrogels were carefully evaluated. In Fig.2.5,a are reported the compressive stress-strain curves of MA-Starch10 and MA-Starch15 hydrogels. As can be noticed, by simply increasing the MS content in water, the compressive stiffness of the hydrogels almost duplicated (Tab.2.2). Interestingly, the obtained compressive young's modulus (E_c) values (13 and 20 kPa) are very similar to those previously reported of silk fibroin and hemicellulose hydrogels used in tissue engineering. Moreover, these values cover the range of different body tissues, which suggests using these HGs for tissue engineering [100].

The rheological properties were instigated on freshly polymerized hydrogels directly prepared on the parallel plate. Initially, an amplitude sweep experiment was performed to determine the linear viscoelastic region (LVR). Subsequently, it was performed a frequency sweep experiment with a strain amplitude fixed at γ=1%.

The results of the frequency sweep experiment are reported in Fig.2.5,b while the obtained values are summarized in Tab.2.2.

It can be observed that in all HGs, the complex viscosities showed a negative slope of -0.9, meaning that all the HGs showed pseudo-plastic behavior [89]. The G' and loss modulus (G'') curves show a linear trend, but the G'' values are lower than the G' one meaning that the elastic components of the HGs are dominant over the viscous ones. This G'-G'' behaviour is typical for gel structures [101]. The G' and G'' values are very similar to those previously reported for carboxymethylated starch hydrogels [102,103]. From the rheology investigation, it was also possible to

estimate the values of the networks parameters as described in the experimental section. The distance between two entanglements points (ξ) and the increased numbers of crosslinks (ν_e) were calculated using the storage modulus plateau (G'_p) value at ω= 10 rad/s. As it can be observed from the values reported in Tab.2.2, increasing the MS in water, lead to an enhancement of the ν_e and to a decreased of the ξ.

Fig.2.5,c shows the swelling curves of the HGs in water. The swelling capability of MA-Starch5 and MA-Starch10 were quite similar, although the MA-Starch5 swelling at equilibrium does not correspond to the maximum value but only to the maximum before breaking. Instead, the MA-Starch15 showed lower swelling capability. These results agree with the rheological experiments since higher crosslinked networks have lower swelling ability.

A gel content evaluation was also performed on the HGs in hot water to evaluate the curing efficiency. The obtained values are reported in Tab.2.2. All the HG showed 100% of G%.

The thermal properties of the HGs were also analysed by DSC measurements and compared with the pristine starch and un-crosslinked starch. However, no significant changes can be noticed from the glass transition temperature (Tg) values reported in Tab.2.2.

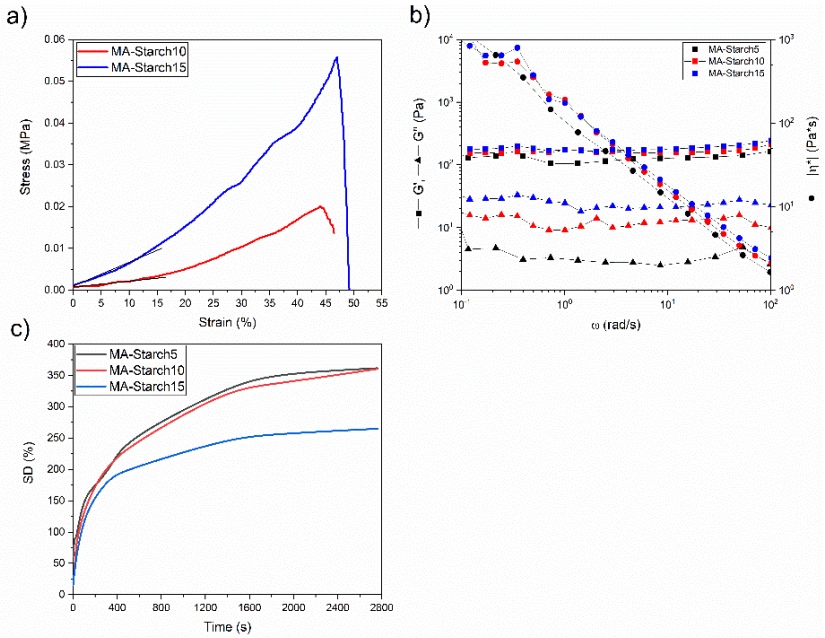

Figure 2.5: a) Compression curves of MA-Starch10 and MA-Starch15; b) Rheology measurements of the HGs; c) Swelling capability of the HGs.

Table 2.2: Mechanical, rheological, G%, and thermal properties of the S, MS, and HGs.

	S	MS	MA-Starch5	MA-Starch10	MA-Starch15
E_c [kPa]	-	-	-	12.7 ± 0.4	20.3 ± 1.7
G'_p [Pa]	-	-	105	159	178
ν_e [m^{-3}]	-	-	$2.55 * 10^{22}$	$3.86*10^{22}$	$4.32*10^{22}$
ξ [m]	-	-	$3.40*10^{-8}$	$2.96*10^{-8}$	$2.85*10^{-8}$
SD_{eq}%	-	-	360	360	270
EWC [%]	-	-	78	78	73
G%	-	-	100	100	100
T_g [°C]	105 ± 2	115 ± 1	106 ± 2	106 ± 9	101 ± 8

Since different scaffolds and hydrogels made of starch have already been used in biomedical fields, a preliminary cell viability study was performed on the obtained UV-cured HGs to assess their cytocompatibility.

BJ human fibroblast cells were cultured in the HGs supernatant. Interestingly, no negative effects were observed on the cell viability (Fig. 2.6) and all the HGs results were very close to the control one. This outcome means that the methacrylation, photocrosslinking process, and LAP presence do not negatively impact the cell vitality.

Those preliminary results further confirmed the potential applicability of those hydrogels in the biomedical fields.

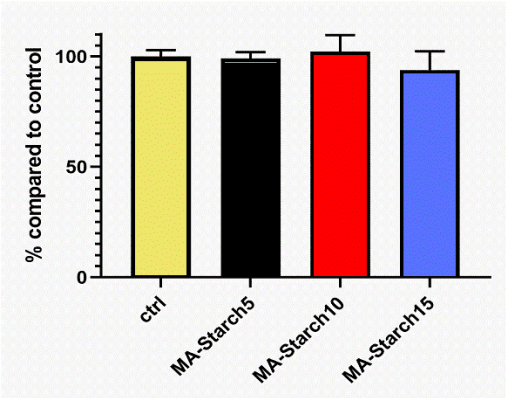

Figure 2.6: Cell viability results of BJ human fibroblasts using the supernatant obtained from the HGs compared with the control (ctrl).

The high photocuring reactivity of the MS formulations and the final mechanical properties of the HGs suggests the possibility to use those formulations as photo-curable resins for DLP-printing technology. The printability of the MA-Starch10 was therefore assessed. MA-Starch10 was selected among the others

because its photocrosslinked network showed a compressive Young's modulus of 13 kPa, so very close to the muscle tissue elasticity (12 kPa). Initially, simply CAD geometries were selected to evaluate the 3D-printability of this resin and to investigate the achievable resolution. The preliminary tests proved the possibility to obtain good resolution in the x-y plane. Fig.2.7,a shows the smallest 3D-printed object, which can be printed with sharp edges and reduced over-polymerization (1.5 x 0.5 x 2 mm). Different strategies can be applyed to increase the resolution of the 3D-printed objects, among them, the addition of a dye to decrease the light diffusion in the vat is one of the most used [104]. Therefore, methyl red dye (0.2 phr) was added in the formulation, and the printing parameters were adjusted accordingly. The obtained printed objects are reported in Fig. 2.7,b-c (5 x 5 x 1 mm). Although, since the cytocompatibility of methyl red was not assessed, other alternatives should be looked for. The fibroblasts viability test revealed that the DMEM solution in contact with the MA-Starch hydrogels possesses a neutral pH and a pink colour. So, the possibility to substitute the MS-water solution with the MS-DMEM solution was evaluated. The honeycomb structure with millimetric thick wall reported in Fig.2.7,d was 3D-printed using MA-Starch10-DMEM solution (24 x 24 x 4 mm). However, in this structure some degree of over polymerization can still be seen ascribing to the light colour of the solution. All the printed HGs were post-cured to obtain complete curing according to the data obtained from the photo-rheology test.

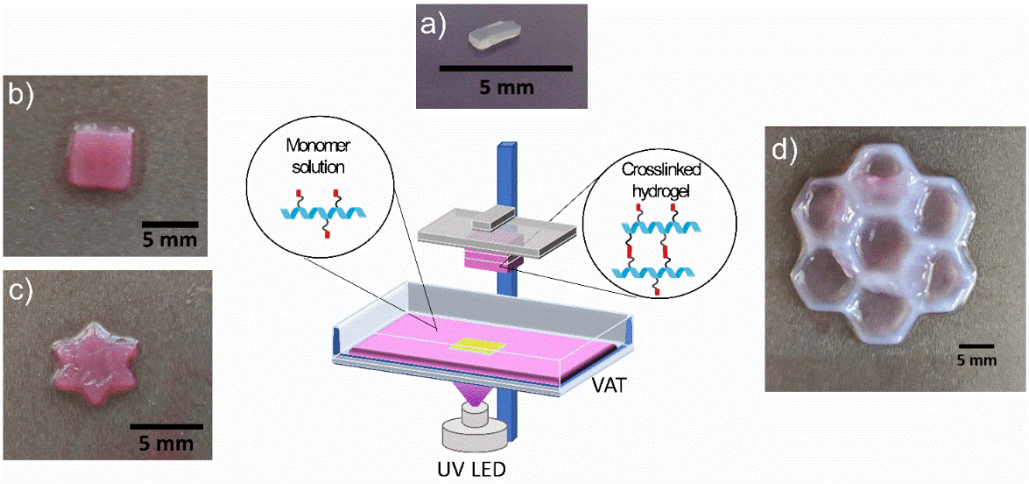

Figure 2.7: 3D-DLP printed hydrogels: a) smallest hydrogel printed without dye; b,c) simple geometries printed using methyl red as a dye; and d) complex flower geometry.

2.2.3 Conclusions

Maize starch hydrogels were successfully UV-cured either by a UV lamp or by a DLP printer. Initially, starch was chemically modified with a methacrylation reaction which was assessed by ^{1}H-NMR, ^{13}C-NMR and FTIR spectroscopy. Three different aqueous formulations were prepared by dispersing the modified starch at different concentrations in the presence of LAP as the photoinitiator. The high reactivity of the formulation was confirmed by the photorheology test. The HG

network parameters were calculated from the rheology test. Higher MA-Starch content in the hydrogels higher the crosslinking density and the compressive elastic modulus, while lower is the swelling capability. The supernatant of the crosslinked HGs does not show any cytotoxicity against human BJ fibroblast cells. Finally, the printability of the MA-Starch10 was successfully assessed. The obtained results are really promising for future applications of UV-curable starch in tissue engineering and cell carriers.

2.3 Starch-cyclodextrin organo/hydrogels for water treatment

This section is based on the original research article titled " *From polysaccharides to UV-curable biorenewable organo/hydrogels for methylene blue removal* ". This article was published in Polymer journal in 2021 (doi.org/10.1016/j.polymer.2021.124257) [105].

All starch-derived organo/hydrogels were light processed and tested as bio-sorbent to remove methylene blue (MB) from water (Figure 2.8). The DLP-printability of the OHG was also investigated to allow the production of sorption materials with tailored geometry, possibly leading to a new frontier for waste-water treatment.

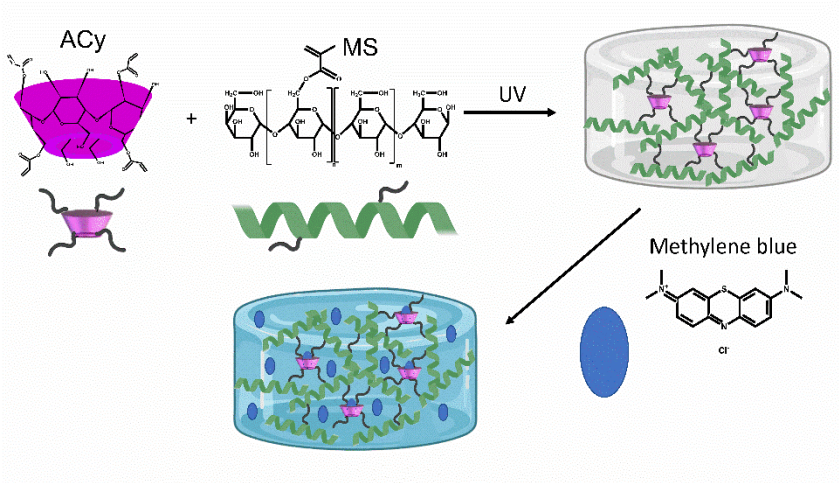

Figure 2.8: Scheme of MS-ACy hydrogel preparation for the sorption of methylene blue.

2.3.1 Materials and Methods

Materials

High-amylose Hylon VII maize starch (70% amylose) was obtained from Ingredion, Goole, UK. Methacrylic anhydride (MA), triethylamine (TEA) (>99%),

dimethyl sulfoxide (DMSO) (ACS reagent P99.9%), ethanol absolute, methylene blue (MB), methyl red and phenylbis(2,4,6-trimethylbenzoyl)phosphine oxide (BAPO) was purchased from Sigma Aldrich (Milan, Italy). Methacrylated starch was synthesized as previously reported in Chapter 2.3.1. Acrylated cyclodextrin (ACy) was synthesized and kindly provided by Andrea Cosola [106].

Photocuring of Methacrylated-Starch and Acrylated Cyclodextrin organo/hydrogel

Formulations containing different MS-ACy weight ratios were obtained by dissolving the modified polysaccharide in an H_2O/DMSO (20/80) mixture (Tab.2.3). The total monomer concentration was kept at 10 wt%. In all the solution was added 1phr of BAPO as a photoinitiator. The formulation was then poured in a silicon mould and UV-cured under a Hamamatsu LC8 lamp equipped with an 8 mm light guide (100 mW/cm^2)**.**

Table 2.3: organo/hydrogels pristine formulations

Sample name	MS (wt%)	ACy (wt%)	BAPO (phr)
MS	100	0	1
MS-ACy 3-1	75	25	
MS-ACy 2-1	66	34	
MS-ACy 1-1	50	50	
MS-ACy 1-2	34	66	
ACy	0	100	

3D printing of Methacrylated-Starch and Acrylated Cyclodextrin organo/hydrogel

The printability of the polysaccharide formulations was investigated using DLP 3D–Printing with an Asiga UV-MAX DLP printer (nominal XY pixel resolution of 27 μm, light emission at λ=385nm). Different CAD models were converted into STL files, and 3D printed. The layer thickness and the light intensity were fixed at 50 μm and 30 mW/cm^2, while the exposure time was set at 3 s. The printed objects were post-cured for 3 min using a mercury lamp provided by Robot Factory (UV-light, 12 mW/cm^2).

2.3.2 Results and discussion

Biobased “all-starch” derived organo/hydrogels (OHGs) were photocured and tested as bio-sorbents to remove MB from water. The OHGs were prepared by mixing methacrylated starch MS (see Section 2.1.1) and acrylated cyclodextrin (ACy) in an H_2O/DMSO (20/80) mixture.

To evaluate the photoreactivity of the formulations, real-time photorheology tests were performed. The reaction kinetics were monitored by following the

storage modulus (G') overtime under light irradiation. Fig. 2.9 shows the photorheology curves of the OHGs pristine formulations. All the formulations showed high reactivity, less than 2 seconds of induction time and reached a G' plateau in less than 60 seconds. Although, even if the reactivity of the formulations seems equals, if we compare the reaction kinetics ($\Delta G'/\Delta t$) reported in Tab.2.4, it is possible to observe that the addition of the ACy enhances almost three times the kinetics of the formulations. This result can be attributed to the higher reactivity of the acrylate groups with respect to the methacrylate ones and the higher degree of functionalization of ACy with regard to MS. Moreover, the ACy addition also increases the final G' value meaning that the improved crosslinking efficiency of ACy leads to the formation of stiffer OHGs [106].

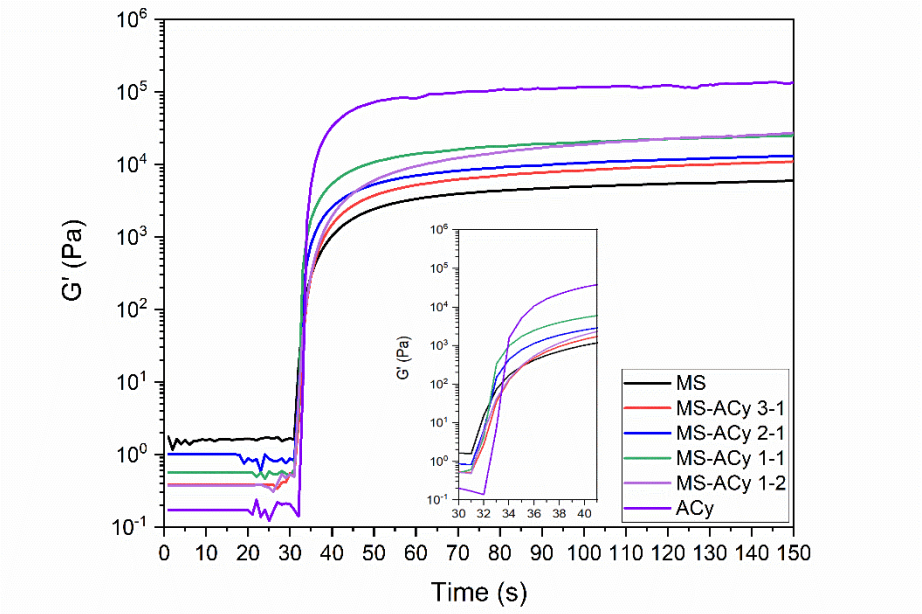

Figure 2.9: Photorheology curves of the OHGs precursor formulations.

The rheological properties of the obtained OHGs were subsequently tested with a frequency sweep experiment performed on the linear viscoelastic region. As can be observed in Fig.2.9,a the dynamic viscosities of the OHGs showed a linear trend with a slope of -0.9, meaning that the OHGs possess a pseudo-plastic behaviour [89]. The network parameters (Tab.2.4) were calculated according to the equations reported in the experimental section by using the storage modulus value (G'_p) at ω = 1 rad/s. The numbers of crosslinks (ν_e) increased by increasing the ACy content, while the distance (ξ) and the molar mass (M^*_e) between two entanglements point decreased by at least one order of magnitude. These results can be ascribed to the high crosslinking efficiency of ACy.

The addition of the ACy also leads to an enhancement of the Tg (Tab.2.4) as observed in the DSC measurements, which is consistent with the previous results since an increase in crosslinking density of a polymer reflects into its glass transition [107].

Moreover, a compression test was also conducted on the UV-cured OHGs to evaluate their mechanical properties. Fig.2.b reports the OHGs average stress-strain curves, and in Tab.2.4 are reported the values of compressive Young's modulus (E_c), ultimate compression strength (UCS), and the compression at the break. The achieved E_c values are generally higher than those reported in the literature for other polysaccharides-based hydrogels [62,108]. As can be noticed, the addition of ACy improves the mechanical properties of the OHGs. In fact, OHGs containing higher ACy content showed higher E_c and UCS while slightly lower compression at the break. These results are in good agreement with the previous findings, and further confirm the overall general performances improvement of the OHGs with the ACy addition.

After that, the swelling capability of these OGHs was investigated. Before the test, the DMSO present in the OHGs was removed *via* solvent extraction in aqueous media. Subsequently, the samples were air-dried and yet again immersed in water to start the test. The obtained swelling curves are reported in Fig.2.10,d, while the swelling at equilibrium (SD_{eq}%) and the equilibrium water content (EWC %) are presented in Tab.2.4. As can be observed from the graph, the SD_{eq}% is reached after 15 h for all the OHGs. The influence of the ACy addition on the swelling capability can be clearly seen; in fact, the SD_{eq}% and the EWC% decreased in the presence of ACy from 395 (MS) to 54 (MS-ACy 1-2) and from 80 (MS) to 35 (MS-ACy 1-2), respectively.

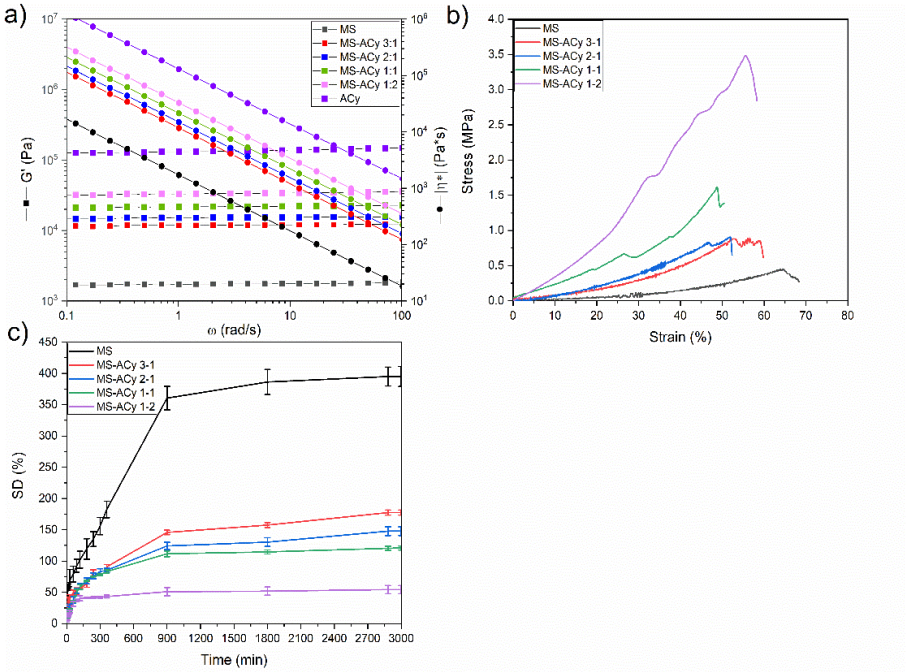

Figure 2.10: a) frequency sweep plots; b) compression stress-strain curves; and c) swelling kinetic of the UV-cured OHGs.

Table 2.4: Photo-/rheological, mechanical, thermal and swelling data of the MS-ACy OHGs.

	MS	MS-ACy 3-1	MS-ACy 2-1	MS-ACy 1-1	MS-ACy 1-2	ACy
Reaction rate [Pa/s]	134	201	266	300	335	1800
G'_p [kPa]	1.8	12	15.4	22.1	34.1	131.2
M_E*[g/Mol]	156.5	22.9	17.9	12.5	8.1	2.1
ν_E [1/m^3]	$4.3 * 10^{23}$	$2.9 * 10^{24}$	$3.7 * 10^{24}$	$5.4 * 10^{24}$	$8.3 * 10^{24}$	$3.2*10^{25}$
ξ [m]	$1.3 * 10^{-8}$	$7.0 * 10^{-9}$	$6.4 * 10^{-9}$	$5.7 * 10^{-9}$	$4.9 * 10^{-9}$	$3.1*10^{-9}$
T_G [°C]	95	98	100	102	109	N.A.
E_C [MPa]	0.36 ± 0.15	0.78 ± 0.01	1.04 ± 0.08	2.10 ± 0.28	3.93 ± 0.11	N.A.
Compression at break [%]	64 ± 23	56 ± 4	52 ± 0.1	49 ± 2.8	56 ± 3.5	N.A.
UCS [MPa]	0.59 ± 0.19	0.89 ± 0.10	0.90 ± 0.13	1.62 ± 0.15	3.48 ± 0.23	N.A.
SD_{eq}%	395 ± 15	178 ± 4	147 ± 7	120 ± 3	54 ± 6	N.A.
EWC [%]	80 ± 0.7	64 ± 0.9	60 ± 1.4	55 ± 1.0	35 ± 2.7	N.A.

FESEM images of the freeze-dried OHGs were collected to investigate the microstructures of the samples. As can be noticed from Fig. 2.11,a and 2.12,a the MS OHG surface presents a high degree of porosity, with a medium pore size higher

than 20 µm. On the contrary, the ACy surface shows no porosity in the micrometric scale (Fig.2.11, Fig. 2.12). The other OHGs compositions exhibit a decrease in the pore amount and size progressively more pronounced when the ACy amount increases (Fig. 2.11, Fig. 2.12). Those results are consistent with the previous analysis, confirming that the ACy additions lead to the formation of highly crosslinked networks.

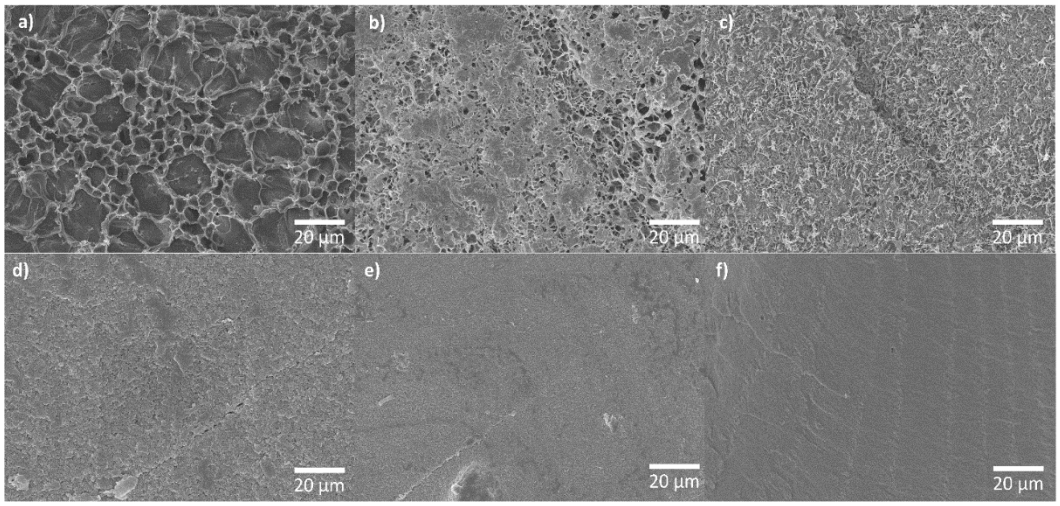

Figure 2.11: FESEM images of different samples prepared from a) MS, b) MS-ACy 3-1, c) MS-ACy 2-1,d) MS-ACy 1-1, e) MS-ACy 1–2, f) ACy.

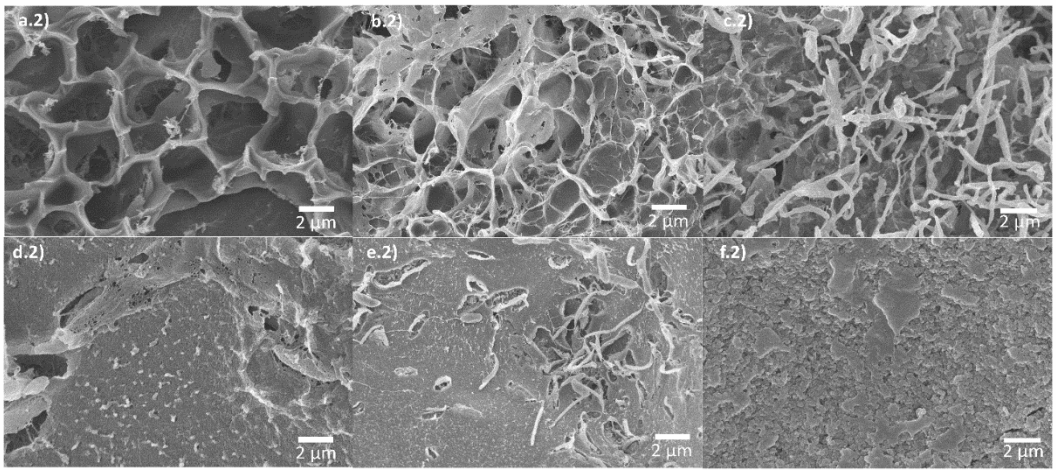

Figure 2.12: High magnification FESEM images of different samples prepared from a) MS, b) MS-ACy 3-1, c) MS-ACy 2-1,d) MS-ACy 1-1, e) MS-ACy 1–2, f) ACy.

The sorption capability of the photocrosslinked OHGs was subsequently tested. In fact, these OHGs are really promising candidates for the sorption of organic dyes since the molecular structure of MS has a large availability of hydroxyl groups that possess chelating properties, and the ACy cavity can form host-guest inclusion

complexes. The selected target molecule was methylene blue (MB), a cationic dye that can fit the ACy cavity dimension. Fig. 2.13 reports the MB sorption kinetics of the different OHGs. The OHGs adsorption process was fast, reaching the equilibrium adsorption capacity (q_e) after 600 min. The obtained q_e values are comparable with the ones previously reported for other polysaccharide-based hydrogels like: regenerated cellulose/GO [109], carboxymethyl cellulose/graphene oxide (GO) (59 mg/g) [110], carbonized lignosulfonate/gelatin (38 mg/g) [111] and corn stalk/organic montmorillonite composite (49 mg/g) [112].

Other than the OHG composition, the sorption properties also depend on the network's porosity and the free volume of the adsorbent, which is expected to decrease as the crosslinking density increases [113]. Although, in the present case, the q_e increases with increasing ν_e reaching a maximum in the MS-ACy 1-1 OHG. Further addition of ACy, negatively affected the q_e. Therefore, this composition can be seen as a threshold concentration beyond which the molecular diffusion into the network is hindered by ν_e enhancement, possibly reducing the accessibility of the ACy sites to the MB molecules. So, the OHGs sorption mechanism is probably the result of two different sorption mechanisms; one can be ascribed to the hydrogen bonding interaction and the other to the host-guest inclusion complexes formed by ACy and MB.

It was possible to estimate the sorption rate k_a (Tab. 2.5) from the graph q_m vs t, reported in Fig.2.13 [113]. Enhancing the ACy content led to an increase in the k_a value from 0.49 to 0.81 [mg/(g*s)]. All the OHGs showed high ka suggesting that the sorption mechanism is mainly occurring at the OHGs surfaces. This result is in good agreement with the sorption scaling time since the swelling equilibrium is reached after 15h, while the sorption equilibrium is reached faster (after 10 h).

The kinetics data were subsequently fitted using the linear pseudo-first-order and pseudo-second-order kinetic models and reported in Fig. 2.13 c, d respectively. It can be clearly observed that the data fitted the pseudo-first-order model (Fig. 2.13,c) did not show a linear trend meaning that this model is not valid to describe the sorption process [90]. Instead, the data plotted using the pseudo-second-order kinetic model displayed a linear trend. So, this model was suitable to describe the sorption in the OHGs, as proved by the similarity between the estimated adsorption capacity $q_{e,cal}$ with the experimental $q_{e,exp}$ and by the obtained high correlation coefficient R^2>0.99823 (Tab. 2.5). The excellent data fitting with this model suggests that chemisorption is the rate-determining step of the OHGs sorption [114].

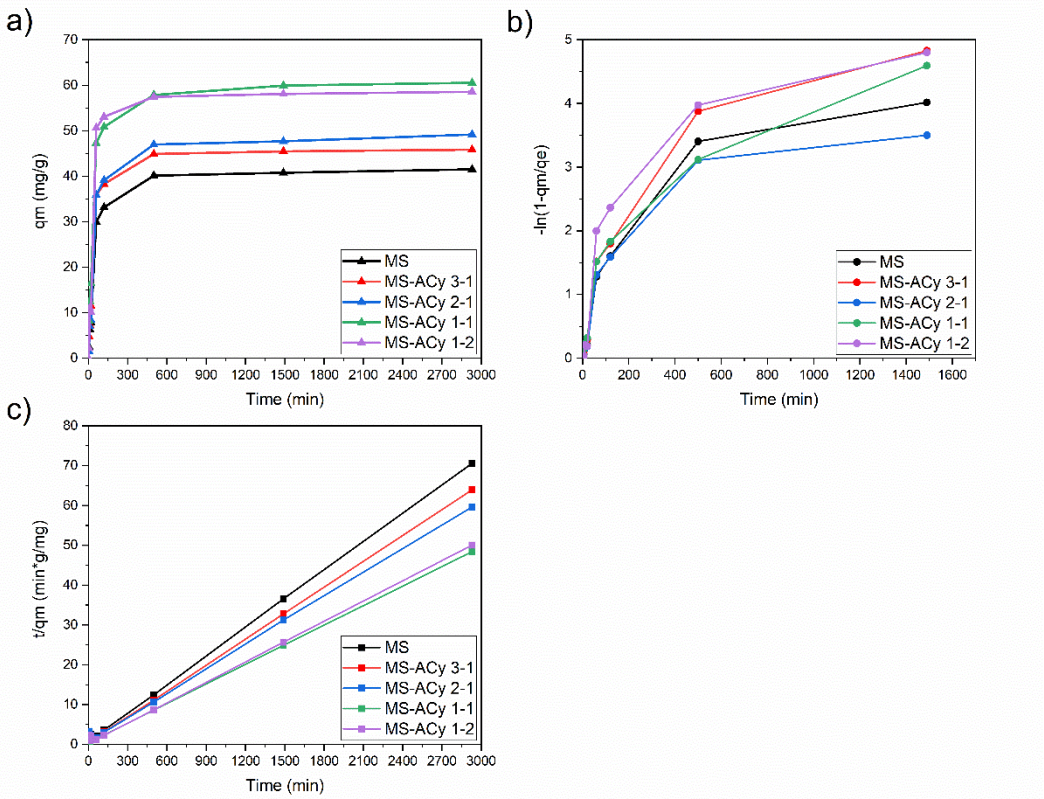

Figure 2.13: sorption kinetics study a) q_m vs t; b) data fitted with the pseudo-first-order kinetics model; c) data fitted with the pseudo-second-order kinetics model.

Table 2.5: Pseudo-second-order fitting parameters for MB adsorption.

	k_a [mg/(g*s)]	$q_{e,calc}$ [mg/g]	$q_{e,exp}$ [mg/g]	k_2 [g/(mg*min)]	R^2
MS	0.49	41.52	42.30	4.52 * 10-4	0.999525
MS-ACy 3-1	0.58	45.83	46.49	5.82 * 10-4	0.999771
MS-ACy 2-1	0.60	49.17	50.40	2.75 * 10-4	0.998231
MS-ACy 1-1	0.80	60.53	59.88	3.08 * 10-4	0.997972
MS-ACy 1-2	0.81	58.55	61.24	49.5 * 10^{-4}	0.996524

Additionally, the DLP-printability of the OHGs having the best sorption capability, so the MS-ACy 1-1 and the MS-ACy 1–2, was assessed. Initially, the formulations were tested without any dyes, but the 3D-printed OHGs showed low resolution due to the over-polymerization (Fig. 2.14, a-top). Therefore, 0.2 phr of methyl red (MR) was added to the formulations. Further photorheological tests were conducted on the photocurable formulations containing 0.2 phr of MR to investigate its possible

negative effect on the UV- curing reaction. However, its effect was negligible while the achieved printing resolution was definitely improved (Fig. 2.14, a-bottom). Nevertheless, the 3D-printed MS-ACy 1-1 OGHs showed poor self-standing capability, so further investigations were conducted only on the MS-ACy 1–2 formulation. Different MS-ACy 1–2 OHGs were successfully obtained with excellent fidelity with the CAD model and improved mechanical stability (Fig. 2.14, b-c). The achieved good printability is a really interesting result since it will allow the fabrication of objects with high surface area, enhancing the sorption capability of the materials.

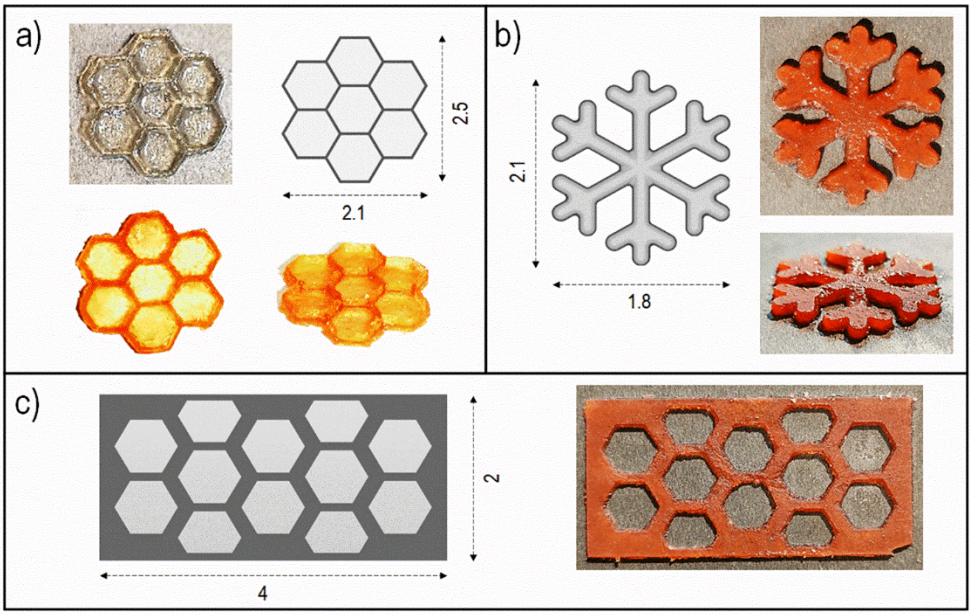

Figure 2.14: 3D-DLP-printed OHGs of a) MS-ACy 1-1 and b-c) MS-ACy 1–2.

2.3.3 Conclusions

In this section, a new all-starch-derived polysaccharide was successfully photocured and tested as bio-sorbents for waste-water treatment. The reactivity of the formulations containing methacrylated starch (MS) and acrylated cyclodextrin (ACy) was evaluated *via* a photorheology test. This investigation revealed that enhancing the ACy content fastens the polymerization kinetics, which can be ascribed to the high reactivity of the ACy multifunctional macromer. Moreover, increasing the ACy content leads to higher crosslinking density, smaller porosity and stiffer networks, as proved from the rheological, morphological and thermo-mechanical analysis. The presence of the ACy into the networks also strongly influences the methylene blue sorption (MB). In fact, even if the addition of ACy lower the swelling at equilibrium, the sorption of MB increase, probably due to the

combination of the chelating properties of the -OH groups present in the MS chains and the ability of ACy torus structure to form inclusion complexes with MB. All the experimental sorption data perfectly fit the pseudo-second-order kinetic model, implying that the primary adsorption mechanism is chemisorption. In the end, the printability of these OHGs with a DLP printer was successfully demonstrated, opening a new frontier for wastewater treatment.

Third Chapter

3 Biobased UV-curable coatings

Increasing environmental pollution and depletion of fossil-fuel research have become central issues in recent years. As a result, many researchers have focused their attention on exploring new thermosets deriving from renewable resources, as already discussed in the first chapter [115,116].

This chapter aims to present different renewable monomers that can be modified and subsequently UV-cured to obtain coatings.

There are two main sections; the first (3.1) concerns the development of cationically photocurable solvent-free epoxy coatings deriving from vanillin, phloroglucinol, cardanols and vegetable oils. The second (3.2) concerns the radical photopolymerization of starch-based coatings.

3.1 Cationically UV-cured coatings

Most of the thermoset polymers are based on epoxy resins, and 60% of epoxy production is intended for the coatings industry [116]. However, the epoxy market is led by diglycidyl ether of bisphenol-A monomer, a reprotoxic substance considered to be toxic. This is one of the reasons why the research interest has been driven to develop green alternatives.

Nevertheless, the majority of biorenewable epoxy monomers have been crosslinked using a conventional thermo-curing process. Only, few data have been reported on biobased cationic UV-curable coatings, which is particularly interesting for coatings production since it does not require an inert atmosphere, and the reaction can continue after the UV source is removed.

With the aim of filling this gap, this first part of Chapter 3 will describe different cationically UV-curable systems. Section 3.1.2 reportes the investigation on coatings obtained from vanillin, phloroglucinol and castor oil epoxy derivatives. In section 3.1.3 epoxy cardanol-based coatings are investigated. In section 3.1.4 coatings obtained from twelve epoxidized vegetable oils are analysed. In the section 3.1.5, the corrosion protection effectiveness of three epoxidized vegetable oils coatings is studied.

3.1.1 Experimental Section

Fourier transform infrared spectroscopy (FTIR)

A Nicolet iS 50 Spectrometer was used to collect the FTIR spectra. The samples were analysed in transmission mode in the air. The photocurable formulations were coated on a silicon wafer (average film thickness 12-20 μm). The wavelength range of collected spectra was 500–4000 cm^{-1}, with a collection rate of 1 scan for 1.2 s and a spectral resolution of 4 cm^{-1}. Two spectra before and after the irradiation were recorded on the same formulation. The UV lamp used was a DIMAX lamp.

The software used to record and analyse the spectra was Thermo Scientific™ OMNIC™ Spectra. All measurements were recorded in triplicates.

Gel content

The gel content of the UV-cured films was determined by weighting the sample before and after 24h of extraction with chloroform at room temperature, according to the standard test method ASTM D2765-84. Using the following formula:

$$G\% = \frac{W_i}{W_0} * 100, \tag{3.1}$$

Differential scanning calorimetric analysis (DSC)

Differential scanning calorimetric analyses were carried out on a Mettler Toledo DSC instrument at a heating rate of 10°C/min using a nitrogen atmosphere. Samples (10–12 mg) were sealed in a 100 μl aluminium pan with pierced lids.

Dynamic thermal mechanical analysis (DMTA)

Dynamic thermal-mechanical analyses were performed with Triton Technology. Samples with dimensions 1 x mm x 7 mm x 0.2 mm were tested with uniaxial stretching performed with a heating rate of 3°C/min, frequency of 1Hz and strain of 0.02%. The storage modulus (E') and the loss factor (Tanδ) were recorded as a function of temperature. The tanδ is the ratio loss modulus/storage modulus = E''/E', the maximum of the Tanδ can be taken as the Tg of the films. To estimate the apparent cross-linking density (ν_c), also known as strand density, the storage modulus values in the rubbery plateau region (E'_R) were extracted from the graph at generally 50°C above the glass transition temperature. Equation 3.2. was used to calculate the ν_c. This equation was derived from the statistical theory of rubber elasticity, which is just an approximation to model the system and therefore was used only to qualitatively compare the level of crosslinking among the obtained networks [53,117].

$$\nu_c = \frac{E'_R}{3RT} \tag{3.2}$$

where ν_c is the number of moles of network chains per unit volume of the cured network, R is the gas constant, T is the absolute temperature (i.e. at T_g+50°C).

Contact angle

Contact angle measurements were performed with a Kruss DSA10 instrument, equipped with a video camera and an image analyzer. Analyses were made at room temperature using the sessile drop technique. Three to five measurements were performed on each sample, and the values averaged. The measuring liquids were doubly distilled water (γ=72.1 mNm^{-1}). Additionally, the surface free energy (γ) was determined based on Owens-Wendt-Rabel-Kaelble (WORK) method [118]. The measuring liquids were double distilled water (γ = 72.8 mN/m) and hexadecane (γ =27.6 nN/m).

Viscosity measurements

Viscosity measurements were conducted using an Anton Paar MCR302 rheometer. The analyses were performed at 20°C with a cone-plate set-up (CP50-1) and a gap of 0.05 mm. The cone had a diameter (⌀) of 25 mm, and a cone-angle (α) of 1°. The viscosity of the samples was recorded by varying the shear rate ($\dot{\gamma}$) from $\dot{\gamma}$=100 s^{-1} to $\dot{\gamma}$=0.1 s^{-1}. To describe the rheological behaviour of the oils, the Power Law model (two terms model, Eq.3.3) and the Sisko model (three-term model, Eq. 3.4) [119] were used:

$$\eta = K\dot{\gamma}^{n-1} \tag{3.3}$$

$$\eta = \eta_\infty + K\dot{\gamma}^{n-1} \tag{3.4}$$

where η is the viscosity, $\dot{\gamma}$ is the shear rate, K is the consistency index, n the flow behaviour index and η_∞ is the viscosity at infinite shear rate.

Thermogravimetric analysis (TGA)

Thermogravimetric analysis was performed with a Mettler Toledo TGA/SDTA 851e to investigate the thermal stability of the obtained coatings. Samples (10-12mg) were inserted in alumina crucibles and heated at 10°C/min from 30°C to 700°C under N_2 flux.

Pencil hardness

The pencil hardness test was performed using pencils of different grades starting from the 6H and continuing down the scale testing with softer and softer pencils according to ASTM D3363-74 [120]. The pencils were maintained at 45° and pushed for at least 6 mm with uniform pressure and speed onto the coating surface. The hardness of the coating was taken as that of the hardest pencil, which caused a cut less than 3mm long out of the 6 mm test push on the surface of the coating.

Adhesion measurement

The coating adhesion measurement was analysed according to the ASTM D3359-B [121]. The surface of each coating was scratched both vertically and horizontally

with a blade holding 6 teeth, separated from each other by a 2 mm distance. A strip of adhesive tape was then applied and subsequently pulled away at a 180° angle. The percentage of squares where the coating is still intact is reported.

Solvent rub resistance test

The coating chemical resistance was evaluated by methyl ethyl ketone double rub test according to the ASTM D5402 [122]. Double rubs were performed until the substrate was exposed or for a maximum of 200.

Electrochemical characterizations

Electrochemical measurements were used to characterize the corrosion behaviour of the different coatings. All measurements, performed using an Ivium-n-Stat potentiostat, were carried out in a 3-electrode electrochemical cell, using an Ag/AgCl electrode as the reference electrode (RE), a Ni-Cr wire as the counter electrode (CE) and the coated steel sample as the working electrode (WE), as commonly done for corrosion experiment [123]. Tests were performed in a 0.1 M NaCl (sodium chloride) aerated solution at T = 20°C. This solution was chosen to simulate a moderately aggressive environment containing chlorides, as the investigated coatings are not specifically designed for seawater applications. The exposed sample surface was 0.78 cm^2; all presented results are scaled to the equivalent area of 1 cm^2.

Two techniques were used to investigate the corrosion protection effectiveness of the coatings: Potentiodynamic Polarization and Electrochemical Impedance Spectroscopy (EIS). Measurements were performed after monitoring the Open Circuit Potential (OCP) of the sample for one hour to reach a steady state of the system under study. Polarization curves were acquired in the range between – 0.3 V *vs* OCP and + 2.7 V *vs* OCP, using a scan rate of 0.166 mV/s and a step size of 1 mV; three samples were tested for each coating formulation. To characterise the corrosion kinetics, results from potentiodynamic polarization measurements were analysed using Tafel extrapolation.

Morphological characterization

A Field Emission Scanning Electron Microscope (FESEM Supra 40, ZEISS) was used to characterize the surface of the coatings after 2-week immersion tests in NaCl solution. The acceleration voltage was set at 5 kV with an aperture size of 30 μm.

3.1.2 Cationic photopolymerization of bio-renewable epoxidized monomers

This section is based on the original research article titled "*Cationic photopolymerization of bio-renewable epoxidized monomers*". The paper was

published in Progress in Organic Coatings in 2019. https://doi.org/10.1016/j.porgcoat.2019.03.054 [124].

This section reports the cationic photopolymerization of vanillin, phloroglucinol and castor oil epoxy derivatives. The reactivity of those monomers and the thermo-mechanical properties of the obtained thermosets are discussed in relationship with the monomer structures.

3.1.2.1 Materials and Methods

Materials

Epoxidized castor oil (ECO, SP-3S-30-005), Phloroglucinol trisepoxy (PHTE, SP-9S-5-003) and Diglycidylether of vanillyl alcohol (DGEVA, SP-9S-5-005) were synthesized and provided by SPECIFIC POLYMERS (Fig. 3.1). The specification of the biobased epoxidized monomers is reported in Tab. 3.1. Triarylsulfonium hexafluoroantimonate used as photoinitiator was purchased from Aldrich.

Photocuring of epoxidized monomers

The epoxy monomers were mixed with 4%wt of photoinitiator, then coated on a polypropylene (PP) substrate and covered with another PP foil to protect the specimen from the atmosphere and ensure a homogeneous thickness of 100µm. The films were irradiated with a Fusion Lamp with a 6 m/min conveyor belt speed and 224 mW/cm^2 light intensity.

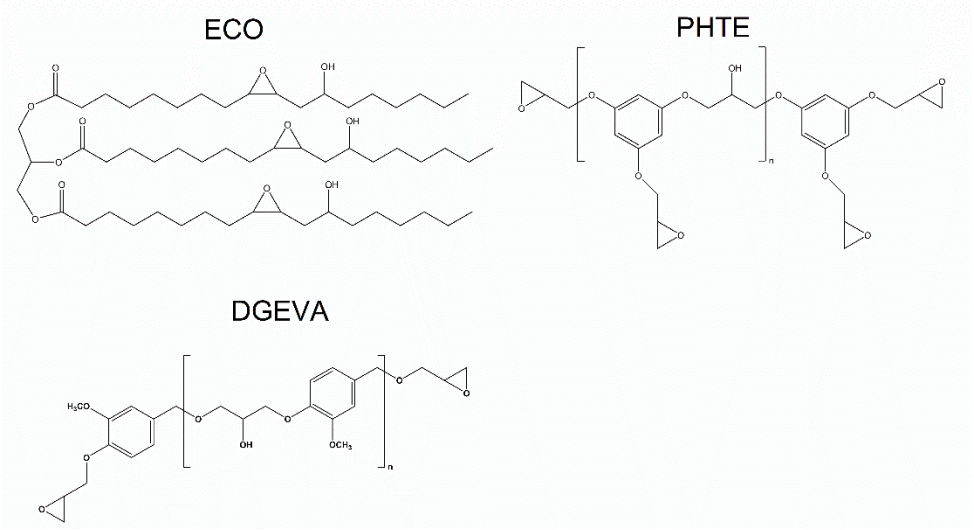

Figure 3.1: Chemical structures of ECO, PHTE and DGEVA.

Table 3.1: Chemical specifications of ECO, PHTE and DGEVA.

	n[a]	Hydroxyl content [m_{eq}/g]	Glycidil index[b] [m_{eq}/g]
ECO	/	/	2.89
PHTE	0.03	0.323	7.28
DGEVA	0.15	0.109	6.78

[a]Average number of monomer units determined by ^{1}H-NMR, [b]Values obtained by ^{1}H-NMR titration evaluated by Specific Polymers.

3.1.2.2 Results and discussion

The reactivity of the three epoxidized biobased monomers was evaluated by FTIR spectroscopy by following the decrease of the peak at 760 cm^{-1}, as described in the experimental section. Fig. 3.2 reports the FTIR spectra before and after the irradiation, while the calculated epoxy group conversions are reported in Tab. 3.2. All the formulations led to free-standing, fully cured films.

The ECO formulation reached the highest epoxy conversion (85%). This result can be explained by looking at the ECO Tg, which is lower than room temperature. Hence, the flexible network gives the polymeric chains high mobility allowing them to reach a high epoxy conversion.

On the contrary, the DGEVA rigid aromatic structure led to early vitrification, hindering the mobility of the chains and reducing the propagation rate of the macro-carbocationic, which led to a low epoxy conversion (60%).

However, even if the PHTE monomer is trifunctional and possesses an aromatic structure, its epoxy groups conversion reached 80%. At the same time, its Tg was only 42° C, which is lower than the DGEVA one. This can be explained considering the high amount of -OH groups in the PHTE structure, which may be involved in an activated monomer mechanism (AM), leading to the formation of flexible ether structures. In fact, the AM mechanism may occur when the hydroxyl group nucleophilically attacks the growing ionic chain-end during the cationic reaction, leading to the formation of a pronated ether. Subsequently, the proton transfers to another epoxy monomer, starting a new chain, terminating the previous one. These flexible ether structures can have increased the final epoxy conversion delaying the vitrification.

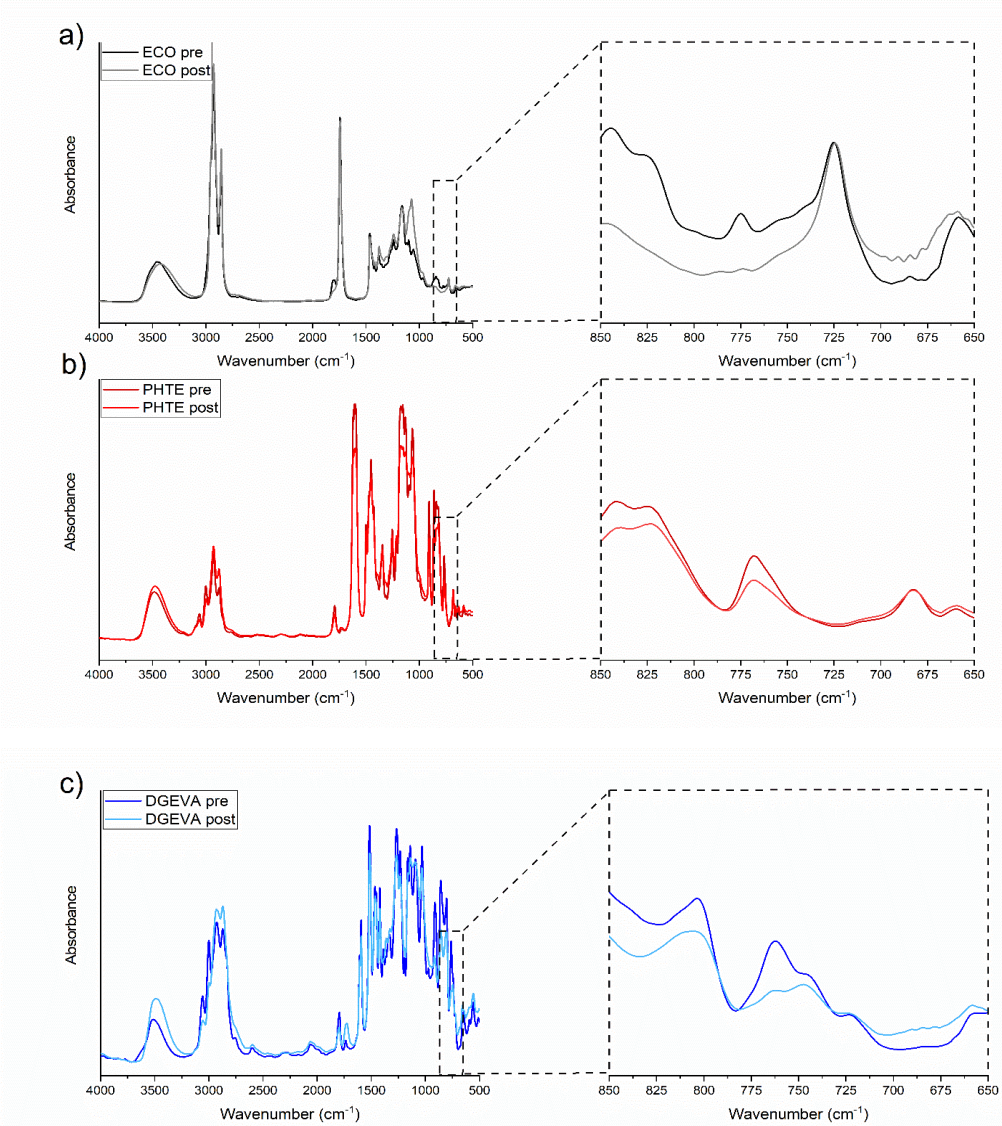

Figure 3.2: FTIR spectra pre and post UV- irradiation of a) ECO, b) PHTE, and c) DGEVA.

The thermal and thermo-mechanical properties of the UV-cured films were characterized using DSC and DMTA analysis (Tab.3.2). In Fig.3.3, a are reported the Tanδ curves of the biobased crosslinked networks; the maximum of the Tanδ is assumed to be the Tg of the material.

As can be noticed, the Tg values obtained from the DSC are lower than the ones registered by DMTA. This outcome was already observed in previous research and can be attributed to the frequency effect [125]. The obtained Tg values are in good agreement with the epoxy group conversion previously discussed. The presence of rigid aromatic structures of DGEVA and PHTE leads to higher Tg concerning the ECO, which instead possess an aliphatic structure. The lower Tg of PHTE with

respect to DGEVA can be explained again considering the formation of flexible ether structures via the AM mechanism.

Other considerations can be made considering the shape of the Tanδ curves from Fig.3.3. The ECO Tanδ have a sharp peak compatible with the formation of a homogeneous network, while the PHTE Tanδ is broader and shorter, which indicates the formation of a highly cross-linked network but with a certain degree of inhomogeneities. The Tanδ of DGEVA shows a main peak at 82°C and a shoulder at 120°C. This behaviour is consistent with the formation of a heterogeneous network [126].

The hydrophobicity of the thermosets surfaces was evaluated by water contact angle measurements (Fig.3.3,b). The values are reported in Tab.3.2. The ECO film surface possesses the highest hydrophobicity as expected from its long aliphatic chains, while the PHTE and DGEVA surfaces are more hydrophilic with very similar contact angles of about 73 and 75°, respectively.

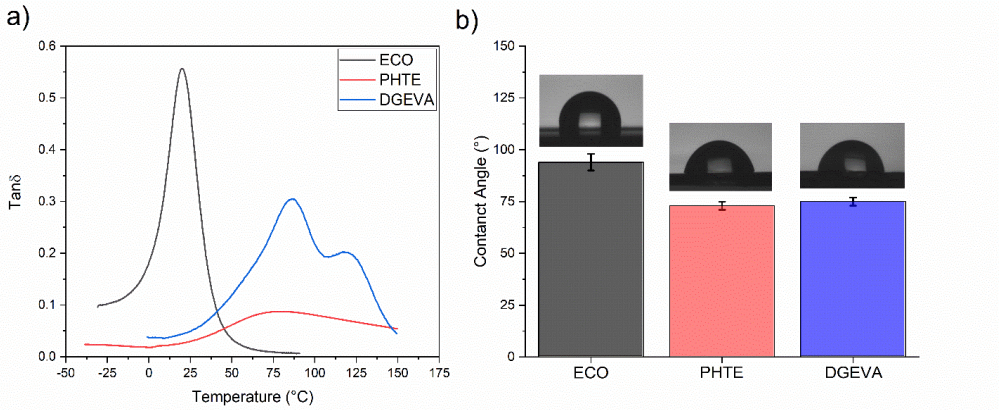

Figure 3.3: a) Tanδ curves and b) contact angle measurements of ECO, PHTE and DGEVA thermosets.

Table 3.2: Properties of the photocrosslinked thermosets.

	Epoxy group conversion [%]	**Tg_{DSC} [°C]**	**Tg_{DMTA} [°C]**	**ϑ [°]**
ECO	85	10	20	94 ± 4
PHTE	80	42	75	73 ± 2
DGEVA	60	82	83 (120)	75 ± 3

3.1.2.3 Conclusions

This work exploits the cationic photocuring of three different biobased epoxy monomers. In all cases, fully crosslinked films were obtained with a wide range of thermal and mechanical properties, which were discussed according to their molecular structures. The long aliphatic chains of ECO give the polymer chains enough mobility to reach a high epoxy group conversion leading to the formation of hydrophobic flexible films. While the rigid aromatic structure of DGEVA induces early vitrification and, consequently, a lower epoxy conversion. Unlike the previous ones, even if the PHTE possesses an aromatic structure, possess a high epoxy group conversion but a low Tg. This can be attributed to its high amount of -OH groups which may have activated the AM mechanism leading to the formation of flexible ether groups enhancing the chain mobility.

Therefore, in this section, new biobased monomers have been successfully used to create cationically UV-curable films.

3.1.3 Cationic UV-curing of epoxidized cardanol derivatives

This section is based on the original research article titled " *Cationic UV-curing of epoxidized cardanol derivatives*". The paper was published in Polymer International in 2020. https://doi.org/10.1002/pi.6031 [127].

This section reports the cationic photopolymerization of cardanol-based epoxy monomers. Cardanols are cheap and abundant by-products of the cashew industry. They are constituted by a phenol moiety meta substituted by a C_{15} alkyl chain. The alkyl chain can have four different types of unsaturations: 8.4% saturated chains, 48.5% mono-olefinic chains, 16.8% diolefinic chains and 29.33% triolefinic chains [128].

The reactivity of those monomers toward the cationic photopolymerization has been investigated, and the thermo-mechanical properties of the obtained thermosets are discussed in relationship with the monomer structures.

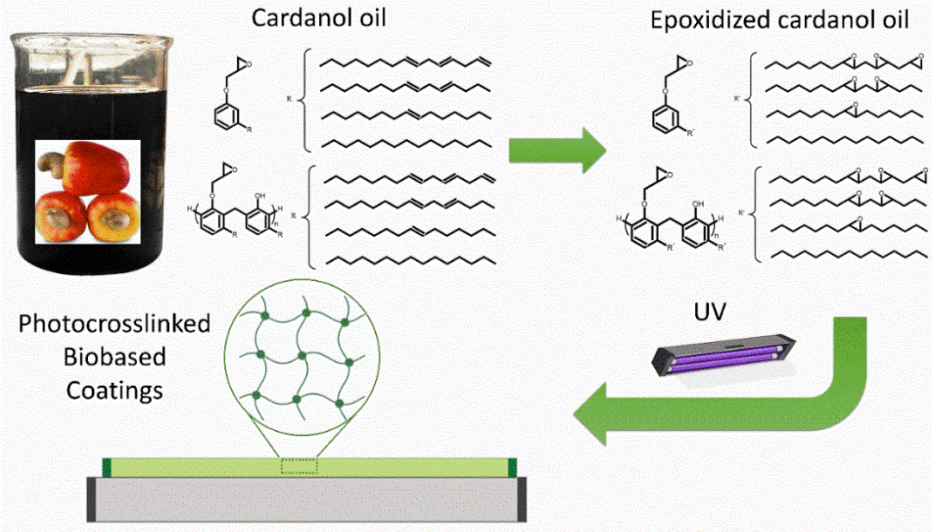

Figure 3.4: Graphical representation of the cardanol oils epoxidation and UV-curing.

3.1.3.1 Materials and Methods

Materials

Epoxidized Cardolite NC-513 (SP-ECO-84), epoxidized Cardolite LITE 2513HP (SP-ECO- 85) and epoxidized Cardolite NC-547 (SP-ECO-86) were synthesized as provided by Specific Polymers (Montpellier, France). Their chemical structures are reported in Fig.3.5, and their properties are summarized in Tab.3.3. The cationic photoinitiator triarylsulfonium hexafluoroantimonate salts mixed to 50 wt% in propylene carbonate was purchased from Sigma Aldrich.

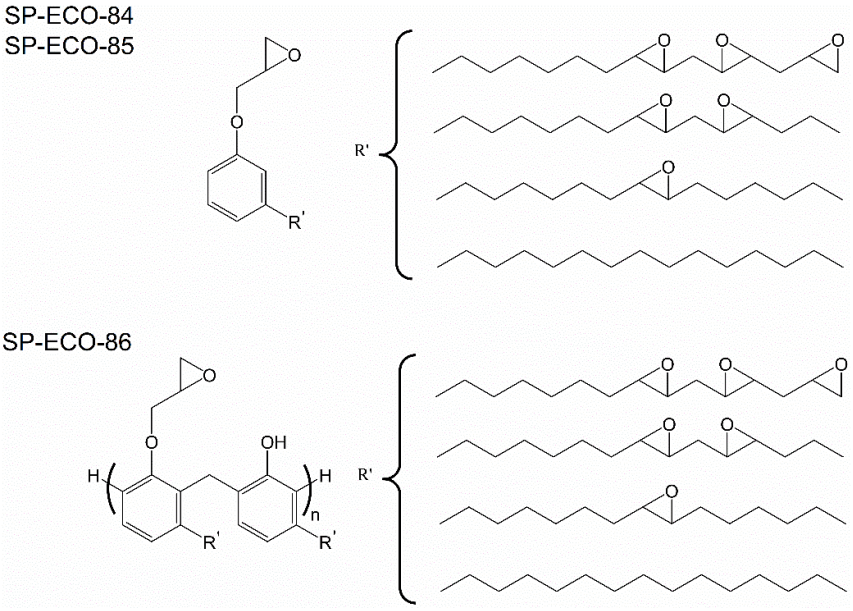

Figure 3.5: Chemical structures of the epoxidized cardanols oils.

Table 3.3: Specifications of the epoxidized cardanols derivatives.

	Glycidyl index [m_{eq}/g][a]	**Epoxy index [m_{eq}/g][b]**
SP-ECO-84	1.74 – 2.35	3.88
SP-ECO-85	2.22 – 2.6	3.89
SP-ECO-86*	1.18 – 1.82	2.82

[a]Value obtained from Cardolite Corporation; [b]Value obtained from ^{1}H-NMR titration evaluated by Specific Polymers; *n value in the SP-ECO-86 was not determined.

Photocuring of epoxidized cardanol derivatives

The epoxy cardanol derivatives were mixed with 4%wt of photoinitiator, then coated on a PP substrate (100μm). The films were irradiated for 1.52 s with a Fusion Lamp having a conveyor belt speed of 6 m/min and 235 mW/cm^2 light intensity.

3.1.3.2 Results and discussion

The reactivity of the SP-ECO cardanols was investigated by FTIR measurements by following the decrease of the double peaks ranging from 829 to 818 cm^{-1} which can be attributed to the epoxy rings (Fig.3.6). The epoxy ring-opening reaction was further confirmed by the increase of the C-O-C peaks centred at 1118 and 1050 cm^{-1}. In all cases was possible to obtain tack-free films with an epoxy conversion ranging from 64 to 72%, as reported in Tab.3.4.

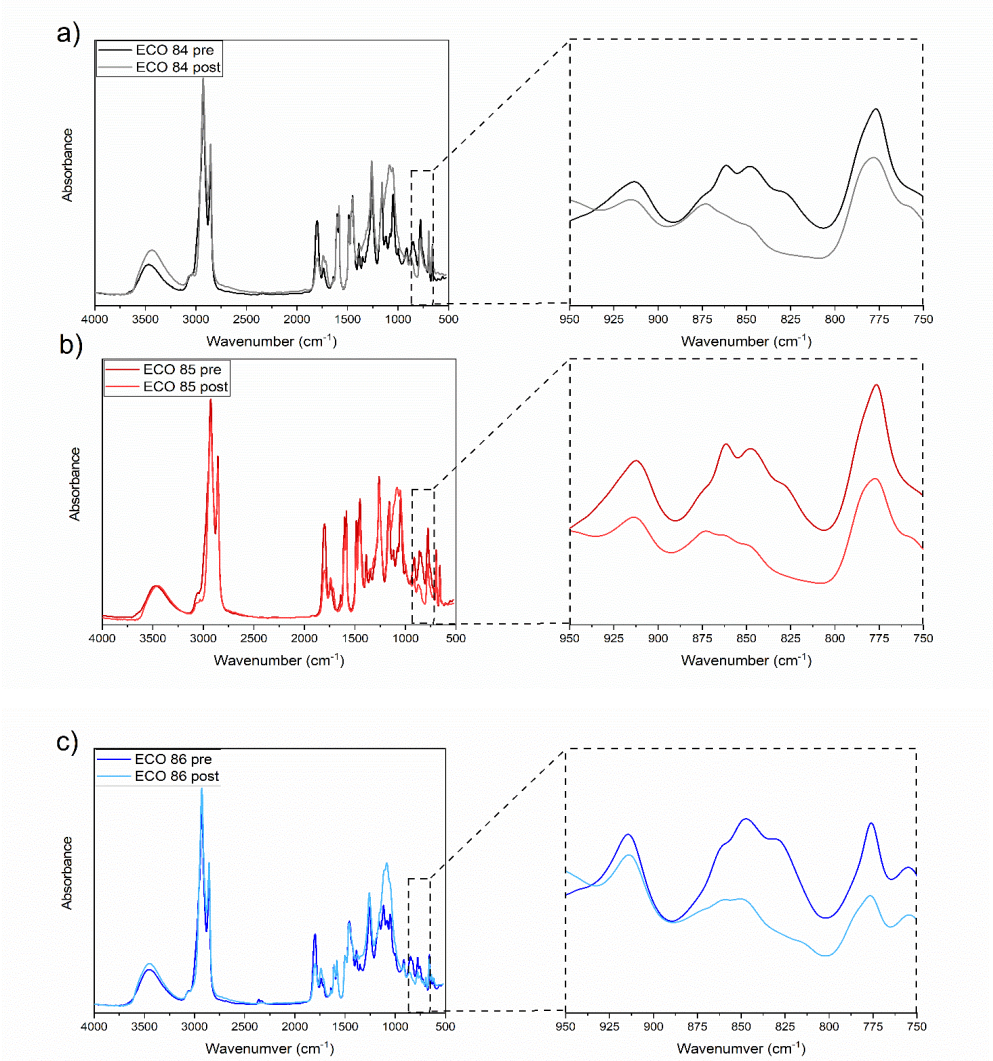

Figure 3.6: FTIR spectra of a) ECO 84, b) ECO 85 and c) ECO 86 recorded before and after the irradiation.

The thermal and viscoelastic properties of the obtained thermosets were analysed by DSC and DMTA analysis. The Tg values are reported in Tab.3.4, while the Tanδ and the E' curves are reported in Fig.3.7. As observed, the SP-ECO-85 has a higher Tg value with respect to SP-ECO-84, despite a similar chemical structure (Fig.3.5). This can be explained considering that the SP-ECO-85 possess a slightly higher glycidyl content with respect to SP-ECO-84 (Tab.3.3), which led to the formation of higher numbers of crosslinks and thus higher Tg. The high Tg of SP-ECO-85 can also induce vitrification hindering the chain mobility and therefore causing a lower epoxy groups conversion. On the contrary, the SP-ECO-86 possesses the highest Tg value even if it has the lowest epoxy content with respect to the others. This can be attributed to its polyaromatic structure. Moreover,

the ECO 86 Tanδ reported in Fig.3.7 presents a broad and relatively low peak ascribing to a highly crosslinked network. From Fig.3.7, it can also be observed that the Tanδ broadens from ECO 84 to ECO 85, so with the epoxy groups, enhancement results in broader branching modes and structures distribution.

In Tab.3.4 are also reported the values of the crosslinking density ν_c obtained from the E'_R value as described in the experimental section. The low ν_c of ECO 86 is consistent with its low epoxy group conversion.

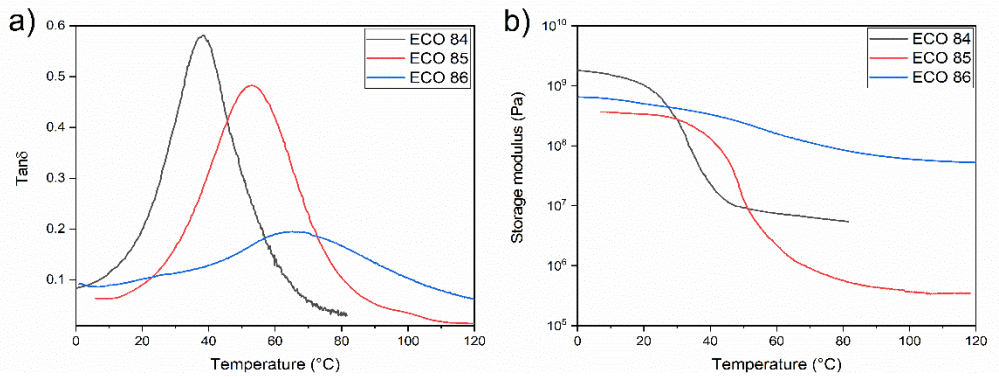

Figure 3.7: a) Tanδ and b) Storage modulus of the ECO 84, ECO 85 and ECO 86.

Table 3.4: Properties of the UV-cured cardanols thermosets.

Thermoset	**ECO-84**	**ECO-85**	**ECO-86**
Starting monomer	SP-ECO-84	SP-ECO-85	SP-ECO-85
Epoxy group conversion [%]	72	64	66
T_{g_DSC} [°C]	25	36	53
T_{g_DMTA} [°C]	38	53	65
E' [MPa]	1810.63	323.37	648.59
E_R' [MPa]	5.14	0.61	53.48
ν_c [mol/dm^3]	0.601	0.065	5.527

3.1.3.3 Conclusions

In this section, epoxy cardanol derivatives have been successfully UV-cured. Their reactivity ranges from 64 to 72 %, as evidenced by FTIR analysis. The thermal and thermo-mechanical properties of the crosslinked thermosets were investigated by DSC and DMTA analyses. The Tg value can be enhanced by either increasing the epoxy rings in the monomer structure or by selecting polyaromatic structures. Therefore, this section successfully demonstrated the possibility to obtain fully crosslinked thermosets from biobased by-products of the cashew industry. Moreover, by carefully selecting the starting monomer, different final thermomechanical properties can be achieved.

3.1.4 Cationic photopolymerization of epoxidized vegetable oils

This section is based on the original research article titled " *Sustainable access to fully biobased epoxidized vegetable oil thermoset materials prepared by thermal or UV-cationic processes*". The paper was published in RSC Advances in 2020. DOI: 10.1039/d0ra07682a [129].

In this section, a detailed investigation of the photopolymerization of 12 different epoxidized vegetable oils (EVOs) is reported (Fig.3.8). The thermal and mechanical properties of the UV-cured epoxidized vegetable oils thermosets are discussed. This section points out the possibility to obtain tuneable thermomechanical properties by a simple careful selection of the starting EVO.

.

Figure 3.8: List of the twelve vegetable oils epoxidized with a green synthesis procedure by Specific Polymers used in this work.

3.1.4.1 Materials and Methods

Materials

Epoxidized vegetable oils were synthetized and provided by Specific Polymers. Their names and composition are reported in Tab.3.5, while in Fig.3.9, the most common fatty acids are shown. The cationic photoinitiator triarylsulfonium hexafluoroantimonate salt, mixed 50 wt% in propylene carbonate were purchased from Sigma Aldrich (Milan, Italy).

Table 3.5: Composition of the EVOs.

	Origin	Edible	Initial composition				Final epoxy index [m_{eq}/g]
			Saturated fatty acids [%]	Mono-unsaturated fatty acids [%]	Di-unsaturated fatty acids [%]	Tri-unsaturated fatty acids [%]	
EVO 1	Karanja	no	22	56	21	1	2.77
EVO 2	St John's wort	No	21	63	16	/	2.97
EVO 3	Peanut	Yes	20	53	27	/	3.33
EVO 4	Rapeseed	No	7	62	25	7	3.96
EVO 5	Soybean	Yes	16	26	49	8	4.54
EVO 6	Rose hip	No	17	20	57	5	4.7
EVO 7	Safflower	/	12	18	70	/	5.0
EVO 8	Camelia	/	10	30	28	32	5.27
EVO 9	Hemp	/	10	12	65	13	5.6
EVO 10	Rose hip	No	5	16	46	36	6.3
EVO 11	Linseed	Yes	10	19	13	58	6.6
EVO 12	Perilla	/	3	21	18	58	6.77

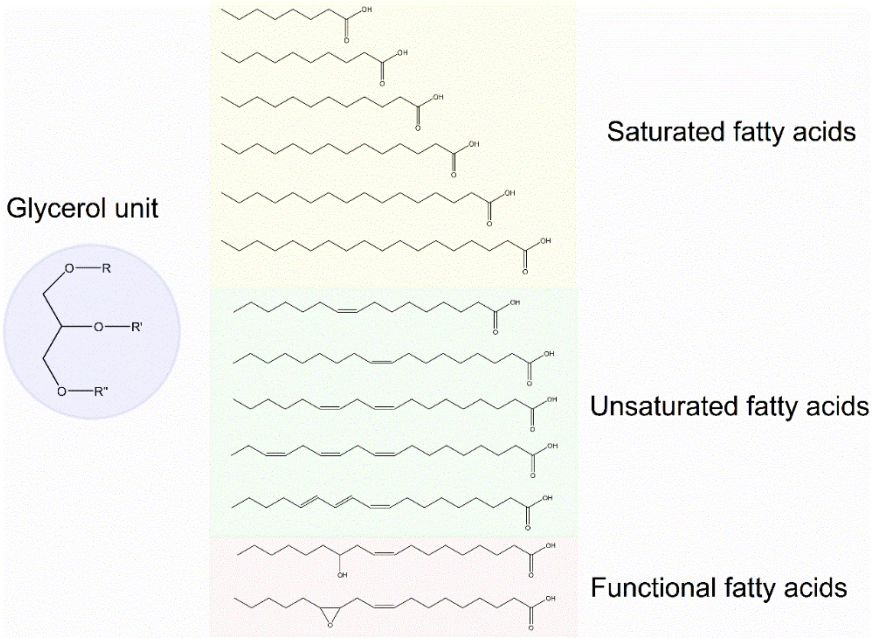

Figure 3.9: General triglyceride structure with the most common fatty acids.

Photocuring of epoxidized vegetable oils

The EVOs were mixed with 2%wt of photoinitiator, then coated on a PP substrate (100µm). The films were irradiated for 1.52 s with a Fusion Lamp having a conveyor belt speed of 6 m/min and 225 mW/cm^2 of light intensity.

3.1.4.2 Results and discussion

The reactivity of the epoxidized vegetable oils was evaluated by FTIR measurements; the collected spectra before and after the UV-irradiation are reported in Fig.3.10. The epoxy groups conversions were evaluated by following the decrease of the peaks centred at 822 and 833 cm^{-1} and are reported in Tab.3.6. All the EVOs achieved high epoxy conversions >90% except for the EVO 1, which instead did not polymerize. One possible explanation for the EVO 1 behaviour is the presence of natural flavonoids like karanjin and pongamol having a UV-shielding effect [130].

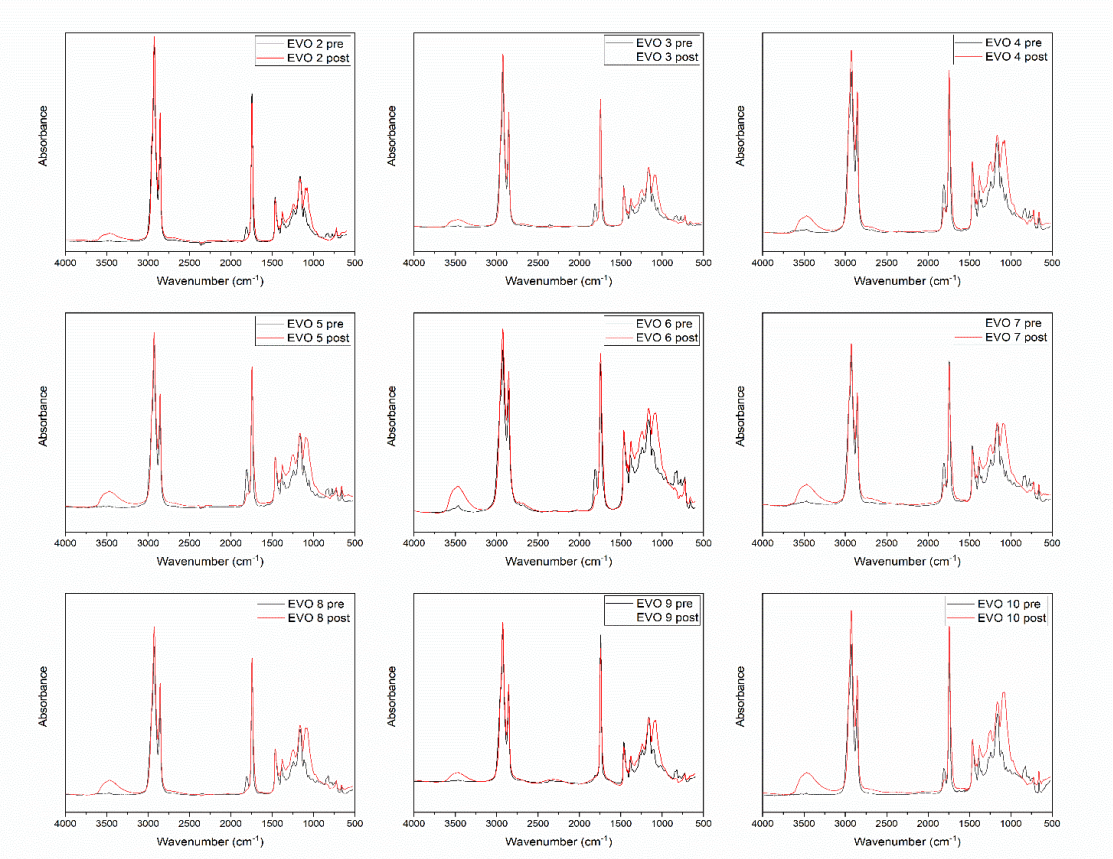

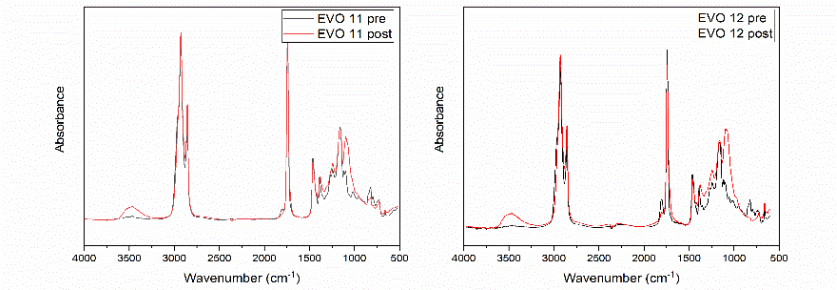

Figure 3.10: FTIR pre and post of the EVOs formulations.

The thermal and thermo-mechanical properties of the EVOs UV-cured films were subsequently evaluated by means of DSC and DMTA analyses. All the results are reported in Tab.3.6. As can be observed, the Tg value increases with enhancing the epoxy index (EI) in the EVO structure. Considering that all the EVOs possess similar epoxy conversion, the EI can be regarded as the major parameter influencing the Tg of the thermosets. So, it is clear that by simply changing the starting EVO, it is possible to modulate the final Tg in a broad range of temperatures (Fig.3.11).

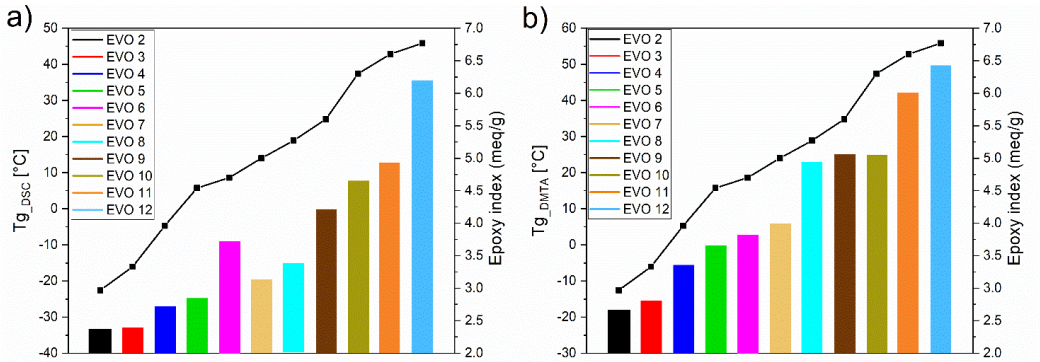

Figure 3.11: Correlation between a) Tg_DSC and b) Tg_DMTA with the epoxy index.

In Fig. 3.12 are reported the Tanδ and the E' of the EVOs. As can be noticed, the Tanδ peaks lower and broaden as the epoxy content increases, indicating an enhancement in network heterogeneity and variety of chain segment mobility [131,132]. Furthermore, the E' and the ν_c values of the biobased thermosets increase with increasing EI.

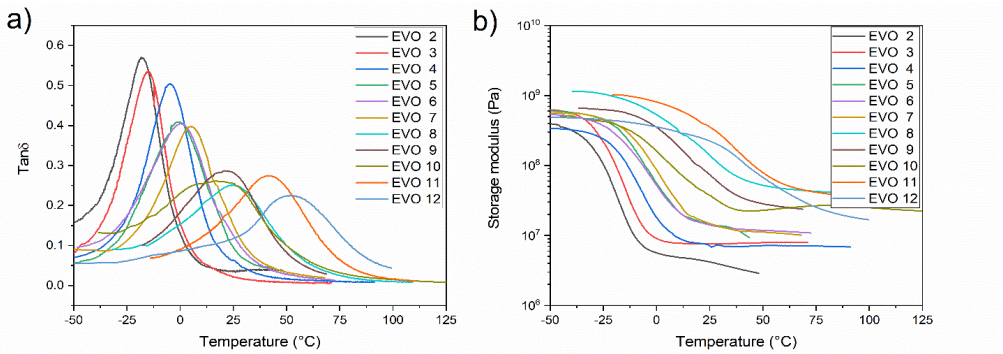

Figure 3.12: a) Tanδ and b) Storage modulus plots of the EVO thermosets.

Table 3.6: Properties of photocured EVO thermosets

	Epoxy conversion [%]	**$Tg_{\_DSC}$ [°C]**	**$Tg_{\_DMTA}$ [°C]**	**$E'_{glass\ state}$ [MPa]**	**ν_c [mmol/cm^3]**
EVO 1	/	/	/	/	/
EVO 2	97	-34	-18	3.71	0.49
EVO 3	91	-33	-15	7.67	1.00
EVO 4	91	-27	-5	7.13	0.90
EVO 5	91	-25	0	9.34	1.16
EVO 6	96	-8	3	11.70	1.44
EVO 7	93	-20	6	10.90	1.33
EVO 8	99	-25	23	43.08	4.99
EVO 9	92	0	25	23.75	2.74
EVO 10	92	8	25	26.63	3.07
EVO 11	90	13	42	35.30	3.88
EVO 12	94	36	50	16.72	1.80

In Section 3.1.2, the thermal properties of epoxidized castor oil were reported. This EVO possesses 2.85 m_{eq}/g, and its Tg reached 10 and 20°C with DSC and DMTA, respectively. However, in this section, closer Tg values are reached by EVO 10, which has a much higher EI (6.3 m_{eq}/g). This result can be explained considering the ECO composition, which is mainly constituted by ricinoleic acid baring hydroxyl groups alongside. Therefore, the presence of -OH groups strongly influences the final properties of the thermoset, deriving either by the formation of hydrogen bonds (supramolecular effect) or by interacting with the cationic species during the polymerization.

3.1.4.3 Conclusions

In this section, twelve different epoxidized vegetable oils (EVOs) have been investigated. The EVOs possess different epoxy indexes based on their initial fatty acid composition. All the EVOs showed high reactivity towards cationic photopolymerization, always reaching more than 90% of final epoxy group

conversion. This section demonstrated that the main parameter influencing the final thermal and themo-mechanical properties of the thermosets was the EI. Linear Tg enhancement was observed as the EI increased. So, it is clear that by carefully choosing the starting epoxidized vegetable oil, it is possible to modulate the final properties of the crosslinked network (e.g. Tg ranging from -19 to 50°C).

3.1.5 Anticorrosion resistance coatings from vegetable oils

This section is based on the original research article titled " *New UV-Curable Anticorrosion Coatings from Vegetable Oils*". The paper was published in Macromolecular Materials and Engineering in 2021. https://doi.org/10.1002/mame.202100029 [133].

This section reports a detailed investigation of three biobased thermoset coatings obtained from epoxidized rosehip and grapeseed oils with potential applicability in the field of anticorrosion coatings (Fig.3.13). Initially, the viscosity of the oils was investigated with a rheology test. Then, the formulations were UV-cured *via* the cationic process. Subsequently, the thermal and mechanical properties of the thermosets were evaluated by DSC and DMTA analyses. Then, the thermal stability and surface properties of the bio-based coatings, such as pencil hardness, adhesion, solvent resistance, and contact angle, were analysed. Furthermore, to evaluate the possible applicability of the coatings for corrosion protection, the formulations were crosslinked on mild steel substrates, and electrochemical characterizations were performed.

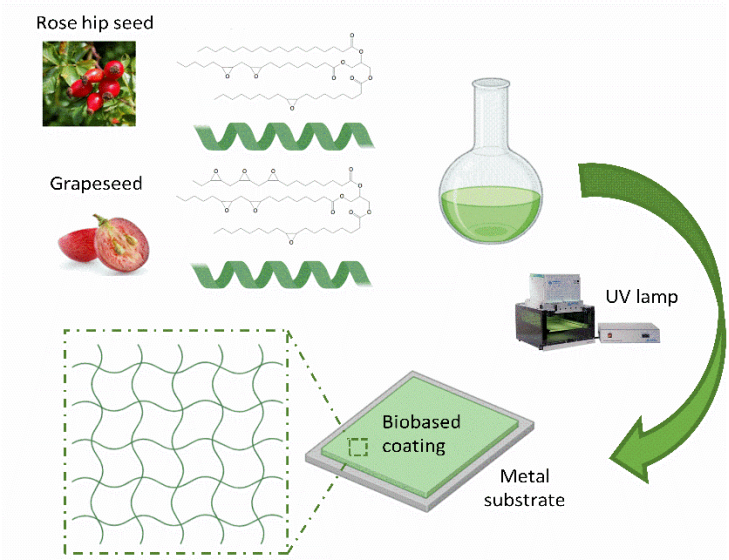

Figure 3.13: Schematic representation of the EVOs UV-curing.

3.1.5.1 Materials and Methods

Materials

Epoxidized vegetable oils (EVOs) were synthesized and provided by Specific Polymers. Their names and composition are reported in Tab.3.7. The triarylsulfonium hexafluoroantimonate salt, mixed 50 wt% in propylene carbonate were purchased from Sigma Aldrich (Milan, Italy).

Table 3.7: Composition of the starting EVOs.

EVO	Origin	Epoxy index [m_{eq}/g]
ERHO-4.5	Rosehip seed	4.7
EGRP-5	Grapeseed	5.5
ERHO-6	Rose hip seed	6.3

Photocuring of epoxidized vegetable oils

The EVOs were mixed with 2%wt of photoinitiator, then coated on a PP substrate (100μm). The films were irradiated for 15 s under a Dymax ECE 5000 Flood lamp for 15 with a light intensity of 95 mW/cm^2. All the polymerization reactions were performed at room temperature at constant humidity (RH = 25–30%).

3.1.5.2 Results and discussion

Initially, the viscosity of the liquid formulations was evaluated since it has a significant impact on the coating applicability and performance. In Fig. 3.14 are reported the oils viscosities as a function of the shear rate. As can be observed, the epoxidized rosehip seed oils showed a Newtonian behaviour since their viscosity has a constant value in the range of $\dot{\gamma}$ tested. Instead, the grapeseed oil showed a shear-thinning behaviour since when the $\dot{\gamma}$ increases its η decreases until its value remains constant in a certain $\dot{\gamma}$ interval called "second Newtonian region". Two models are used to describe the η behaviour as reported in the experimental section. The Power Low model correctly describes the rosehip seed oil viscosity behaviour, while the grapeseed fits with the Sisko model (Tab. 3.8).

The viscosity values reported in the Tab.3.8 are higher than those reported in the literature for other vegetable oils available in the market. This viscosity enhancement may be attributed to the molecular weight enhancement ascribing to the epoxidation reaction. In fact, it has already been reported that for saturated fatty acids, the viscosity increases with the increase of the molecular weight [134]. Moreover, the achieved η values are consistent with the one obtained for epoxidized soybean oil [135]. It is also possible to observe η increase with increasing epoxy content, probably due to the formation of hydrogen bonds [136,137].

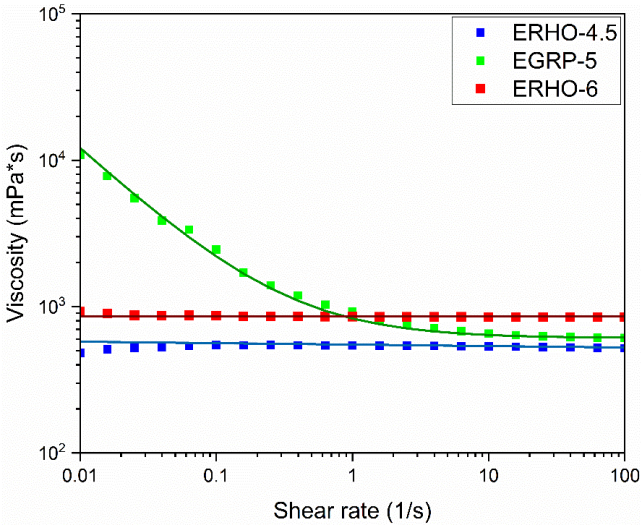

Figure 3.14: Viscosity of the EVOs as a function of the shear rate; ERHO-4.5 and ERHO-6 fitted with the Power Law model while EGRP-5 fitted with the Sisko one.

Table 3.8: Power low and Sisko model parameters.

EVO	Fitting model	K	n	η_∞[mPa*s]	η [mPa*s]
ERHO-4.5	Power law	0.55	0.99		519
EGRP-5	Sisko	0.22	0.14	610	610[a]
ERHO-6	Power Law	0.86	1		845

[a]value was taken in the second Newtonian plateau.

The reactivity of the formulations towards cationic photopolymerization was subsequently evaluated by FTIR measurements. Fig.3.15 reports the FTIR spectra of the EVOs, from which it is possible to identify their typical functional groups. The peaks at 2926 and 2854 cm^{-1} can be assigned to the -CH_2- asymmetrical and symmetrical stretching. The peak at 1745 cm^{-1} represents -C=O ester stretching vibration. The peaks at 1465 and 1378 cm^{-1} are attributed to -C-H (CH_2, CH_3) scissoring and -C-H (CH_2) rocking vibration. The peaks at 1162 cm^{-1} and 1116 cm^{-1} correspond to the -C-O bending and -C-O stretching vibrations. While the double peak at 840 cm^{-1} is attributed to the C-O-C vibration of the epoxy ring.

The success of the UV-curing was confirmed by the reduction of the peak at 840 cm^{-1} ascribing to the epoxy ring-opening reaction. Moreover, in the spectra collected after the irradiation it is also possible to observe the appearance of two new peaks centred at 1090 and 3485 cm^{-1} representing the C-O-C ether and the -OH stretching vibrations, respectively. In all cases was possible to achieve a high epoxy group conversion (>94%).

The high curing efficiency was further confirmed by the obtained high gel fraction (G%) (Tab.3.9).

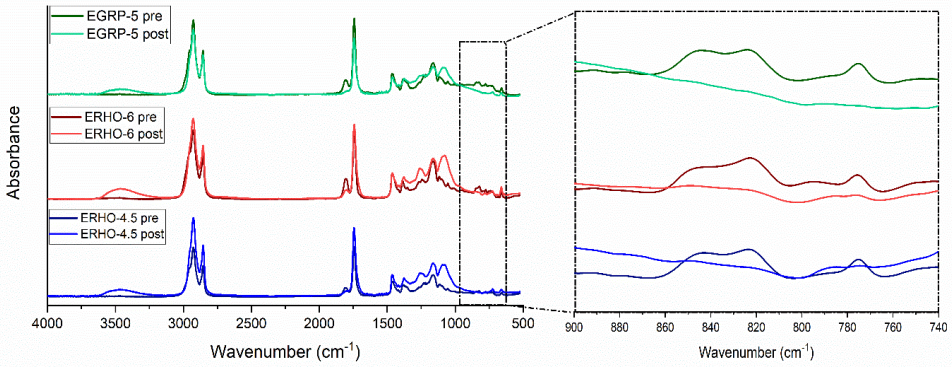

Figure 3.15: FTIR spectra of EVOs recorded before and after the UV-irradiation under DYMAX lamp.

The thermal and viscoelastic properties of the biobased thermosets were analysed with DMTA analysis. The Tanδ curves are reported in Fig.3.16,a. As observed in the previous sections, the Tg increases with the increase of the epoxy index of the starting monomer. It is also possible to notice that the Tanδ of the ERHO-6 is flatter and broader with respect to the others, indicating the formation of a more heterogeneous network with broader distribution of chains relaxations. From the value of the E' in the rubbery plateau, it was possible to evaluate the crosslinking density (ν_c) of the obtained thermoset (see Tab.3.9) by using the theory of rubber elasticity as described in the experimental section. As expected, high EI in the starting EVO leads to higher final ν_c.

The thermal analysis performed on the crosslinked networks confirmed the Tg trend obtained with the DMTA.

The thermal stability of the thermosets was subsequently investigated by TGA analysis. In Fig. 3.16,b are reported the obtained curves. Interestingly, the initial decomposition temperature ($T_{5\%}$) values are similar to those obtained by diglycidyl ether bisphenol A, one of the most used petroleum-based epoxy resin and possess similar char residue [138].

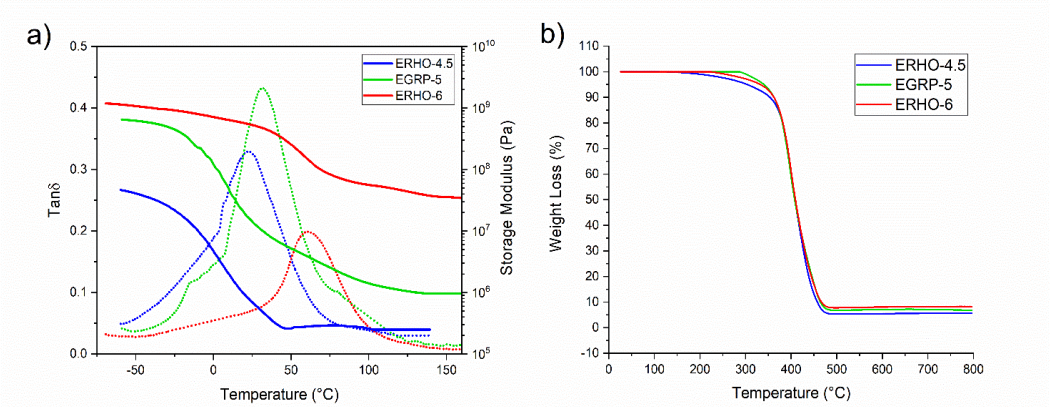

Figure 3.16: a) DMTA and b) TGA curves of the EVOs.

Table 3.9: Properties of the UV-cured films.

EVOs	FTIR conversion (%)	Gel content (%)	Tg_DMTA (°C)	E' at glassy state (MPa)	E' at rubbery plateau (MPa)	Crosslinking density (mmol/cm3)	Tg_DSC (°C)	T5% (°C)	Tpeak (°C)	Char residue (%)
ERHO-4.5	95	94	9	47	0.3	0.03	-10	304	400	6
EGRP-5	99	98	16	653	1	0.38	-5	340	399	7
ERHO-6	93	95	57	1191	23	5.38	23	333	400	8

The solvent resistance of the crosslinked coatings was evaluated via a MEK-resistance test. Thermosets with higher ν_c showed improved chemical resistance (high MEK resistance), as can be observed in Tab. 3.10. The enhancement of the surface properties with higher ν_c was further confirmed by both the hardness and the adhesion test. In fact, as the ν_c increases from 0.03 to 5.38 mmol/cm^{3,} the film hardness increases from 3B to F and its adhesion from 92 to 96 % (Tab.3.10).

The surface properties of the crosslinked films were subsequently evaluated by contact angle measurements. As observed from Tab.3.10, all the surfaces are hydrophobic with a water contact angle >74°, as expected for the presence of long aliphatic chains in the starting monomers. The obtained values are slightly higher than those reported in the literature for UV-cured 3,4-epoxycyclohexylmethyl-3,4-epoxycyclohexane carboxylate (70°), which is petroleum-based epoxy resin [139]. Additionally, the contact angle with diiodomethane was also measured to estimate the surface energy using the WORK method described in the experimental section. All the coatings show very similar surface tension with a value close to 42 mN/m, similar to the value reported for other epoxy petroleum-based resins [140].

Table 3.10: Surface properties of the obtained biobased coatings.

EVO	Solvent resistance	Film hardness	Adhesion test On metal [%]	Water contact angle [°]	Diiodomethane Contact angle [°]	Surface tension [mN/m]
ERHO-4.5	50	3B	92	75.4±2	38.4±5	41.7
EGRP-5	100	F	93	74.9±2	36.9±3	42.4
ERHO-6	>200	F	96	80.7±3	37.1±2	41.4

The corrosion protection performances of the coating were evaluated by two different electrochemical measurements. The experiments and the data interpretation were conducted by Leonardo Iannucci, so in this section are only reported the highlight of these investigations. A detailed description of the mathematical formula used to extrapolate the Tafel parameters and on the Brode diagrams are reported in the published article [133].

Initially, the coatings were coated on a mild steel substrate (20μm thickness) and subsequently UV-cured. The electrochemical measurements were conducted with a three-electrodes cell set up using 0.1 M NaCl aerated solution. The potentiodynamic polarization results demonstrate that the biobased coatings successfully provide good protection for the metal, reducing the current in both the anodic and the cathodic parts of the curve (Fig.3.17). In particular, the ERHO-6 coating showed the lowest corrosion current, the highest E_{corr} and no pitting evidence for the entire scanned anodic overpotential. On the contrary, the ERHO-4.5 showed low I_{corr} and different peaks in the anodic part of the potentiodynamic polarization curve, which may be attributed to local coating breakdowns thus to pitting events. These results are in good agreement with the previous analyses. In fact, higher crosslinked networks showed higher corrosion resistance. Nevertheless, it is clear that in all cases, the presence of the coatings successfully protected the metal substrate.

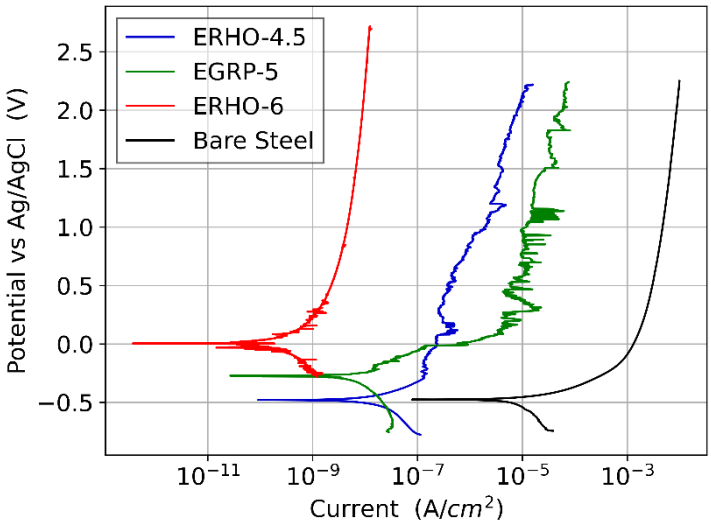

Figure 3.17: Potentiodynamic polarization curves.

To further characterize the corrosion protection effectiveness of the coatings, electrochemical impedance spectroscopy (EIS) was performed. This test is not destructive. Therefore, it helps to determine the stability of the coatings as a function of immersion time by taking different measurements on the same sample at different interval times. In this test, the samples were immersed in the NaCl solution for two weeks. The frequency range tested was from 10^{-2} Hz to 10^{4} Hz with 10 mV of alternating voltage. Higher crosslinked networks showed more stable behaviour, probably ascribing to a lower corrosion medium diffusion into the network leading to improved barrier effect. Interestingly after 72h of immersion time, the EGRP-5 presented a significant impedance modulus reduction above 10^{5} Ohm*cm^2, then remained constant for the rest of the test. Unfortunately, it is important to stress that if the impedance modulus reaches a value lower than 10^{6} Ohm*cm^2, the coating cannot be considered protective [141], therefore the EGRP-5 cannot be considered suitable to protect the metal. On the contrary, ERHO-4.5 and ERHO-6 showed higher impedance moduli: 10^{6} Ohm*cm^2 and 10^{7} Ohm*cm^2, respectively.

After the impedance test, the morphology of coatings surfaces was investigated with FESEM microscopy. As can be observed in Fig.3.18, the morphology of the ERHO-4.5 presents some localized defects. At higher magnification, those defects can be recognized as corrosion products generated in correspondence with local irregularities. While the ERHO-6 shows no significant signs of deterioration and no corrosion products. Instead, the EGRP-5 surface presents extensive damages and corrosion products as expected from the impedance result.

The superior corrosion protection effectiveness showed by ERHO-6 can be attributed to both its higher Tg and its crosslinking density. It was previously demonstrated that networks with higher Tg possess poor swelling capability and water permeability. Furthermore, it is important to notice that all the tests were

performed at 20°C, so the only coatings tested in its glassy state was ERHO-6. The glassy state of the ERHO-6 may have hindered the water solution diffusion into the network, therefore, enhancing the barrier effect of the material.

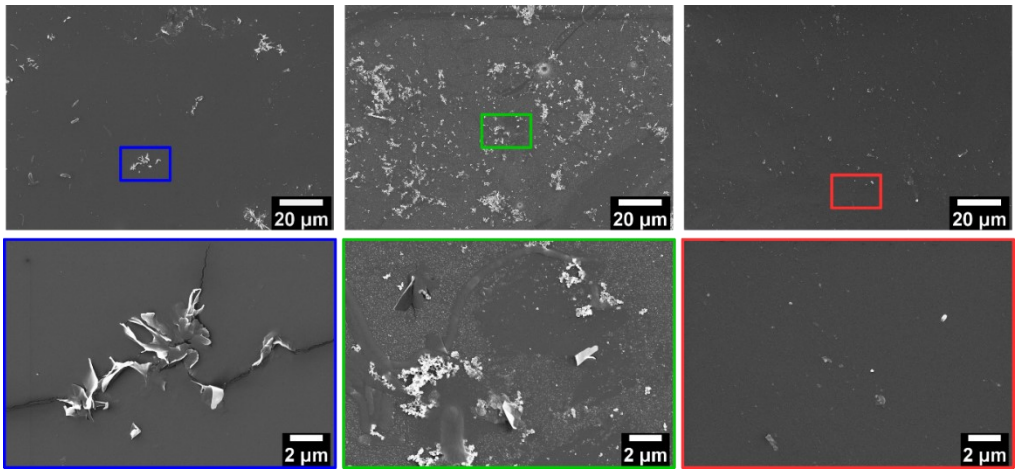

Figure 3.18: FESEM images of the biobased coatings after the impedance measurements.

3.1.5.3 Conclusions

This section reports the successful cationic photocuring of three different vegetable oils. All the formulations reached high epoxy conversion which states their high reactivity. The final thermosets possess a wide range of thermal and thermomechanical properties combined with good thermal stability. The coatings showed similar hydrophobicity and adhesion resistance. However, their corrosion protection effectiveness was very different. Among them, the ERHO-6 showed the best performances in terms of solvent resistance, hardness and corrosion resistance. These results can be attributed to its higher Tg and crosslinking density, which can have delayed the NaCl 0.1M solution diffusion into the network, improving its barrier effect. Thus, in this section, the potential applicability of vegetable oils as anti-corrosion coatings has been presented.

3.2 Radical UV-cured coatings

Other than epoxy resins, another interesting class of biobased materials is carbohydrates which are less explored due to their generally poor mechanical properties and short shelf life. Moreover, while the availability of carbohydrates-based thermoplastic is large, the thermosetting field is quite limited. To fill this gap in this section, the possibility to obtain a UV-curable starch-based thermosetting coating is exploited.

3.2.1 UV-cured biodegradable methacrylated starch based-coatings

This section is based on the original research article titled " *UV-Cured Biodegradable Methacrylated Starch-Based Coatings*". The paper was published in Coatings in 2021. https://doi.org/10.3390/coatings11020127.

In this section the possibility to obtain a photocurable starch-based thermosets coating is evaluated. Methacrylated starch, synthesized as reported in second chapter, was solubilized in water with the photoinitiator. Subsequently, the coatings were cast on the substrate and, after the water evaporation, UV-cured. The mechanical and surface properties of the obtained coatings were fully characterized. Moreover, the biodegradability of those coatings was investigated using the α-amylase enzyme. In particular, the degradation was evaluated by comparing the cured with the uncured MS and was monitored by following the amount of glucose and maltose released by the degradation of the materials in the natant medium.

3.2.1.1 Experimental section

Gel content (G%)

The gel content of the UV-cured films was determined by weighting the sample before and after 24h of extraction with water at 60°C according to the standard test method ASTM D2765-84. Using the 3.1 formula reported in the previous section.

Differential scanning calorimetric analysis (DSC)

Differential scanning calorimetric analyses were carried out on a Mettler Toledo DSC instrument at a heating rate of 10°C/min using a nitrogen atmosphere. Samples (10–12 mg) were sealed in a 100 µl aluminium pan with pierced lids.

Tensile Test

Tensile tests were performed on dry rectangular specimens (1x10cm^2) with 600 µm thickness using MTS QTest^{TM} /10 Elite controller using TestWorks® 4 software. The traction force was applied along the length of the samples at a constant cross-head displacement rate of 2mm/min. The Young's modulus (E) was calculated from the slope of the initial linear portion of the stress-strain curve. The ultimate tensile strength (UTS) and elongation at break were calculated as the maximum stress value in the stress-strain curve. Five samples for each film were tested and the value obtained averaged.

Pencil hardness

The pencil hardness test was performed using pencils of different grades starting from the 6H and continuing down the scale testing with softer and softer pencils according to ASTM D 3363-74. The pencils were maintained at 45° and pushed for at least 6 mm with uniform pressure and speed onto the coating surface. The

hardness of the coating was taken as that of the hardest pencil, which caused a cut less than 3mm long out of the 6 mm test push on the surface of the coating.

Adhesion measurement

The coating adhesion measurement was analysed according to the ASTM D3359-B. The surface of each coating was scratched both vertically and horizontally with a blade holding 6 teeth, separated from each other by a 2 mm distance. A strip of adhesive tape was then applied and subsequently pulled away at a 180° angle. The percentage of squares where the coating is still intact is reported.

Solvent rub resistance test

The coating chemical resistance was evaluated by methyl ethyl ketone double rub test according to the ASTM D5402. Double rubs were performed until the substrate was exposed or for a maximum of 200.

Enzymatic degradation

The enzymatic degradation test was carried out by using α-amylase from *bacillus licheniformis*. Pre-weighted samples were incubated in phosphate buffer saline (PBS) solution containing 0.6 mg/mL of the enzyme at 37°C for 2 weeks. At different time points (2,5,7, 14 days), supernatants were collected. The enzymatic degradation of MS and MSC was quantified by measuring the amount of maltose and glucose using The Maltose and Glucose Assay kit provided by Sigma Aldrich. Briefly, 50 µl of supernatants were mixed with 50µl of master reaction mix containing a glucose probe, which quantifies the amount of glucose generating a colorimetric product (570 nm). To measure the amount of maltose, an additional 50 µl of supernatants were mixed with 50 µl of master reaction mix containing a glucose probe and a-D-Glucosidase enzyme able to degrade maltose in two glucose units. The absorbance at 570 nm was detected using a multimode plate reader (SYNERGY, BioTeK). Tests were performed in triplicate. To monitor the α-amylase activity over time, a control solution containing only the enzyme in PBS was prepared and stored ad 37°C.

3.2.1.2 Materials and Methods

Materials

Methacrylated starch (MS) was synthesized as previously reported in second chapter. Bis(acyl)phosphane oxi lithium phenyl-2,4,6trimethylbenzoylphosphinate (LAP) used as photoinitiator was purchased from Sigma Aldrich (Milan, Italy).

Casting and Photocuring of Methacrylated Starch Coating

Initially, the MS was solubilized in water (10 wt%) with 1wt% with respect to the starch weight of LAP. Subsequently, the solution was cast on a glass substrate and left to dry in the air. Then, the casted films (MSU) (100 µm) were irradiated with a

UV-DYMAX lamp (125 mW/cm^2) in an inert atmosphere (Fig.3.19). The obtained methacrylated crosslinked films (MSC) were fully transparent and tack-free.

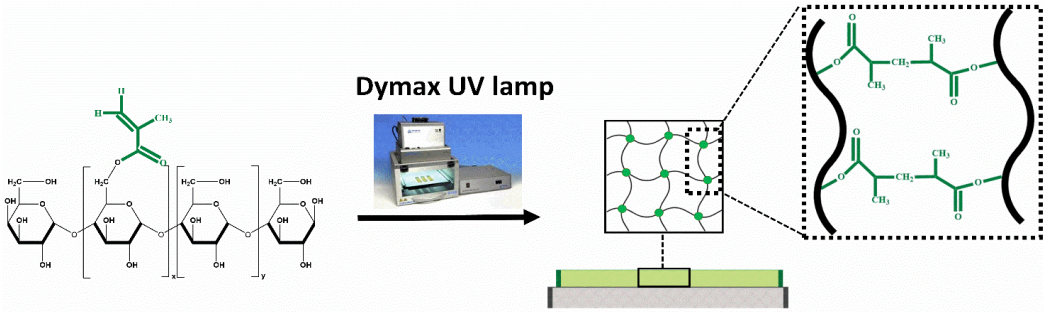

Figure 3.19: Schematic representation of the photocrosslinking reaction.

3.2.1.3 Results and discussion

Methacrylated starch-water solution containing the PhI was cast on glass and irradiated under the DYMAX lamp. Since from the FTIR analysis it was impossible to estimate the double bond conversion due to the adsorbed water peak (see second chapter), the efficiency of the photocrosslinking reaction was determined by evaluating the insoluble G% fraction at different irradiation times. As shown from Fig.3.20,a, increasing the irradiation time leads to higher G%, thus confirming the crosslinking reaction. The G% after 10 min of irradiation was already at 78% and reached the G% equilibrium (85%) after 15 min. The G% value is comparable with the one reported in the literature for starch-based films crosslinked with sodium benzoate (85%) [142]. It is important to stress that previous work had used DMSO as extracting agent for measuring the gel fraction, however since this solvent is challenging to eliminate and requires several passages; in this investigation, it was used hot water in which the MS was initially soluble.

The thermal and mechanical properties of the cast (MSU) and crosslinked (MSC) films were investigated using DSC and tensile tests. The results are summarized in Tab.3.11. As can be noticed, the UV-curing reaction leads to an enhancement of the Tg of the MSC concerning the MSU, probably ascribing to the hindering effect of the crosslinked network on chain mobility. The Tg obtained are consistent with the one reported in the literature for other crosslinked starch [143].

Fig.3.20,b reports the stress-strain tensile curve of the MSU and MSC. It can be clearly seen that crosslinking reaction leads to an enhancement of the mechanical properties. The Young's modulus (E) and the ultimate tensile strength (UTS) of MSC enhanced by 420% with respect to MSU while the elongation at break remains almost unaffected. The achieved tensile properties are similar to those obtained by gellan/gelatine composites films [30] and higher than those obtained from cassava and wheat starch [142,144].

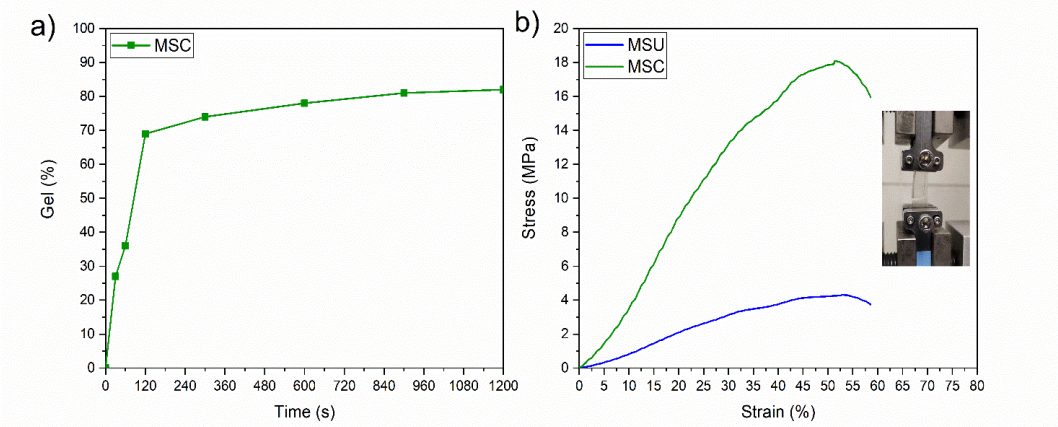

Figure 3.20: a) evaluating the insoluble gel fraction at different irradiation times; b) Stress-strain tensile curves of MSU and MSC.

Table 3.11: Thermal and tensile properties of the MSU and MSC films.

	Tg [°C]	**Young's modulus [MPa]**	**Elongation at break [%]**	**Ultimate tensile strength [MPa]**
MSU	112	9.35±0.9	49±12	4.3±1.2
MSC	121	39.29±5.7	48±15	18.1±2.9

The surface properties of the obtained MSC films were subsequently characterized. Fig.3.21,a reports a picture of MSC fully transparent film. The MSC film shows high pensile hardness (7H), which can be attributed to the presence of rigid glucose structure in the starch chains and to the crosslinking reaction [145]. The high pencil hardness value is consistent with the values reported in the literature for biobased coatings [146,147].

The MSC adhesion on the glass substrate was evaluated by a scratch test. The result is reported in Tab.3.12. MSC showed excellent surface adhesion, which can be attributed to the high amount of hydroxyl groups present in the starch chains able to form hydrogen bonds with the glass substrate [140].

The chemical resistance of the MSC was investigated with the MEK analysis, which is a solvent rub resistance test and gives a qualitative correlation between the resistance of the coating to MEK solvent and the degree of curing. This test is commonly used in industries where crosslinking cannot be investigated by conventional laboratory instruments, like FTIR. The MSC shows high MEK resistance suggesting a high cured network. This result agrees with the G% outcome and with the Tg enhancement registered by the DSC measurement.

Subsequently, the surface tension of the MSC films was evaluated. As seen in Fig.3.21,b the surface was found to be hydrophobic (85° with water) as a result of the crosslinking reaction. The overall surface energy (γ), calculated with the OWRK method was 29.8 mN/m which is a low value. A low γ value indicates a surface with poor wettability, which may give the coating enhanced antifouling properties [148].

Table 3.12: Surface properties of the MSC film.

	Pencil hardness	**Adhesion [%]**	**MEK resistance**	**Water contact angle [°]**	**Hexadecane contact angle [°]**	**γ [mN/m]**
MSC	7H	99	>200	85±5	24.8±4	29.8

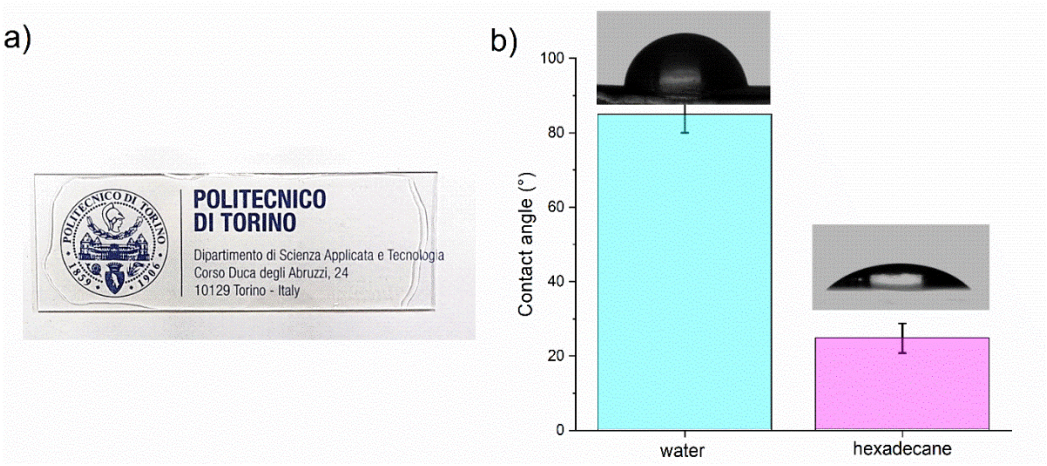

Figure 3.21: a) picture of the fully transparent MSC film coated on a glass substrate; b) Contact angle measurements with water and hexadecane.

Finally, an enzymatic degradation test was performed on MSU and MSC to evaluate their possible biodegradability. It is important to stress that the term biodegradability is defined as the "gradual breakdown of a material mediated by a specific biological activity" [149]. The enzymatic degradability of the MSU and MSC by α-amylase (from *Bacillus Licheniformis*) enzyme was investigated. *Bacillus Licheniformis* is a thermophilic Gram-positive bacterium frequently present in soil [150] and was selected to lay the foundation for further composting tests. Since the α-amylase enzyme breaks the α-1,4 glycosidic linkage of polysaccharides leading to the formation of glucose, maltose and maltotriose [151]. To evaluate the film degradation was quantified the amount of glucose and maltose in the supernatant at different time points. Noticeably, already after 4 days, the film started to fragment. Fig.3.22 reports the results of this investigation. As can be observed, the maltose and glucose amount of MSU and MSC were quite similar, except for the maltose value after 7 days of incubation (*$p<0.05$). Therefore, it can

be concluded that the crosslinking reaction does not affect significantly the degradation kinetics. Additionally, it can be observed that the maltose amount decreases with the times while the glucose one shows an enhancing trend with significant differences (*p>0.05) among different time steps. This can be probably explained considering that the enzyme is ultimately able to degrade maltose to glucose. The degradation experiment was concluded for 14 days which correspond to the time at which no solid films remained.

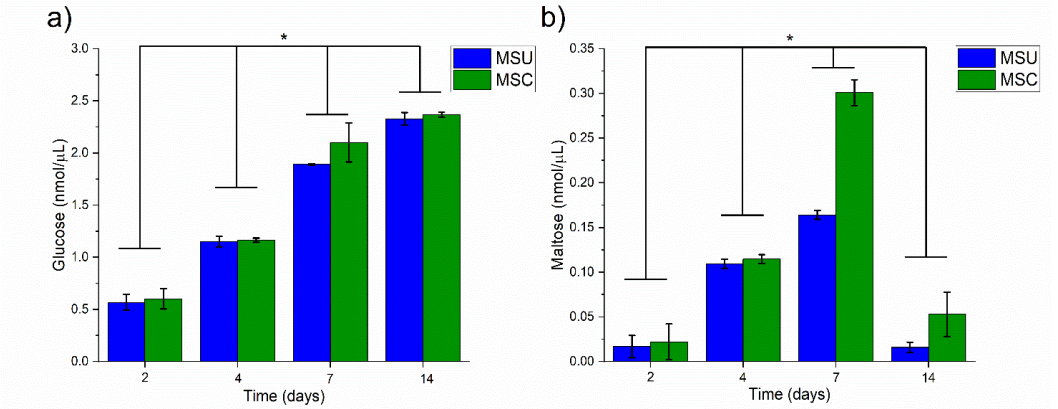

Figure 3.22: a) glucose and b) maltose amount present in the supernatant of MSU and MSC at different time intervals.

3.2.1.4 Conclusions

In this section, the possibility to obtain UV-cured starch-based film has been presented. The curing was monitored with G% investigation. After only 10 minutes, the crosslinking efficiency was above 78%. The success of the crosslinking reaction was further confirmed by the Tg enhancement (up to 10°C) and by the 420% increase of E and UTS of the MSC with respect to the uncrosslinked film (MSU). Moreover, the obtained coatings show high pencil hardness of 7H, excellent adhesion (99%) and solvent resistance (>200). Finally, the biodegradation using α-amylase (from Bacillus licheniformis) of the MSU and MSC films were evaluated. No significant differences were noticed by comparing the glucose and maltose formation upon enzymatic degradation of the MSU and MSC. Therefore, it can be concluded that the photocuring reaction does not negatively influence the degradability of the film. These promising results suggest the possibility to use polysaccharides-based thermosets as biodegradable coatings.

Fourth Chapter

4 Biobased UV-curable composites

Nowadays, the substitution of petroleum-based materials represents a great challenge also in the field of composites. The first attempts to develop greener composites was made using biobased fillers like vegetal fibers deriving from hemp, jute, and kenaf embedded in fossil-fuel-based resins [152–154]. One of the main advantages of adding biobased fibers is their high specific strength, which is comparable with glass fibers [155]. Furthermore, green fillers are generally low-cost and easy to process [156].

Even if some progress has been made to reduce greenhouse gas emissions, there still remains a need to develop biobased matrixes to manufacture fully biobased composites.

This chapter reports a study of two different biobased composites obtained using two different curing strategies. Section 4.2 presents 3D-printable soybean oil composites (ASO) with macadamia nutshell powder (MAC) as reinforcement. Section 4.3 exploits the feasibility of using the radical-induced cationic frontal polymerization (RICFP) to obtain green composites using vanillin derivatives, and both cellulose and hemp flax fibres as reinforcement is evaluated.

4.1 Experimental Section

Fourier Transform Infrared Spectroscopy (FTIR)

The FTIR spectra of ASO and ASO composites were recorded by Nicolet iS 50 Spectrometer FTIR spectrometer (Perkin Elmer, Norwalk, CT, USA) in transmission mode. For each sample, 16 scans were recorded with 4 cm^{-1} resolutions. Data were processed using the software Omnic from Thermo Fisher Scientific.

In section 4.2, it was calculated the double bond conversion by following the decrease of the double peaks centred at 1636-1618 cm^{-1}. The double peak at 1740-1727 cm^{-1} representing the C=O bond stretching vibration of the triglycerides was utilized as internal standard since it is not affected by the reaction. The calculation was done according to Eq. 4.1.

$$\text{Conversion}\ (\%) = \left(1 - \frac{\frac{A_{C=C,post}}{A_{C=C,pre}}}{\frac{A_{ref,post}}{A_{ref,pre}}}\right) * 100 \qquad (4.1)$$

Where $A_{C=C,pre}$ and $A_{C=C,post}$ represents the area of the double bond peak before and after the photopolymerization reaction, respectively and $A_{ref,pre}$ and $A_{ref,post}$ represent are the area of the reference peak before and after the photopolymerization reaction.

While in section 4.3, it was calculated the epoxy conversion by following the decrease of the peak centred at 910 cm^{-1}. To quantify this variation, the peak at 1511 cm^{-1} representing the C=C bond stretching vibration of the aromatic ring was taken as internal standards, since it is not affected by the reaction. The calculation was done following Eq. 4.2.

$$Conversion(\%) = \left(1 - \frac{\frac{A_{epoxy\_post}}{A_{epoxy\_pre}}}{\frac{A_{ref\_post}}{A_{ref\_pre}}}\right) * 100 \quad (4.2)$$

Where A_{epoxy_pre} and $A_{epoxy\text{-}post}$ are the area of the epoxy peak before and after the frontal polymerization respectively. While $A_{ref\text{-}pre}$ and $A_{ref\text{-}post}$ are the area of the reference signal before and after the fontal polymerization respectively.

Photorheology

The photorheology tests were performed with an Anton PAAR Modular Compact Rheometer (Physica MCR 302, Graz, Austria) using a parallel plate configuration (ϕ= 15 mm) with a quartz bottom glass. The gap value was set as 300 μm. All experiments were carried out at T = 25°C. Oscillatory rheometer operating in time and stress sweep modes was used to monitor the viscoelastic properties associated with the crosslinking kinetics. The time sweep experiment was performed in the linear viscoelastic region (LVR) at a constant strain amplitude (λ) of 0.5% and a constant angular frequency (ω) of 6 rad/s to monitor the crosslinking reaction by following the evolution of elastic storage modulus G' with time. After 30 s, the UV Hamamatsu LC8 lamp (Hamamatsu City, Japan) with a light intensity of 28 mW/cm^1 was turned on. The samples were irradiated from the bottom.

Radical induced cationic frontal polymerization (RICFP) evaluation

The RICFP front was evaluated by using a silicone mold for the polymerization of the composites (10 mm x 50 mm, thickness 3 mm), an optic fiber UV-light irradiation for the reaction initiation (Hamamatsu LC8 lamp, 100 mW/cm^2), and a thermo-camera for the evaluation of the front characteristics (FLIR E5, with a thermal sensibility of 0.1 °C and an IR resolution of 10,800 pixels).

Optical microscopy

The surfaces of the 3D-printed ASO composites were monitored with an Olympus BX53 M optical microscope. The ocular lenses and the objective lenses were equipped with 10× magnification.

Gel content percentage (G%)

The gel content percentage (G%) of the cured composites was determined by measuring the weight loss after 24 h extraction with chloroform. G% was calculated according to Eq. (4.3):

$$G\% = \frac{W_i}{W_0}\, x\, 100\% \qquad (4.3)$$

where Wi is the weight of the dry sample after the treatment with chloroform and W_0 is the weight of the dry sample before the treatment.

Dynamic thermal-mechanical analysis (DMTA)

DMTA analysis was performed with a Triton Technology-Tritec 2000 DMA. Samples were cooled with liquid nitrogen and measurements were run with a heating rate of 3 °C min^{-1} in tensile mode.

Differential scanning calorimetry (DSC)

DSC analyses were performed by using a Mettler Toledo DSC instrument. Approximately 10 mg of each sample were inserted in 100 µl aluminium pans with pierced lids in an inert atmosphere (N_2, 50 ml min^{-1}). The thermal behaviour of the samples was investigated by using two repeated heating-cooling cycles. The applied heating rate was 10 °C min^{-1}.

The temperature program sets for the ASO composites (Section 4.2) was: first ramp from -60 °C to 150 °C, followed by a cooling cycle from 150 °C to -60 °C. After an isotherm at -60 for 10 min, a second heating cycle was performed from -60 to 150°C. Glass transition temperature (Tg) was determined from the second heating curve.

The temperature program sets for the DGEVA and CE composites (Section 4.3) was: first ramp from 25 °C to 250 °C, followed by a cooling cycle from 250 °C to 25 °C. After an isotherm at 25 for 10 min, a second heating cycle was performed from 25 to 250°C.

Tensile Testing

Tensile tests were performed on rectangular specimens (w x l x t =10 x 50 x 2 mm) according to ASTM D1708-18 [157] using MTS QTestTM/10 Elite controller (MTS Systems Corporation, Edan Prairie, Minnesota, USA) using TestWorks® 4 software (Edan Prairie, Minnesota, USA). The tensile force was applied parallel to the samples axis at a constant cross-head displacement rate of 2 mm/min. The strain was measured as the ratio between cross-head displacement and the initial distance between the grips. The tress was calculated as the ratio between the force and the cross-section area. The Young's modulus (E) of each sample was calculated from the slope of the initial linear portion of the stress-strain curve. The toughness of the materials was calculated by calculating the area underneath the stress-strain curves. Three samples for each material composition were tested.

Field Emission Scanning Electron Microscopy (FESEM)

The morphological characterization of the ASO composites was performed by using a FESEM Zeiss Supra 40 (Oberkochen, Germany). Before the analysis, the samples were covered with a 7nm thick film of Platinum.

Scanning Electron Microscopy (SEM)

The morphological characterization of the DGEVA and CE composites was performed by using SEM (JCM-6000PLUS, JEOL). The tensile-fractured samples were covered with a 5 nm thick film of platinum and observed with the microscope.

Profilometry

The surface roughness of the 3D-printed objects was measured by Taylor Hobson Intra Touch 3D profilometry. Three surfaces were scanned for each specimen. The mean routh square values were calculated using the ISO 25178 method with the help of the TelyMap Gold 7.4.8703 software.

Cell Viability

Cytotoxicity tests were performed following the ISO10933-5 for indirect tests to identify any cytotoxic events due to the release of compounds from the ASO and ASO-MAC hydrogels. Conditioned media were prepared by soaking 0.1 g of ASO and ASO-MAC samples into 1 mL of complete medium (Dulbecco's Modified Eagle's Medium, 15% fetal bovine serum, 1% penicillin-streptomycin). Two conditions were tested: samples were soaked for 24 hours (conditioned medium_24h) and for 7 days (conditioned medium_7d). Human fibroblasts (HFF-1 ATCC® cells) were cultured in a 96-plate multiwell (MW96) using a cell density of 2×10^4 cells/well. After 24 h, the cells reached confluence and the culture medium was removed from each well and substituted with conditioned medium (conditioned medium_24h or conditioned medium_7d). Control samples (CTRL) were prepared by substituting the medium with a not-conditioned fresh medium. After 24 h, the medium was substituted in each well with 100 µL of 0.1 mg/mL non-fluorescent resazurin solution in phosphate-buffered saline-PBS. Cell viability was measured as non-fluorescent resazurin is converted to fluorescent resorufin by cell metabolism and the fluorescent signal was monitored using a plate reader (Biotek) at 530 nm excitation wavelength and 590 nm emission wavelength. Experiments were performed using six samples for each condition and cell viability was calculated as a percentage value compared to CTRL.

Cell Adhesion and Proliferation

Direct assays were performed to assess the adhesion and proliferation ability of HFF-1 cells on ASO and ASO-MAC grid-shaped samples. ASO and ASO-MAC grids 3D printed as previously described, after which they were blocked at the bottom of MW48 plate to avoid floating and seeded with 2×10^4 cells/well. Briefly, a drop of 50µl containing 2×10^4 cells was placed on the top of each grid and incubated for 2 hours, after which 450 µl of fresh media were added. At different time points (1, 3, and 7 days), cell viability was measured using resazurin as previously described. To avoid an overestimation ascribed to cells adhered at the

bottom of the plate, samples were placed in a new MW48 before adding the resazurin solution. Furthermore, cell morphology was assessed through immunostaining. Firstly, cells were fixed with 4% paraformaldehyde for 30 minutes, permeabilized with 0.5% TRITON-X in PBS for 10 minutes and blocked with 1% (w/v) bovine serum albumin (BSA, Sigma-Aldrich) in PBS for 30 minutes. Then, nuclei and actin filaments were stained incubating samples in a DAPI solution (1:1000 in PBS, Thermofisher Scientific) and rhodamine-phalloidin solution (1:60 in PBS, Thermofisher Scientific) for 10 and 40 minutes, respectively.

4.2 Acrylated soybean oil and macadamia nutshell 3D printed composites

This section is based on the original research article titled " *DLP-printable fully biobased soybean oil composites*". This article was submitted in Polymer journal 17/11/2021.

This section presents the possibility to obtain customized complex-shaped fully biobased composited via vat polymerization (Fig.4.1). The selected matrix was acrylated soybean oil while the reinforcing agent was a lignocellulose waste powder derived from the macadamia nut industry.

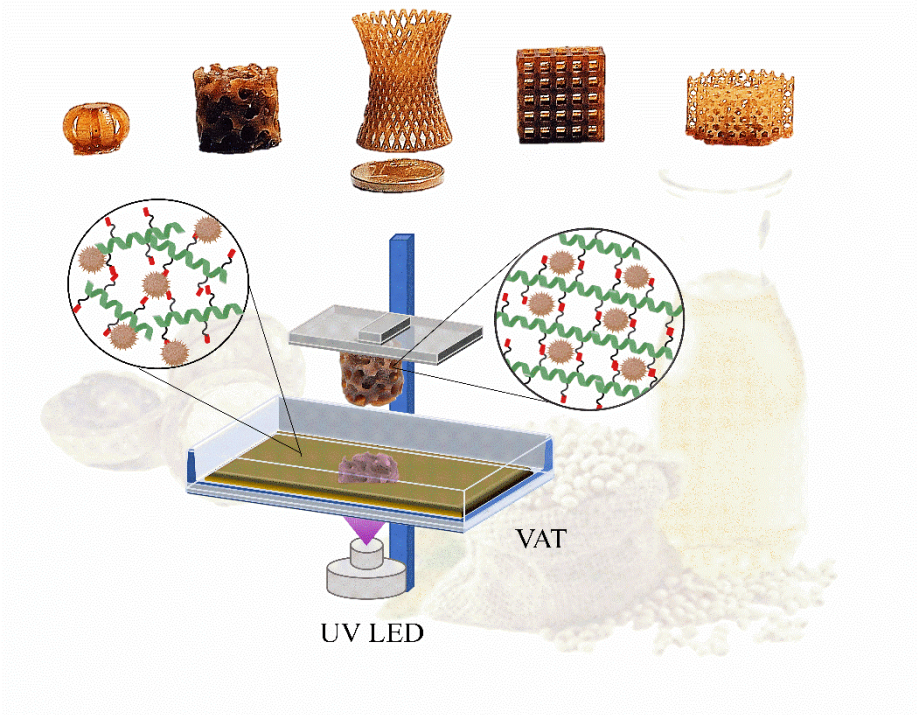

Figure 4.1: Schematic representation of DLP-printable soybean oil composites.

4.2.1 Materials and methods

Materials

Acrylated soybean oil (ASO), dimethyl sulfoxide (DMSO) (ACS reagent P99.9%), ethanol absolute, and bis-(2,4,6-trimethylbenzoyl) phenylphosphine oxide (BAPO) were purchased by Sigma Aldrich (Milano, Italy). The macadamia nutshell (MAC) was obtained from the 814 variety of macadamia and subsequently ground (the average particle dimensions was 140 μm as evaluated by FESEM images) [158].

Biobased composites formulations

The ASO photocurable formulations were prepared by mixing different amounts of MAC into the ASO liquid resin. After stirring for 5 min the BAPO photoinitiator was added into the formulation (Tab.4.1).

Table 4.1: ASO photocurable formulations.

Formulations	ASO [%wt]	MAC [%wt]	BAPO [phr]
ASO	100	0	1
ASO-MAC1	99	1	1
ASO-MAC5	95	5	1
ASO-MAC10	90	10	1

Digital light processing 3D printing

Different ASO composites were 3D-printed *via* DLP printer ASIGA (MAX X with light emission of 385 nm and nominal XY-pixel resolution of 27 μm). The UV light intensity was set to 32 mW/cm^2 while the layer thickness was set and 50 μm. The exposure time/layer was adjusted for each formulation according to the photorheology results. The obtained printed objects were post-cured using a medium-pressure mercury lamp provided by Robot Factory (2 min, 12 mW/cm^2).

4.2.2 Results and discussion

Different ASO-MAC composites were obtained *via* radical photopolymerization reaction. The UV-crosslinking reaction was evaluated by FTIR spectroscopy following the decrease of the ASO double bond peaks at 1626 and 1618 cm^{-1}, as described in the experimental section. Fig.4.2,a reports the FTIR spectra of the ASO formulation before and after irradiation. As can be observed, the C=C peaks noticeably decrease confirming the success of the reaction. A preliminary investigation of the reaction kinetics was conducted by evaluating the Conversion(%) of the formulations at different irradiation times, as reported in Fig. 4.2,b. Fig. 4.2,b shows that all the ASO formulations exhibited fast reactivity,

reaching a Conversion(%) higher than 85% (Tab.4.2) in less than 30 seconds also in the presence of the biobased filler.

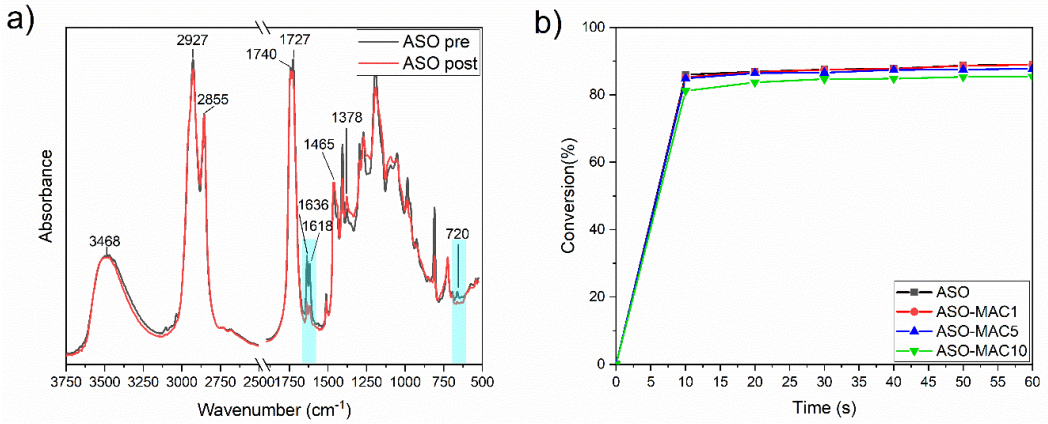

Figure 4.2: a) ASO FTIR spectra before and after the UV irradiation; b) Conversion(%) of ASO formulations at different irradiation times.

The reaction kinetics of the ASO formulations were further investigated using a real-time photorheology test, from which it was possible to monitor the changes in the viscoelastic properties of the materials during the reaction. Fig. 4.3 reports the storage modulus G' values at different time steps. The sharp enhancement of the G' when the lamp is switched on indicates a high reactivity of the ASO formulations, which is in good agreement with the previously obtained FTIR results.

Interestingly, the pristine formulation, the ASO-MAC1 and ASO-MAC5 reached a G' plateau after 30 seconds which is in the same order of magnitude as the one achieved by poly(lactide-*co*-glycolide) (PLGA) diacrylates formulations used to create bioscaffolds in previous work [159]. In contrast, the G' of ASO-MAC10 reached a plateau after 90 seconds. The ASO-MAC10 formulation required a higher irradiation time to complete the reaction with respect to the other formulations. Nonetheless, it is possible to observe a slight decrease in the reaction kinetics of ASO-MAC5 with respect to ASO-MAC1 by looking at the initial slope of the G' curve ($\Delta G'/\Delta t$) reported in Tab.4.2. In fact, with the enhancement of MAC content there was a $\Delta G'/\Delta t$ decrease from 56 to 28 kPa*s^{-1}, suggesting a slowdown effect provoked by the presence of MAC. This effect can be attributed to the UV-shielding effect of MAC, which has a brown color causing a reduction of the formulation's transparency and therefore hindering light penetration. The slight reactivity reduction of the formulations with the increased addition of MAC is in good agreement with the FTIR Conversion(%) outcome and with the slight reduction of the insoluble fraction (G%) of the composites (Tab.4.2).

Additionally, it can also be observed that the G' plateau value increased as the MAC content increased from 4 MPa of ASO alone to 11 MPa of ASO-MAC10 composites, suggesting a reinforcing effect of the MAC particles towards the ASO matrix.

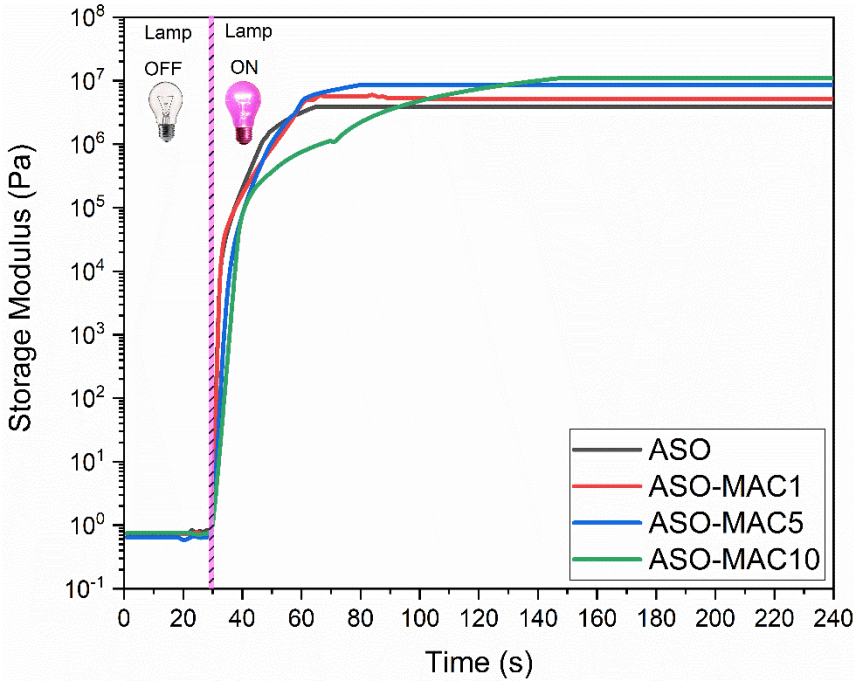

Figure 4.3: Photorheology curves of the ASO formulations.

Table 4.2: Crosslinking parameters of ASO formulations.

	ASO	ASO-MAC1	ASO-MAC5	ASO-MAC10
FTIR Conversion [%]	89	89	87	85
ΔG'/Δt [kPa s^{-1}]	56	44	29	28
G [%]	90	87	86	85

Subsequently, the applicability of the ASO-MAC formulations as biobased ink for DLP printing was evaluated. The printing parameters were adjusted according to the photorheology results. The exposure time was varied from 1 to 2.5 seconds based on the MAC amount present in the formulation. Different complex CAD models were developed to evaluate the printability of the formulations. As can be noted from Fig.4.4, high-resolution composites were successfully 3D-printed for all the ASO formulations. Noticeably, the brown colour of the MAC enabled the printability of complex geometries without the addition of dyes, typically required to avoid over-polymerization defects caused by the light diffusion into the vat. Fig.4.4,a shows an example of ASO and ASO composites 3D-printed objects reproduced from the same CAD model. Fig.4.4,b reports a complex lattice structure obtained using the ASO-MAC10 formulation. The high CAD fidelity of the printed composites was assessed by optical microscopy as presented in Fig.4.4,c.

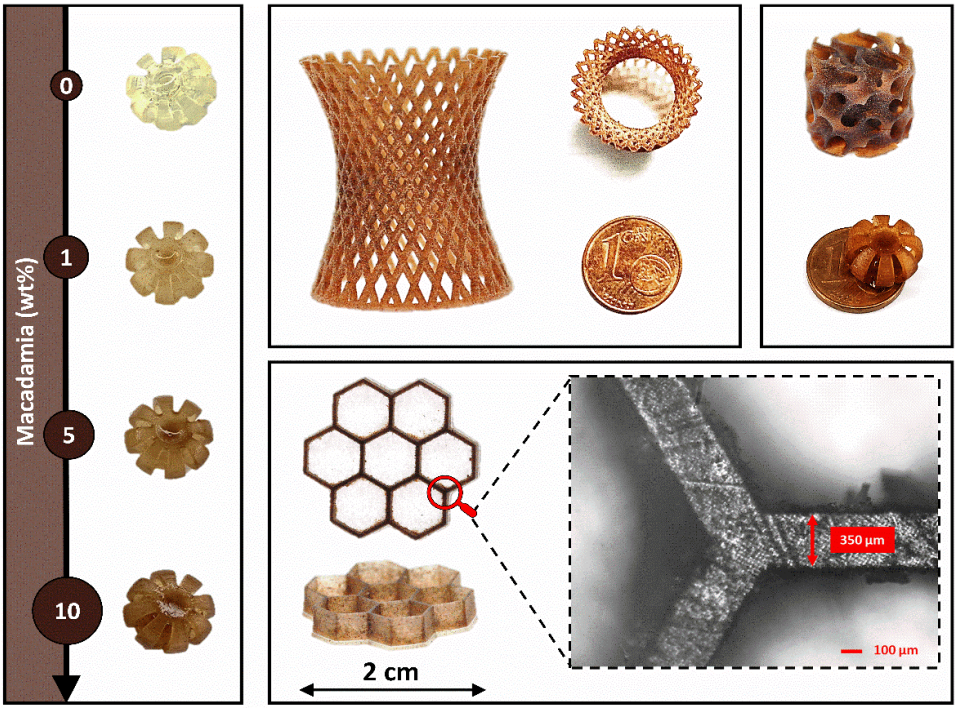

Figure 4.4: a) ASO, ASO-MAC1, ASO-MAC5and ASO-MAC10 3D-printed composites; b) complex lattice-shaped structure from ASO-MAC10; c) evaluation of the printed objects fidelity with respect to the CAD model by means of optical microscopy.

The thermomechanical properties of the 3D-printed composites were investigated by means of DMTA analysis. Fig.4.5,a shows the storage modulus and the Tanδ curve of the ASO composites at different temperatures. As can be observed from Tab.4.4, the Tg of the composites (measured as the peak of Tanδ) increased as the MAC content increased, suggesting reinforcement of the ASO matrix by the MAC powder. This trend was confirmed by the DSC analysis and is in good agreement with the photorheology outcomes. Moreover, from the graph reported in Fig.4.3,a further considerations can be made. In fact, the enhancement of the MAC content also led to a decrease and to a broadening of the Tanδ peak which may indicate the enhancement of network heterogeneities such as relaxation time and chain mobility distribution [106,160]. Additionally, the E' modulus in the rubbery plateau also increased with the addition of MAC which may be attributed to a reduction of the ASO chain mobility ascribing to the MAC particles acting as a physical barrier [161].

A tensile test was subsequently carried out to further investigate the mechanical properties of the composites. Tab.4.3 reports the ultimate tensile strength (UTS), Young's modulus (*E*), and toughness (K_{IC}) values of the ASO composites, while Fig.4.3,b shows their averaged stress-strain curves. Both *E* and UTS noticeably increase as the MAC content increased reaching 100 MPa and 3.8 MPa, respectively, in the ASO-MAC10 composite. The E values of the ASO composites range from 15 to 100 MPa which matches the typical values of the bone tissues and

are comparable with other materials used for bone tissue engineering like 3D-printed polycaprolactone (20MPa) and polylactic acid/multi-wall carbon nanotubes/polyethylene glycol composites (26 MPa) [162,163]. This outcome may imply the potential applicability of the 3D-printed ASO composites as bone scaffolds in the field of tissue engineering.

Furthermore, embedding MAC powder into the ASO matrix led to an enhancement of the toughness of the composites (Tab.4.3) which can be defined as the ability of the material to adsorb energy before fracture while the elongation at break (ε_b) remains almost constant or even slightly higher with respect to the unfilled matrix. The elongation at break can be influenced by many complex phenomena including filler shape and/or distribution, filler/matrix interaction and the viscoelastic properties of the matrix. Therefore, the observed ε_b behaviour can be attributed to a good filler/matrix interaction.

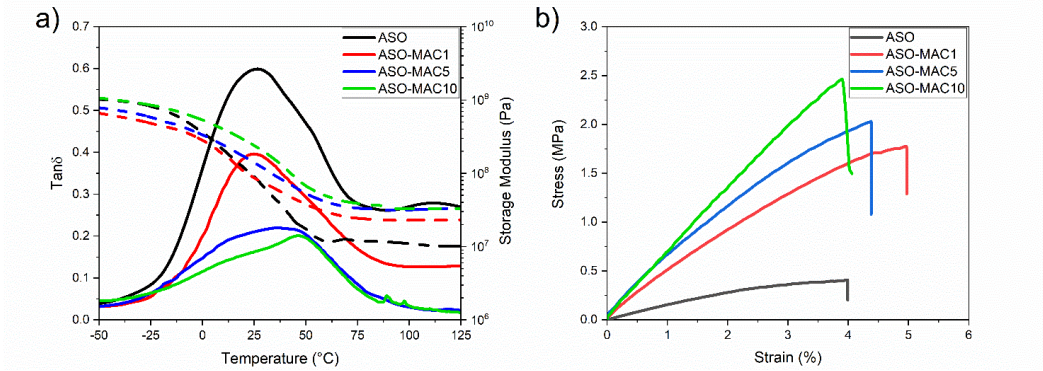

Figure 4.5: a) DMTA analysis and b) Tensile test of ASO and ASO composites.

Table 4.3: Thermal and mechanical properties of ASO and ASO composites.

Sample	Tg_DMTA [°C]	E_rubbery [MPa]	Tg_DSC [°C]	*E* [MPa]	UTS [MPa]	ε_b [%]	K_{IC} [MJ/m³]
ASO	25	12.0	10	15.0±0.2	0.45±0.07	4.0±0.3	1.28±0.1
ASO-MAC1	27	24.1	15	54.3±0.2	1.80±0.15	5.5±0.4	6.57±1.2
ASO-MAC5	38	31.3	22	68.5±0.5	1.98±0.24	4.9±1.1	6.61±1.8
ASO-MAC10	46	33.0	30	100.2±1.7	3.80±0.40	4.5±0.9	7.01±2

Field-emission scanning electron microscopy (FESEM) images were recorded on the MAC particles to analyse their average dimensions and on the tensile fractured surfaces of the composites to investigate their morphology. As can be observed from Fig.4.6, the MAC particles had an irregular shape and had an average dimension of 140 µm. Fig.4.6 b reports the ASO matrix alone, while Fig.4.6 c, d, and e show the ASO-MAC1, ASO-MAC5, and ASO-MAC10 samples. It is clear that an excellent dispersion of the MAC particles in the ASO resin was achieved in

the ASO-MAC1 composites, while in the other composites there were some agglomerates, especially in the ASO-MAC10. Moreover, all the fracture surfaces were rough indicating a high resistance to the crack propagation [163].

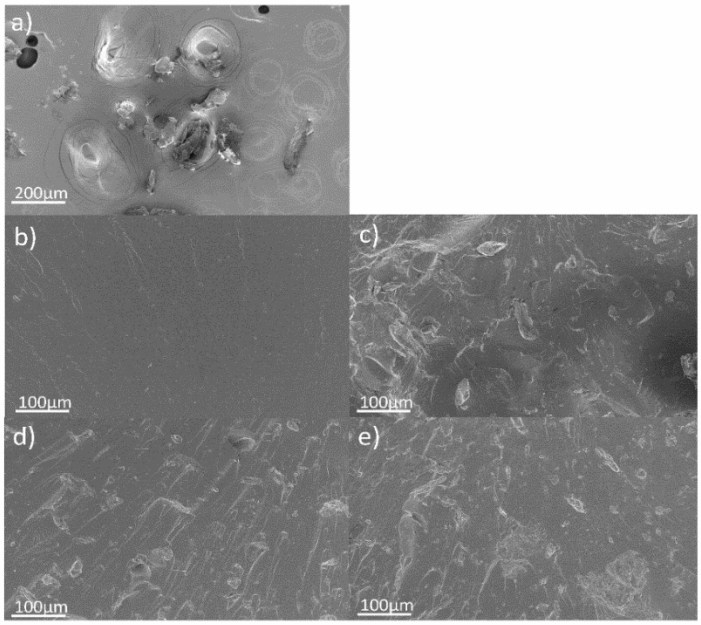

Figure 4.6: FESEM micrographs of MAC powder, ASO and ASO composites.

Subsequently, a profilometer was used to evaluate the surface topographies of ASO composites surfaces (Fig.4.7). The average root mean square (RMS) values obtained were: 3.01 µm for ASO, $Sq_{ASO\text{-}MAC1}$= 3.73 µm for ASO-MAC1, 7.03 µm for ASO-MAC5, and 10.9 µm for ASO-MAC10. The slight enhancement of the RMS with the MAC content increase is consistent with the FESEM images. Noticeably the RMS was, in all cases, lower than the one previously reported for other DLP printed objects (53.8 to 76 µm) used for dental applications [164].

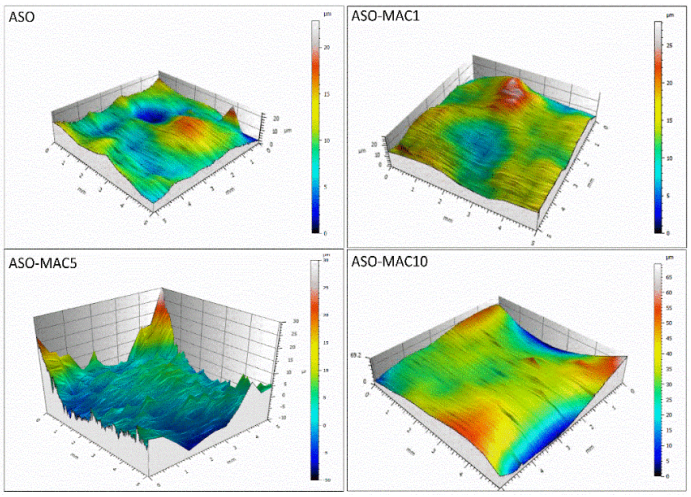

Figure 4.7: profilometry measurements of the 3D-printed objects.

Finally, indirect and direct tests were performed to evaluate the possibility to use the ASO composites as a substrate for cell adhesion and proliferation. Initially, it was performed a cell viability test, whose results are reported in Fig.4.7,A. All the ASO composites showed no cytotoxicity effect which indicates that the objects do not release toxic products like unreacted monomer, photoinitiator, or degraded pieces after one day (conditioned medium_1d) and up to 7 days (conditioned medium_7d). Subsequently, the adhesion and proliferation of HFF-1 cells onto the ASO composites 3D-printed grids were investigated (Fig.4.7,B). Even if the MAC addition does not hinder the HFF-1 adhesion and proliferation, a slight reduction of the cell numbers compared to the control was noticed. This result may be explained considering that the control has a simple 2D surface so it has an enhanced total surface area with respect to the ASO grids (filament/pore ratio 2.5) which may have increased the initial number of adhered HFF-1 cells and therefore led to a higher proliferation rate. Additionally, the capability of the ASO composites to support the cell colonization was assessed through immunostaining at 7 days (Fig.4.8). Noticeably, the HFF-1 cells adhered on the grid showed uniform, distribution with a spread morphology.

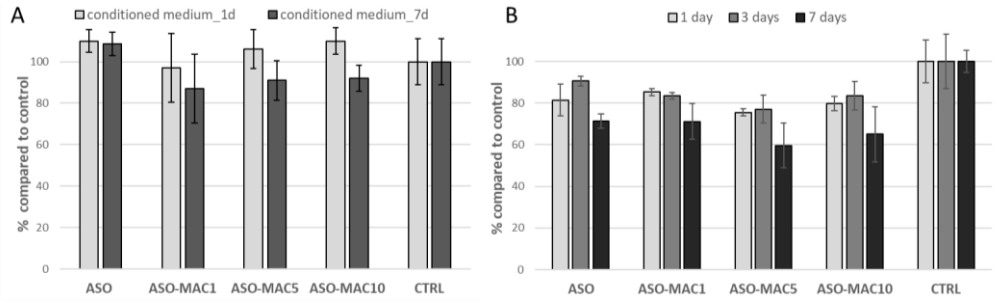

Figure 4.8: HFF-1 cell viability: A) indirect tests at two conditions: samples were soaked for 24 hours (conditioned medium_24h) and for 7 days (conditioned medium_7d) and B) proliferation assay at 1, 3 and 7 days using printed grid-shaped samples.

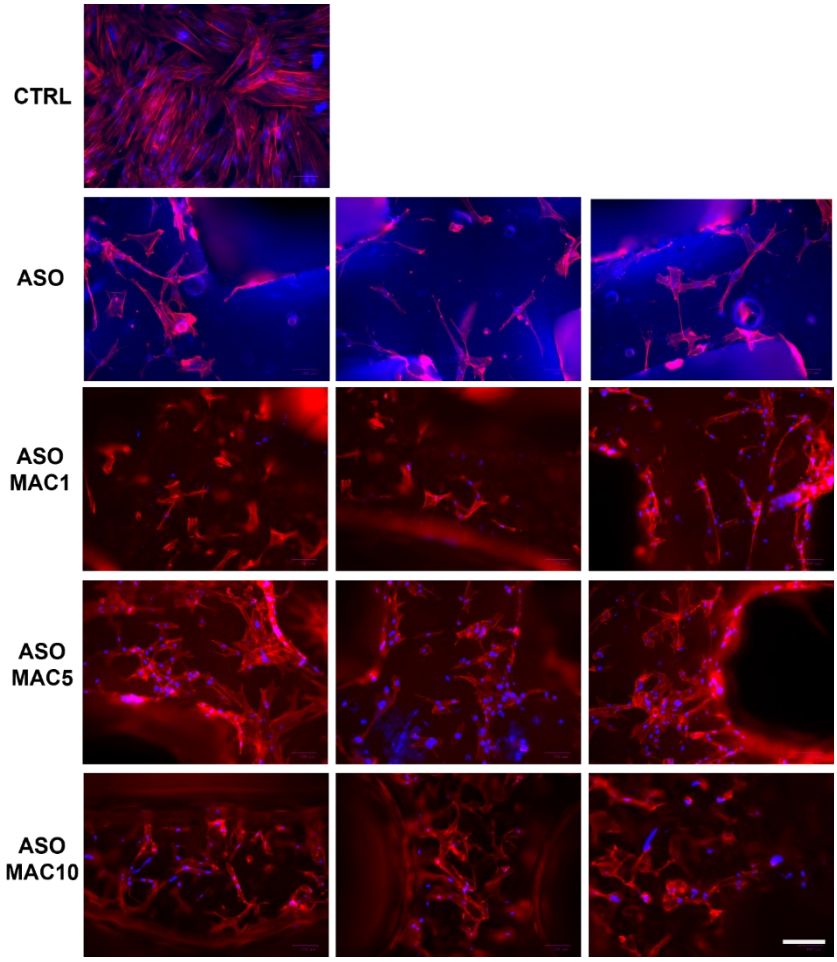

Figure 4.9: Nuclei and actin filaments staining of ASO and ASO-MAC grid-shaped samples. Polystyrene plates were used as control (CTRL). A slightly blue autofluorescence can be observed for ASO samples. Scale bar: 50 µm.

4.2.3 Conclusions

This section presents the successful 3D printing of different fully biobased composites obtained using acrylated soybean oil as a matrix and macadamia nutshell powder as a reinforcing agent. The high reactivity of the ASO-MAC formulations was confirmed with both FTIR and photorheology investigations. Even if a slight UV-shielding effect of the MAC powder was noticed, the calculated double bond conversion was always higher than 85%. The possibility to use DLP-printing technology to obtain composites possessing high geometrical complexity and fidelity with the CAD models was assessed. The high resolution achieved by the printed objects was evaluated with optical microscopy. Subsequently, the thermomechanical and thermal characterization of the composites showed that the MAC addition leads to an increase in the Tg values (from 25 to 46°C). The MAC enhancement into the matrix also enhances the stiffness of the composite (+ 660%) as shown in Young's modulus values calculated from the tensile test. The FESEM

images assessed the good dispersion of the particles into the matrix, while the profilometry characterization indicates the generally low RMS value successfully obtained with the DLP printing.

4.3 Frontal-photopolymerization of fully biobased epoxy composites

This section is based on the original research article titled " *Frontal-photopolymerization of fully biobased epoxy composites*". This article was published on Macromolecular Materials and Engineering in 2022, DOI: 10.1002/mame.202100864 [165].

In this section, the possibility to obtain fully biobased composited using a radical-induced cationic frontal photopolymerization (RICFP) is presented. Two different fabrics made of cellulose and flax were embedded into two epoxy matrices, one biobased deriving from vanillin-diglycidylether of vanillyl alcohol-DGEVA (already used in the third chapter) and the other one petroleum-based-3,4-epoxycyclohexylmethyl 3,4 epoxycyclohexanecarboxylate-CE. The final properties of the obtained composites were investigated and compared.

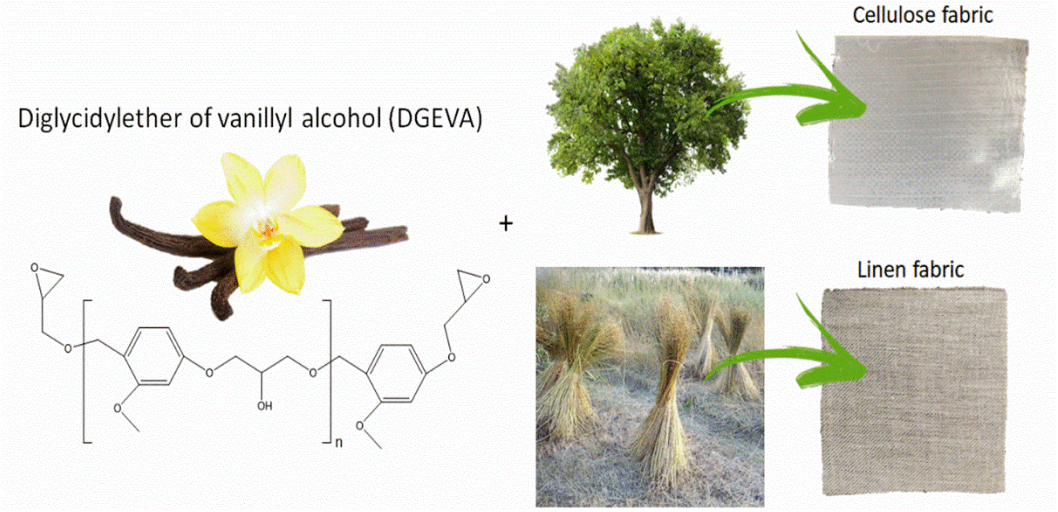

Figure 4.10: Scheme of the DGEVA composites.

4.3.1 Materials and methods

Materials

The biobased epoxy resin: diglycidylether of vanillyl alcohol (DGEVA) was synthetized and provided by Specific Polymers. The petroleum-based epoxy resin:

3,4-Epoxycyclohexylmethyl 3,4-epoxycyclohexanecarboxylate (CE), the thermal initiator: 1,1,2,2-tetraphenyl-1,2-ethanediol (TPED) were purchased from Sigma Aldrich. The cationic photoinitiator: (p-octyloxyphenyl)phenyliodonium hexafluoroantimonate (PAG) was obtained from ABCR. The fabric mats: cellulose unidirectional non-woven fibres and woven flax fibres (linen) were supplied by HP Johannesson Trading AB, Sweden. All the chemicals were used as received without further purification.

Biobased composites preparation

Different composites were prepared either using cellulose fabrics or linen fabrics as fibre-reinforcement. The formulations were prepared by mixing neat DGEVA with 1 phr (parts per hundred resin) of TPED and 1 phr of $Ph_2I^+SbF_6^-$ (PAG). To ease the TPED dissolution it was dissolved in propylene carbonate (50:50 wt%). Different composites (10x50 mm, thickness 2 mm) were prepared by impregnating one cellulose (DGEVA1CL), one linen (DGEVA1LL), two cellulose (DGEVA2CL), or two linen (DGEVA2CL) plies of fibers. The impregnation was conducted in mild vacuum conditions for 30 minutes. Subsequently, the corner of the mold was irradiated with an optical fiber UV lamp (Light-Ning Cure™ LC8, Hamamatsu) to activate the thermal front. For comparison composites made using a petroleum-based epoxy matrix: 3,4-epoxycyclohexylmethyl 3,4-epoxycyclohexanecarboxylate (CE) with the same fibers content were also prepared and UV cured under the same conditions. The composite compositions are reported in Tab.4.4.

Table 4.4: Composite compositions.

	PAG (phr)	**TPED (phr)**	**N° Cellulose layers**	**N° linen layer**
DGEVA	1	1	/	/
DGEVA1CL	1	1	1	/
DGEVA2CL	1	1	2	/
DGEVA1LL	1	1	/	1
DGEVA2LL	1	1	/	2
CE	1	1	/	/
CE1CL	1	1	1	/
CE2CL	1	1	2	/
CE1LL	1	1	/	1

4.3.2 Results and discussion

Different composites were prepared using a radical-induced cationic frontal photopolymerization technique (RICFP). The RICFP (Fig.4.11) reaction requires an initial UV-irradiation step which provokes the highly exothermic epoxy rings opening. Then, the heat released by bond dissociation activates the thermal initiator which starts the front propagation. The generated carbon-centered radicals are subsequently oxidized to carbocations by the iodonium salt [166,167]. The carbocations further induce the cationic ring-opening polymerization through the sample until the front heat is dissipated.

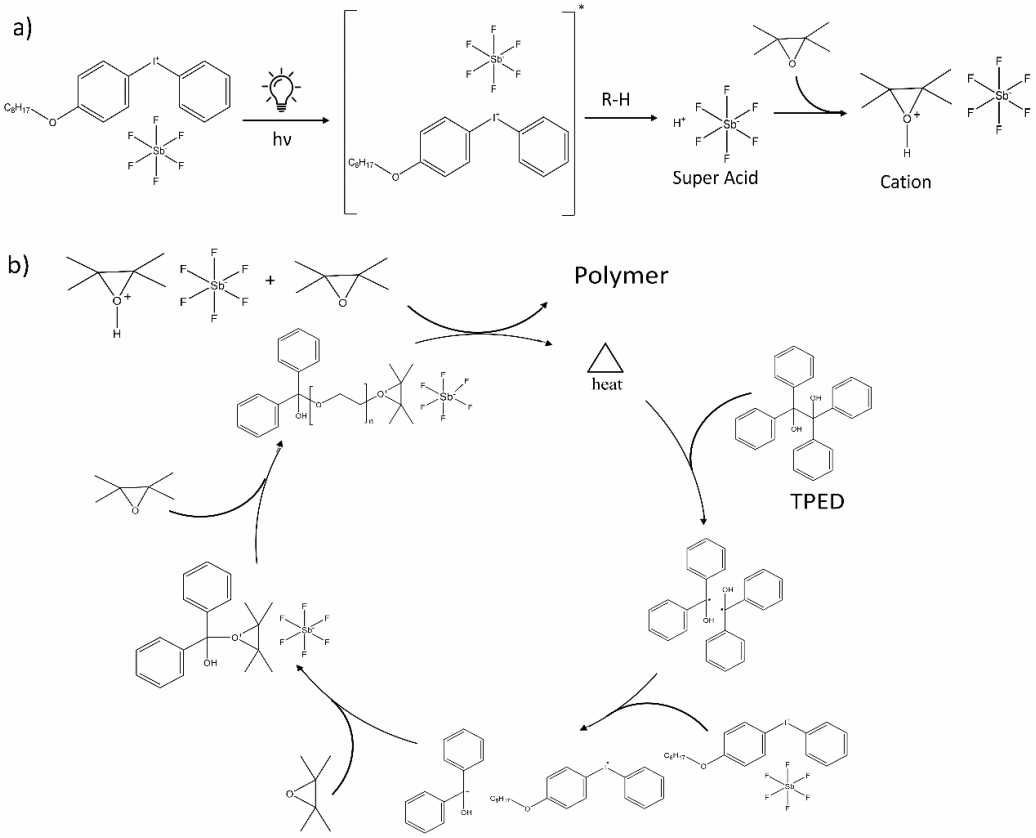

Figure 4.11: RICFP reaction scheme: a) UV-induced diphenyl iodonium salt (PAG) decomposition followed by the photoacid generation; b) exothermic epoxy ring-opening and reaction propagation with the formation of radicals from the dissociation of the C-C labile bond of TPED (thermal initiator).

Considering that the thermal front requires a constant heat generation to continue propagating, the fibers heat dissipation has to be taken into account. Initially, the optimum photoinitiator-thermal initiator ratio was optimized in the pristine DGEVA formulation to guarantee a self-sustaining heat front maximizing the epoxy-groups conversion. The optimum formulation was found to be the one

containing 1 wt% /1wt% TPED/PAG, which was further investigated with the fibers. The thermal front was monitored using a thermo-camera as described in the experimental section. Fig.4.12,a reports a scheme of the thermal front propagation process, while Fig.4.12,b reports the real UV-initiated thermal front of the DGEVA formulation recorded with the thermo-camera.

Tab.4.5 reports the front parameters of DGEVA and DGEVA composites such as the font starting time (t_0), the front velocity (V_f), and the maximum front temperature (T_{max}). The V_f was extrapolated from the temperature profile registered at three different points: 10, 20, and 50 mm of the samples recording the time in which the T_{max} is reached (see Fig.412,c; and Fig.4.13) [168]. As can be observed, the t_s and the V_f are higher in the composites compared to the pristine DGEVA resin, possibly attributed to a good thermal conductivity of the fibers as previously observed in the literature [169]. Noticeably, the V_f reached by the DGEVA formulation is higher than the previously obtained RICFP of petroleum-based resins [170–172]. The registered thermal front for all the DGEVA showed a constant propagation rate with a linear behavior (Fig.4.12,d) which highly supports the hypothesis of an effective front propagation mechanism. The high T_{max} (285°C) value reached by DGEVA and DGEVA composites is consistent with the previously reported T_{max} for the RICFP of DGEBA with TPED and PAG (283°C) [171].

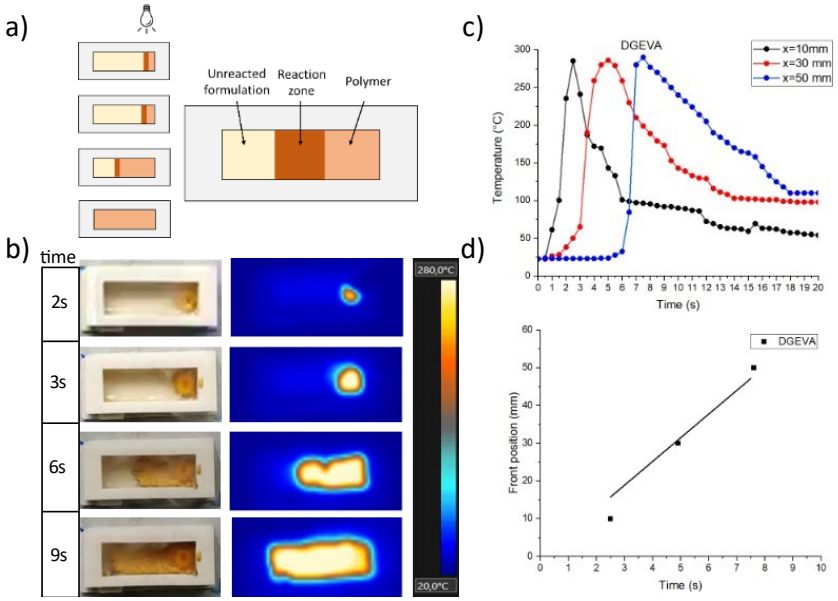

Figure 4.12: a) schematic presentation of the UV-initiated thermal front; b) thermo camera frame sequence of the propagating DGEVA thermal front; c) temperature-time evolution at three different DGEVA specimen position; d) DGEVA front position as a function of time.

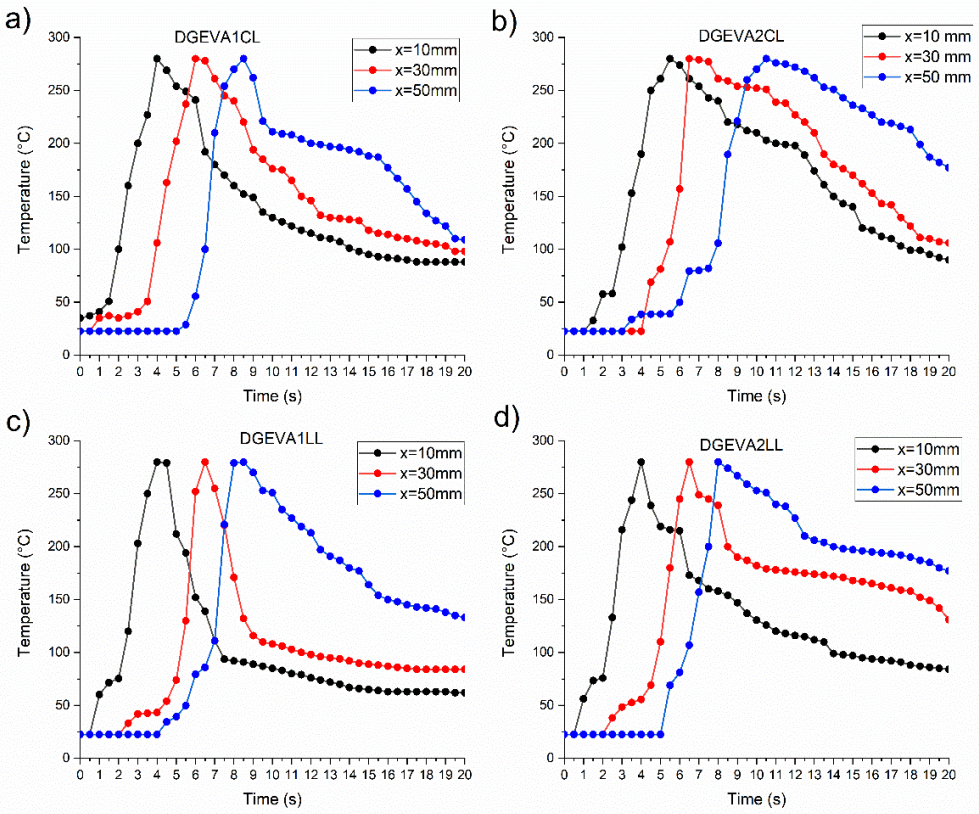

Figure 4.13: temperature–time evolution at three positions along the composites from the trigger point of a) DGEVA1CL, b) DGEVA2CL, c) DGEVA1LL and d) DGEVA2LL.

The UV-curing reaction of the DGEVA resin was followed by FTIR analysis. The spectra were recorded before and after the RICFP in transmission mode (Fig.4.14). Firstly, in the DGEVA spectrum, there can be clearly observed the typical vanillyl peaks like the peaks at 1230 and 1260 cm^{-1} corresponding to the -CH_2 twisting and wagging vibrations, respectively. The peaks from 1261 to 1160 cm^{-1} are identified as the vanillyl fingerprint region. The band at 1600 cm^{-1} is attributed to the C-O vibration. The peaks ranging from 1453 to 1592 cm^{-1} correspond to the C=C vibration of the substituted benzene [173]. The peaks at 2930 and 2970 cm^{-1} are assigned to the sp^3 C-H bond vibration of the aliphatic chain [174]. The low peaks at 3000 and 3060 cm^{-1} may be assigned to the methyl groups in proximity to epoxy rings [175].

The success of the curing reaction was assessed by the intensity reduction of the peaks at 800, 850, and 910 cm^{-1} attributed to the epoxy rings vibrations, and by the appearance of the broad peak at 3460 cm^{-1} representing the -OH groups vibration formed as a consequence of the epoxy ring-opening. The epoxy ring conversion was 82%, calculated as described in the experimental section.

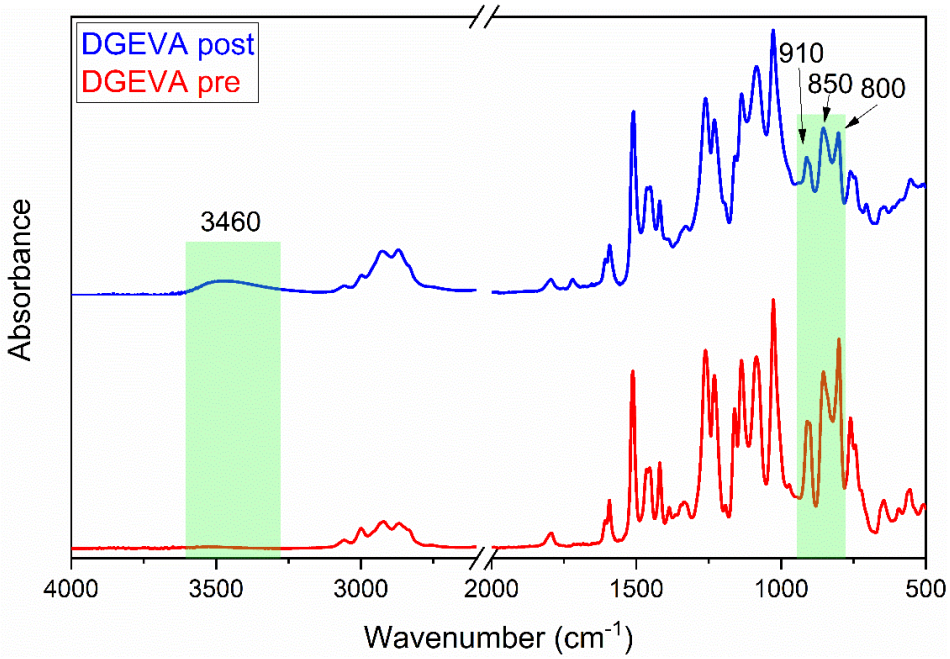

Figure 4.14: FTIR spectra of the DGEVA pre and post-cured. Film thickness 12 µm coated on a silicon substrate.

To further characterize the curing of the DGEVA a DSC analysis was performed as described in the experimental section. In fact, the epoxy group conversion can be estimated by calculating the area under the exothermic peak. In Fig.4.15,a is reported the DGEVA formulation thermograms. In the first cycle, an exothermic peak at 120°C with a heat release of 129.44 J/g can be clearly observed. The heat release value can be attributed to the total epoxy group conversion since it entirely disappears in the second run. Interestingly, in the second run, a glass transition temperature at around 75°C can be noticed. In fig.4.25,b, a RICFP cured DGEVA sample is reported, in which a low exothermic response (3.18 J/g) is observed in the first run. This exothermic signal may represent residual thermal polymerization and it also disappears in the second scan. From the recorded exothermicity values it can be estimated the value of the RICFP epoxy group conversion of the DGEVA pristine formulation, which was found to be 90%.

The higher epoxy group conversion calculated from the DSC analysis with respect to the FTIR one can be explained taking into consideration the non-negligible heat losses to the surrounding occurring during the RICFP of the sample in the FTIR analysis.

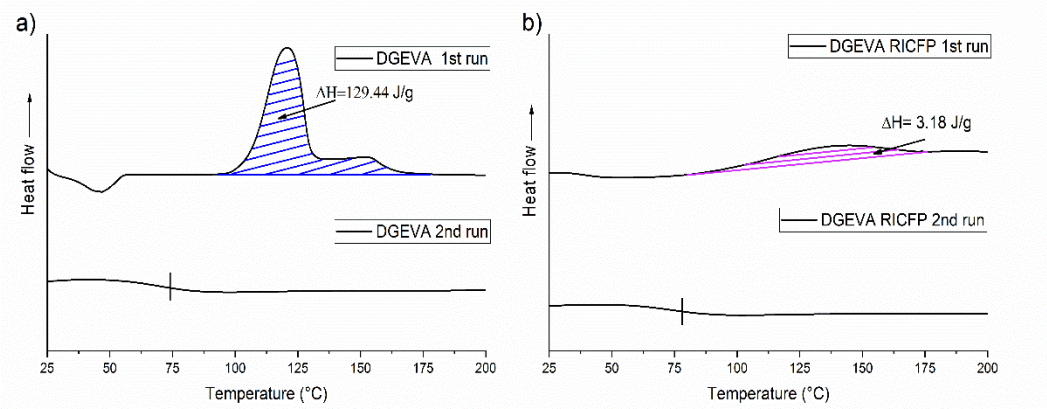

Figure 4.15: DSC thermograms of a) DGEVA resin first and second run; b) DGEVA after RICFP curing first and second run.

Nevertheless, a quantitative epoxy group conversion cannot be calculated from the FTIR analysis since the thickness of the sample was too high for the transmission of the FTIR signal and the ATR-FTIR mode allows evaluating only qualitatively the degree of curing.

Thus, an estimation of the curing efficiency was conducted by evaluating the gel or insoluble fraction (G%) of the composites. The obtained values are reported in Tab.4.5. As can be observed, the G% values are always higher than 95% implying an efficient reaction with a small amount of released unreacted product.

Table 4.5: Thermal-front parameters.

	t_0 [s]	V_f [cm min^{-1}]	T_{max} [°C]	G%
DGEVA	2	48±2	280±4	96±2
DGEVA1CL	4	69±4	285±2	96±1
DGEVA2CL	5	66±2	278±1	98±1
DGEVA1LL	4	67±4	285±2	95±2
DGEVA2LL	4	62±3	277±3	96±2

Subsequently, the thermo-mechanical and mechanical properties of the DGEVA composites were investigated with DMTA and tensile tests. Additionally, all those measurements were also conducted on CE composites cured with the same RICFP system using the same fibers to have a direct comparison with a commercially available fossil-fuel-based resin.

The viscoelastic properties of the composites like storage modulus (E'), the loss modulus (E''), and the damping factor (Tanδ= E''/E') were obtained from the DMTA analysis. The averaged E' and the Tanδ plots are shown in Fig.4.16. It can be observed that the E' value increase as the number of fabrics increases suggesting

an effective reinforcing effect of the matrix. This result was expected since the E' of the composites increases when the polymer segments are hindered by fiber-fiber and fiber-matrix interactions. Moreover, the Tanδ peak of the DGEVA composites lowers its intensity with the addition of the fiber fabrics, further confirming the reinforcement effect of the fiber which hinders the polymer chain mobility and consequently leads to a decrease of the Tanδ [176]. Noticeably, this lowering Tanδ trend is not observed on the CE composites which can be ascribed to a decrease of the interfacial bonding between the filler and the matrix and to the formation of a less homogeneous network [177]. It is also interesting to notice that the addition of flax fibers leads to a more evident enhancement of Tg in the DGEVA composites (91 – 130°C) with respect to the CE ones (93 – 107°C). This result may be attributed to a low interfacial interaction between the CE matrix and the flax fibers.

As can be observed in Fig.4.16, the E' values always decrease as the temperature increases due to a matrix softening effect. Noticeably, the E' values of the DGEVA composites are generally high (54 – 130 MPa) and very similar to the CE.

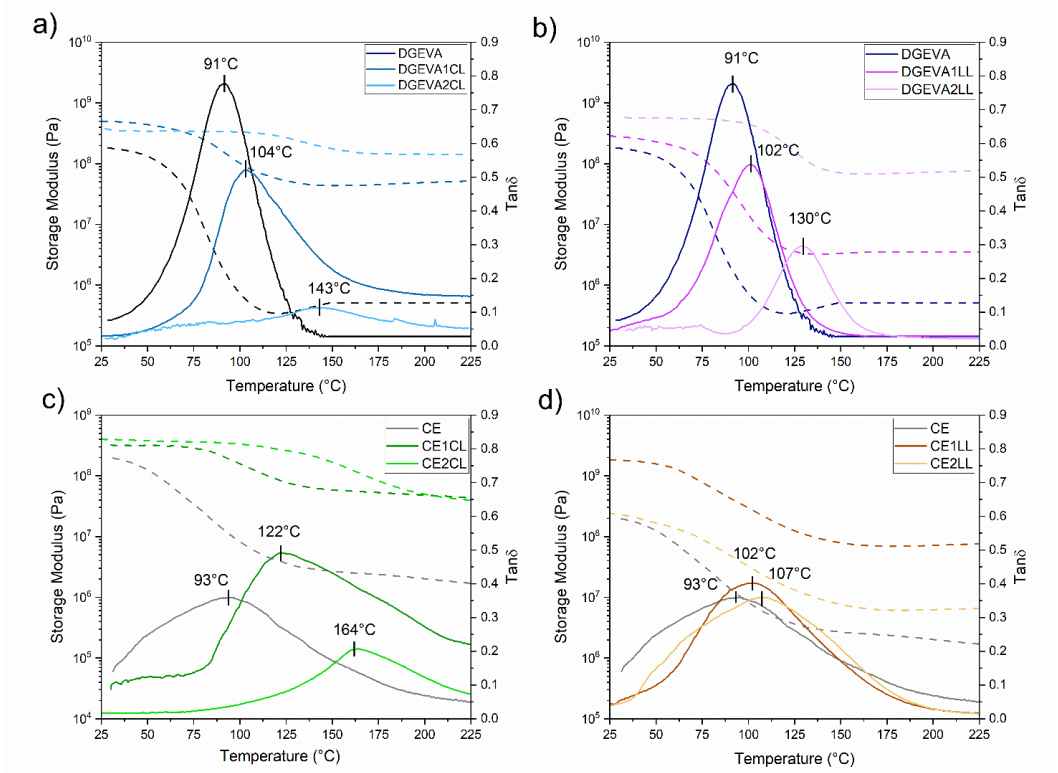

Figure 4.16: Tanδ and storage modulus curves of epoxy–cellulose (right) and epoxy-linen (left) composites. a) DGEVA-cellulose, b) DGEVA-linen, c) CE-cellulose and d) CE-linen.

Fig4.17 shows the averaged tensile stress-strain curves of the DGEVA and CE composites. The elongation at break slightly increases with the addition of the

fibers, except for the DGEVA1CL, suggesting a small ductility increase with respect to the brittle resins. However, all the specimens possess a generally low elongation at break values which nevertheless, can be expected for fiber-reinforced composites. Generally, the addition of the fiber enhances the tensile strength (σ_{max}) further confirming a strong fibers/matrix interaction which is in good agreement with the mechanical reinforcement observed in the DMTA outcomes. The DGEVA composites made of unidirectional non-woven cellulose (Fig.4.17,a) proved to be more brittle and harder than the one made of woven flax (Fig.4.17,c) since they showed lower elongation at break and higher tensile strength. This behavior can be attributed to the interlocking effect of fill and warp yarn [178]. Interestingly, even if the DGEVA crosslinked network possesses lower rigidity than the CE one, the DGEVA composites achieved comparable or even enhanced tensile strength compared to the CE ones. The Young's modulus (*E*) values are reported in Fig.4.18. The DGEVA composites reached 1.2 and 0.8 GPa as a maximum *E* value when the cellulose and linen fibres were added, respectively. Those values are comparable to the ones obtained from the CE composites (0.8 and 0.6 GPa, respectively). The σ_{max} reached for the DGEVA cellulose composites ranged from 10 to 18 MPa while the DGEVA linen composites from 6 to 12 MPa (Fig.4.18,a). Instead, the σ_{max} obtained for the petroleum-based CE composites ranged from 11 to 17 MPa when cellulose was added and 6 to 7 MPa when the reinforcement was linen. Moreover, the obtained E and σ_{max} values of the DGEVA composites are comparable with the values reported in the literature for other natural-fibres reinforced epoxy composite as summarized in Tab.4.6. Noteworthy, the thermo-curing time used to obtain the other natural fibres composites is markedly higher than the one here reported.

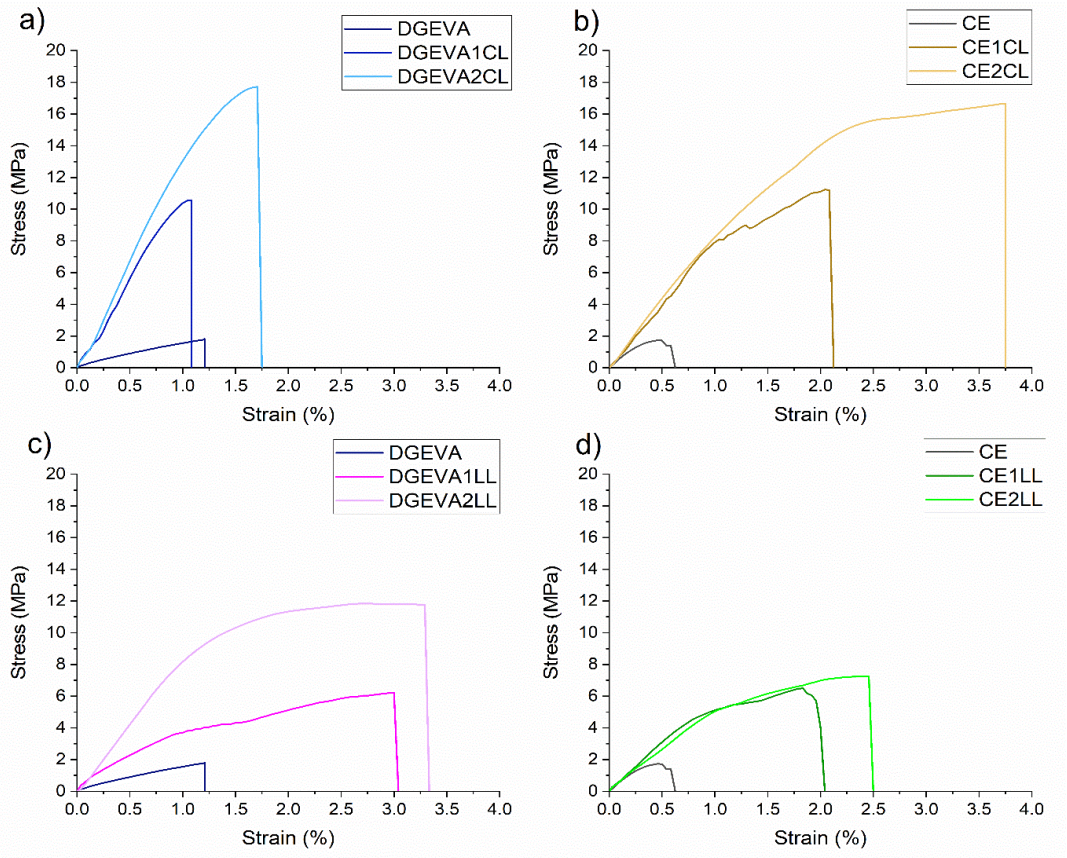

Figure 4.17: Tensile stress-strain curves of a,c) DGEVA composites; b,d) CE composite.

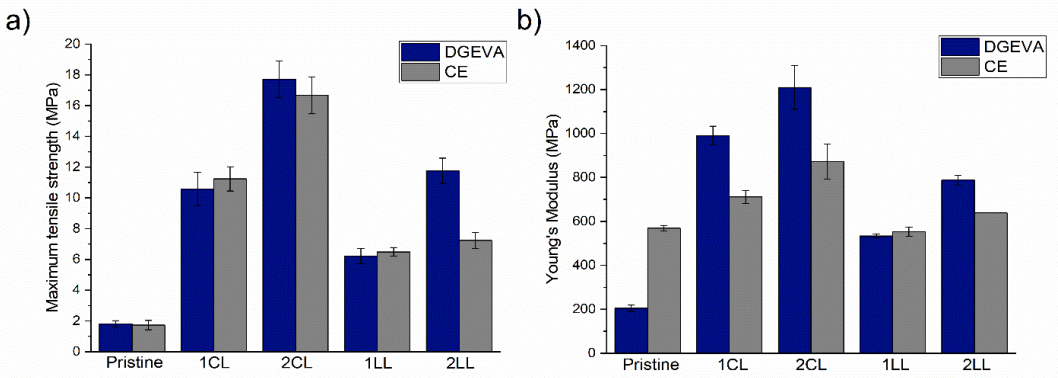

Figure 4.18: Comparison of a) maximum tensile strength and b) Young's modulus between DGEVA and CE composites.

Table 4.6: Mechanical tensile properties of natural fibre reinforced composites reported in literature compared with the properties achieved by the composites prepared with RICFP in the present work.

Type of curing	**Fibre reinforcement**	**Curing time**	**Tensile strength [MPa]**	**Young's Modulus [MPa]**	**Reference**
Thermal	Kenaf/glass	/	40-110	6000-1200	[79]
Thermal	Kenaf	/	25-40	3000-5000	[80]
Thermal	Jute/hemp/flax	24 h	30-60	1000-1700	[81]
Thermal	Aloevera and sisal	24 h	19-27	/	[82]
Thermal	Jute/pineapple and glass	24 h	40-70	500-900	[79]
Thermal	Coir/glass fibre	24	30-60	/	[83]
Thermal	Pineapple/flax	/	22-35	/	[84]
RICFP	Cellulose/linen	1 min	6-18	600-1200	*Present work
Type of curing	Fibre reinforcement	Curing time	Tensile strength [MPa]	Young's Modulus [MPa]	Reference

Finally, scanning electron microscopy (SEM) images were recorded to evaluate the morphologies of the fractured composites and the fibre-matrix adhesion (Fig.4.19). As can be observed from the images, the DGEVA resin diffused inside the yarn which suggests a good wettability of both fibre fabrics with the biobased resin. The good wettability results in a strong adhesion between the fibres and matrix, which is in good agreement with the data obtained from the DMTA and tensile tests. Moreover, by looking at the fractured surfaces it can be observed that the failure mechanism involved is a mixture of fibre debonding and fibre pull-out which are key damaging mechanisms in fibre composites (Fig.4.19, b,c). In fact, in the tensile test the failure process of a polymer-fibre composites usually took place when a small crack forms into the matrix transferring the load by the matrix to the fibre *via* shear forces. These shear forces gradually increase inducing the failure of the matrix-fibre interface. This process led to the generation of a cylindrical crack at the interface which propagates as the load increases. This failure mechanism is named bedonding. However, since in the curing process the epoxy resin can have slightly shrieked on the fibre, some load can be still transferred between the matrix and the fibre by interfacial forces, inducing a friction between them. This friction induces a non-uniform stress through the debonded fibre which can generate an enhanced stress in a different part of the fibre with respect to the matrix-crack plane. As a consequence, the fibre breaks at some distance from the broken interface [185]. This failure process, called pull-out, can be detected in the broken surface samples

of both DGEVA1CL (Fig.4.19,b) and DGEVA1L (Fig.4.19,c) which show protruding fibres.

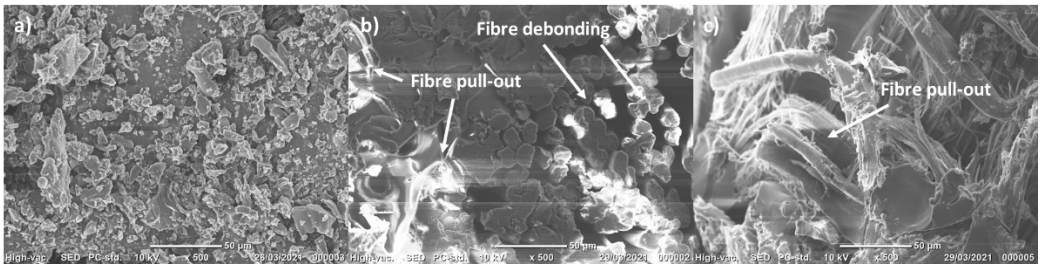

Figure 4.19: SEM images of the fracture surfaces of a) pristine DGEVA, b) DGEVA1CL and c) DGEVA1L.

4.3.3 Conclusions

In this section, the possibility to use the RICFP to obtain fully biobased composites using a biobased epoxy resin and natural fibres has been presented. The fibres selected for this purpose were either made of cellulose or flax. The RICFP curing possesses high front velocity and successfully led to high epoxy group conversion (>96%). The obtained composites reached Tg in the range of 104 to 143°C in the case of cellulose fabrics addition and 102 to 130°C for flax fabrics. Moreover, the properties of the biobased composites were compared with the corresponding petroleum-based ones. Noteworthy, the tensile mechanical properties of DGEVA composites were comparable or even higher than the one obtained with CE. The Young's modulus obtained by the DGEVA composites ranged between 600 to 1200 MPa which is in the same order of magnitude as other composites reported in the literature for petroleum-based natural fibre composites. Interestingly, the overall thermal and mechanical properties increased as the fibre content increased, suggesting a god fibre-matrix interaction, and subsequently verified by SEM images. Therefore, this section presented the feasibility of using the fast and energy-efficient RICFP technique to obtain fully biobased composites with good thermal and mechanical properties.

General conclusions

This thesis work exploits the possibility of obtaining different biobased thermosets using various photopolymerization techniques. In this frame, numerous starting materials were selected and functionalized with meth(acrylic) or epoxy groups to make them light-processable. Their reactivity toward photopolymerization processes was investigated and their thermo-mechanical properties were carefully evaluated. It was proved that UV-light irradiation is a powerful tool that can be used for the development of biorenewable thermosets.

In the first experimental work, maize starch was successfully modified with methacrylic anhydride to produce photocrosslincable hydrogels, using either UV-lamp or DLP 3D printing. The methacrylation reaction was confirmed by means of ^{1}H-NMR, ^{13}C-NMR, and FTIR spectroscopy. By means of the ^{1}H-NMR technique, it was possible to estimate the DOS, which was around 0.08. Three different MS water solutions were prepared and irradiated in the presence of LAP, which was used as the photoinitiator. The high reactivity of the formulations was assessed by means of a photorheology test. Subsequently, from the results of the compression test, it emerged that the obtained hydrogels reached compressive Young's modulus values that cover different body tissues, and interestingly, the formulation containing 10 wt% of MS was found to match the values of muscle tissue. The cytocompatibility test on the hydrogels, which was performed using human fibroblast cells, highlighted that none of the samples released toxic products after the photocrosslinking reaction. Finally, the 3D printability of the MS10 solution was assessed, and the results suggested that these hydrogels could be applied in the tissue engineering field.

In the second experimental work, MS was mixed with acrylated cyclodextrin (ACy) in a DMSO/water solution to obtain photocrosslikable OHGs. The photorheology, mechanical and morphological characterizations highlighted that the addition of ACy resulted in an enhancement of the reaction kinetics, and of the cross-link density, which in turn led to the formation of stiffer structures with less porosity. Moreover, the ACy influenced the sorption capabilities of the OHGs to a great extent. Indeed, the addition of ACy decreased the maximum swelling capability of the OHG, but, inversely, the MB adsorption capacity increased. This result can be ascribed to the combination of the ability of ACy to form inclusion complexes with MB and to the chelating properties of the -OH groups of MS. The main OHG sorption mechanism resulted to be chemisorption, as indicated by the good fitting of the sorption kinetics data with the pseudo-second-order kinetic model. Additionally, the DLP printability of the OHGs was demonstrated, thereby possibly opening a new frontier for water remediation.

The third experimental work focused on the cationic UV-curing of three biobased monomers: epoxidized castor oil (ECO), phloroglucinol trisepoxy (PHTE) and the diglycidylether of vanillyl alcohol (DGEVA). These monomers possess a high reactivity and, in all cases, it was possible to obtain tack-free films. The ECO epoxy group conversion resulted to be the best among the monomers, since its aliphatic structure allowed a high mobility of the polymeric growing chain to be obtained. The presence of flexible aliphatic chains is also the reason for the low glass transition temperature achieved by the final ECO thermosets. The DGEVA monomer has a rigid aromatic structure, which leads to thermosets with a high Tg, however this rigid structure causes early vitrification during photopolymerization, thus reducing the final epoxy group conversion. Notwithstanding such an aromatic structure, the PHTE films showed a lower Tg than DGEVA, which can be ascribed by the presence of a higher number of hydroxyl groups in its chain. In fact, these -OH groups may have started a chain transfer reaction which led to the formation of flexible ether chains. Therefore, this study successfully proved the applicability of epoxy bio-renewable monomers in the cationic photopolymerization field.

In the fourth experimental work, three different epoxidized cardanol-based monomers were selected with different numbers of epoxy groups. The monomers possess a good reactivity toward the cationic photocrosslinking process, as can be seen from the final epoxy group conversion (64 – 72%) obtained from the FTIR analysis. The Tgs of the thermosets can be modulated by changing the initial aromatic monomer structure or the epoxy ring content in the resin. This part of the work demonstrated the possibility of applying cardanols for the production of UV-curable coatings.

The possibility of tuning the final thermomechanical properties of the films, by simply selecting the initial monomer structure and the number of epoxy groups present in the moiety, was further investigated in the fifth part of the work. In this investigation, 12 different epoxidized vegetable oils (EVOs), with different numbers of oxirane rings, were cationically phothocrosslinked. All the EVOs showed a high reactivity and their final epoxy group conversion was always above 90%. It was then demonstrated, through both DMTA and DSC analyses, that it was possible to modulate the Tg of the thermosets over a wide range of temperature, from -19 to 50°C, by choosing EVOs with different epoxy contents.

The sixth work investigated the applicability of UV-curable EVO formulations to create anti-corrosion coatings. In this work, three different coatings, obtained from rosehip seed and from grapeseed, were analyzed. Although the coatings show similar water contact angles and adhesion, they have quite different corrosion protection effectiveness. The EVO with the highest epoxy index leads to the formation of the coating with the best performances, that is, a high degree of hardness, solvent resistance, and corrosion resistance. These results can be explained by considering the high crosslinking density and Tg reached by this thermoset. Furthermore, the combination of such properties may have delayed the

water and salt diffusion through the coating, thus enhancing the barrier effect of the coatings against the corrosive medium. Therefore, this study offered a complete understating of the potentiality of using vegetable oils to produce coatings with anti-corrosion properties.

In the seventh experimental contribution, the possibility of obtaining UV-curable fully transparent films from MS was illustrated. The efficiency of the photocrosslinking process was evaluated by analyzing the insoluble fraction (G%), at different irradiation times. The G% plateau, which corresponds to the formation of 79% of the gel insoluble fraction, was reached after 10 minutes. The success of the UV-curing reaction was also proved by the results of the mechanical characterization, in which the MS starch film crosslinked (MSC) was compared with the just cast but not crosslinked film (MSU).

The MSC film showed an enhancement of the Tg of 10°C, and a 420% increase in Young's modulus and in the ultimate tensile strength values with respect to the MSU. Moreover, the MSC coating has a high pencil hardness (7H), excellent adhesion (99%), and good solvent MEK resistance (>200). Subsequently, the biodegradability of MSU and MSC was assessed, by means of enzymatic degradation, using α-amylase enzymes derived from *Bacillus licheniformis*. The outcomes show that the degradation kinetics was not influenced by the crosslinking reaction.

Therefore, we demonstrated the possibility of using MS as a starting material to achieve new types of photocurable coatings with encouraging levels of biodegradability.

The eighth work involved the DLP-printing of biobased composites made of acrylated soybean oil (ASO) and macadamia nutshell powder (MAC). The high reactivity of the ASO-MAC1 formulation was confirmed by means of both FTIR spectroscopy and photorheology, although a slight UV-shielding effect was observed as the result of the addition of a larger amount of MAC. Nevertheless, high curing kinetics and double bond conversion were always achieved for all the formulations. Complex 3D-printed objects with high resolution and CAD fidelity were successfully obtained using a DLP printer. The enhancement of the MAC content in the composites allowed a higher Tg and stiffer thermosets to be reached with a maximum +660% increase of Young's modulus. The formation of homogeneous composites was assessed from FESEM images. The promising results of cell adhesion and proliferation tests with human fibroblast cells conducted on all the composites would seem to point out their potential applicability in the biomedical field.

In the ninth experimental work, the RICFP technique was used for the preparation of DGEVA resin composites, reinforced with either cellulose or flax fibers. The RICFP reaction showed a fast front velocity in all the composites, which led to a striking reduction of the processing time, compared to the conventional thermo-curing process. The composites showed good thermomechanical properties

and reached up to 130 and 140°C when linen or cellulose were used, respectively. The biorenewable composites proved to have similar or even higher mechanical properties than the corresponding petroleum-based CE composites, as shown by means of the tensile test. Furthermore, the achieved mechanical properties are comparable with previously reported data obtained for other natural-fiber reinforced composites but cured using petroleum-derived epoxy resins. Interestingly, the thermal and mechanical properties of the vanillin-based composites increased as the fiber fraction content increased. This result indicates a good resin-fiber adhesion, which was also confirmed by means of SEM analysis. Thus, this work shows the possibility of applying the RICFP technique to produce high-performance composites in a fast and energy-efficient way.

To conclude, the results presented in this thesis manuscript successfully provide a full understanding of the potentiality of applying biobased monomers as innovative precursors for photopolymerization processes. Indeed, the encouraging outcomes can represent a stimulus for future investigation possibly targeting more specific industrial applications.

Appendix A

A1 List of Abbreviations

ACy = acrylated γ-cyclodextrin

AGU = Anhydrous Glucose Unit

ATR-FTIR = Attenuated Total Reflectance-Fourier Transform Infrared Spectroscopy

BAPO = phenylbis(2,4,6-trimethylbenzoyl)phosphine oxide

DLP = digital light processing

DMSO = dimethyl sulfoxide

DMTA = Dynamic thermal-mechanical analysis

DSC = Differential Scanning Calorimetry

E' = storage modulus

E'' = loss modulus

E'_R = storage modulus values in the rubbery plateau region

E_c = compressive young's modulus

ECM = extracellular matrix

EVOs = epoxidized vegetable oils

EWC = equilibrium water content

FESEM = Field Emission Scanning Electron Microscopy

FTIR = Fourier transform infrared spectroscopy

G% = Gel content

G' = storage modulus

G'_p = the value of G' in the plateau region

HFF = Human fibroblasts

HG = Hydrogels

K_{IC} = toughness

LAP = bis(acyl)phosphaneoxilithium phenyl-2,4,6-trimethylbenzoyl phosphinate

LVR = linear viscoelastic region

M^*_e = molar mass between two entanglements points

MA = Methacrylic anhydride

MB = Methylene blue

MS = methacrylated starch

NMR = Nuclear Magnetic Resonance

OHGs = Organo/hydrogels

q_e = equilibrium adsorption capacity

q_m = adsorption capacity at time t

RICFP = radical-induced cationic frontal polymerization

S = high amylose maize starch

SD_{eq}% = equilibrium swelling ratio percentage

SD% = swelling degree

Tanδ = loss factor

ε_b = elongation at break

ν_e = number of crosslinks

ξ = distance between two entanglements points

ν_c = apparent cross-linking density

A2 List of Figures

A3 List of Tables

Appendix B

B1 List of publications from the author related to this thesis work

Submitted Camilla Noè, Andrea Cosola, Chiara Tonda-Turo, Raffaella Sesana, Cristina Delprete, Annalisa Chiappone, Minna Hakkarainen, Marco Sangermano. “DLP-printable fully biobased soybean oil composites

2022 Camilla Noè, Minna Hakkarainen, Samuel Malburet, Alain Graillot, Kayode Adekunle, Mikael Skrifvars, and Marco Sangermano, " Frontal-Photopolymerization of Fully Biobased Epoxy Composites ". In Macromolecular Materials and Engineering. DOI: 10.1002/mame.202100864

2021 Camilla Noè, Andrea Cosola, Annalisa Chiappone, Minna Hakkarainen, Hansjörg Grützmacher, Marco Sangermano, " From polysaccharides to UV-curable biorenewable organo/hydrogels for methylene blue removal ". In *Polymer.* https://doi.org/10.1016/j.polymer.2021.124257

2021 Camilla Noè, Minna Hakkarainen and Marco Sangermano (2021). "Cationic UV-Curing of Epoxidized Biobased Resins". In *Polymers.* https://doi.org/10.3390/polym13010089.

2021 Camilla Noè, Leonardo Iannucci, Samuel Malburet, Alain Graillot, Marco Sangermano, and Sabrina Grassini (2021). "New UV-Curable Anticorrosion Coatings from Vegetable Oils". In *Macromolecular Materials and Engineering.* DOI: 10.1002/mame.202100029.

2021 Camilla Noè, Chiara Tonda-Turo, Irene Carmagnola, Minna Hakkarainen and Marco Sangermano (2021). "UV-Cured Biodegradable Methacrylated Starch-Based Coatings". In *Coatings*. https://doi.org/10.3390/coatings11020127.

2020 Camilla Noè, Samuel Malburet, Elodie Milani, Agathe Bouvet-Marchand, Alain Graillot and Marco Sangermano (2020). "Cationic UV-curing of epoxidized cardanol derivatives".In *Polymer International*, pag. 668-674. DOI 10.1002/pi.6031.

2020 Camilla Noè, Chiara Tonda-Turo, Annalisa Chiappone, Marco Sangermano and Minna Hakkarainen (2020). "Light Processable Starch Hydrogels". In *Polymers*. doi:10.3390/polym12061359.

2020 Samuel Malburet, Chiara Di Mauro, Camilla Noè, Alice Mija, Marco Sangermano and Alain Graillot (2020). "Sustainable access to fully biobased epoxidized vegetable oil thermoset materials prepared by thermal or UV-cationic processes". In *RSC Advances*, pag. 41954–41966. 10.1039/d0ra07682a.

2019 Camilla Noè, Samuel Malburet, Agathe Bouvet-Marchand, Alain Graillot, Cédric Loubat, Marco Sangermano (2019). "Cationic photopolymerization of bio-renewable epoxidized monomers". In *Progress in Organic Coatings*, pag. 131–138. https://doi.org/10.1016/j.porgcoat.2019.03.054.

B1 List of publications from the author unrelated to this thesis work

Submitted Diana Cafiso, Athanasia Amanda Septevani, Camilla Noè, Tara Schiller, Candido Fabrizio Pirri, Ignazio Roppolo, Annalisa Chiappone. "Tree-D" printing of cellulose-based hydrogels"

2021 Anastasiia O. Krushynska, Antonio S. Gliozzi, Alberto Fina, Dmitry Krushinsky, Daniele Battegazzore, Miguel A. Badillo-Ávila, Mónica Acuautla, Stefano Stassi, Camilla Noè, Nicola M. Pugno, and Federico Bosia (2021). "Dissipative Dynamics of Polymer Phononic Materials". In *Advanced Functional Materials.* DOI: 10.1002/adfm.202103424.

2021 Valentina Casalegno, Federico Smeacetto , Milena Salvo , Marco Sangermano , Francesco Baino , Camilla Noè, Marco Orlandi , Riccardo Piavani , Roberto Bonfanti , Monica Ferraris (2021). "Study on the joining of ceramic matrix composites to an Al alloy for advanced brake systems". In Ceramics International. https://doi.org/10.1016/j.ceramint.2021.05.062.

References

1. *Kirk-Othmer Encyclopedia of Chemical Technology*; Wiley, 2000; ISBN 9780471484943.
2. Cywar, R.M.; Rorrer, N.A.; Hoyt, C.B.; Beckham, G.T.; Chen, E.Y.X. Bio-Based Polymers with Performance-Advantaged Properties. *Nature Reviews Materials* **2021**, *0123456789*, doi:10.1038/s41578-021-00363-3.
3. Babu, R.P.; O'Connor, K.; Seeram, R. Current Progress on Bio-Based Polymers and Their Future Trends. *Progress in Biomaterials* **2013**, *2*, 8, doi:10.1186/2194-0517-2-8.
4. Global-Plastic-Production-1950-2020 Available online: https://www.statista.com/statistics/282732/global-production-of-plastics-since-1950/.
5. European-Bioplastics.Org/Market/ Available online: https://www.european-bioplastics.org/market/.
6. Sangermano, M.; Razza, N.; Crivello, J.V. Cationic UV-Curing: Technology and Applications. *Macromolecular Materials and Engineering* **2014**, *299*, 775–793, doi:10.1002/mame.201300349.
7. Sangermano, M.; Roppolo, I.; Messori, M. UV-Cured Functional Coatings. *RSC Smart Materials* **2015**, *2015*, 121–133.
8. Sangermano, M.; Roppolo, I.; Chiappone, A. New Horizons in Cationic Photopolymerization. *Polymers* **2018**, *10*, doi:10.3390/polym10020136.
9. Felix, J.F.; Barros, R.A.; de Azevedo, W.M.; da Silva, E.F. X-Ray Irradiation: A Non-Conventional Route for the Synthesis of Conducting Polymers. *Synthetic Metals* **2011**, *161*, 173–176, doi:10.1016/j.synthmet.2010.11.017.
10. Yagci, Y.; Schnabel, W. New Aspects on the Photoinitiated Free Radical Promoted Cationic Polymerization. In Proceedings of the Makromolekulare Chemie. Macromolecular Symposia; Wiley Online Library, 1992; Vol. 60, pp. 133–143.

11. Chen, Z.; Wang, X.; Li, S.; Liu, S.; Miao, H.; Wu, S. Near-Infrared Light Driven Photopolymerization Based On Photon Upconversion. *ChemPhotoChem* **2019**, *3*, 1077–1083, doi:10.1002/cptc.201900007.

12. Neumann, M.G.; Miranda, W.G.; Schmitt, C.C.; Rueggeberg, F.A.; Correa, I.C. Molar Extinction Coefficients and the Photon Absorption Efficiency of Dental Photoinitiators and Light Curing Units. *Journal of Dentistry* **2005**, *33*, 525–532, doi:10.1016/j.jdent.2004.11.013.

13. Chen, Y.C.; Ferracane, J.L.; Prahl, S.A. Quantum Yield of Conversion of the Photoinitiator Camphorquinone. *Dental Materials* **2007**, *23*, 655–664, doi:10.1016/j.dental.2006.06.005.

14. Williams, J.L.R. Photopolymerization and Photocrosslinking of Polymers. In *Photochemistry*; Springer-Verlag: Berlin/Heidelberg, 2006; pp. 227–250.

15. Khudyakov, I. v. Fast Photopolymerization of Acrylate Coatings: Achievements and Problems. *Progress in Organic Coatings* **2018**, *121*, 151–159, doi:10.1016/j.porgcoat.2018.04.030.

16. Tiwari, A.; Polykarpov, A. *Photocured Materials*; Royal Society of Chemistry, 2014; ISBN 178262001X.

17. Crivello, J. v.; Lam, J.H.W. Diaryliodonium Salts. A New Class of Photoinitiators for Cationic Polymerization. *Macromolecules* **1977**, *10*, 1307–1315, doi:10.1021/ma60060a028.

18. Gomurashvili, Z.; Crivello, J. v. Phenothiazine Photosensitizers for Onium Salt Photoinitiated Cationic Polymerization. *Journal of Polymer Science, Part A: Polymer Chemistry* **2001**, *39*, 1187–1197, doi:10.1002/pola.1096.

19. Devoe, R.J.; Sahyun, M.R.V.; Serpone, N.; Siiarma, D.K. Transient Intermediates in the Photolysis of Iodonium Cations. *Canadian Journal of Chemistry* **1987**, *65*, 2342–2349, doi:10.1139/v87-391.

20. Bulut, U.; Crivello, J. v. Investigation of the Reactivity of Epoxide Monomers in Photoinitiated Cationic Polymerization. *Macromolecules* **2005**, *38*, 3584–3595, doi:10.1021/ma050106k.

21. Fouassier, J.P.; Burr, D.; Crivello, J. v. Photochemistry And Photopolymerization Activity Of Diaryliodonium Salts. *Journal of Macromolecular Science, Part A* **1994**, *31*, 677–701, doi:10.1080/10601329408545306.

22. Yağci, Y.; Ledwith, A. Mechanistic and Kinetic Studies on the Photoinitiated Polymerization of Tetrahydrofuran. *Journal of Polymer Science Part A: Polymer Chemistry* **1988**, *26*, 1911–1918.

23. Nelson, E.W.; Carter, T.P.; Scranton, A.B. The Role of the Triplet State in the Photosensitization of Cationic Polymerizations by Anthracene. *Journal of Polymer Science Part A: Polymer Chemistry* **1995**, *33*, 247–256.

24. Crivello, J. v; Lee, J.L. Photosensitized Cationic Polymerizations Using Dialkylphenacylsulfonium and Dialkyl (4-Hydroxyphenyl) Sulfonium Salt Photoinitiators. *Macromolecules* **1981**, *14*, 1141–1147.

25. Yagci, Y.; Schnabel, W.; Wilpert, A.; Bendig, J. Electron Transfer from Aromatic Compounds to Phenyliodinium and Diphenylsulfinium Radical Cations. *Journal of the Chemical Society, Faraday Transactions* **1994**, *90*, 287–291.

26. Hizal, G.; Yagci, Y.; Schnabel, W. Charge-Transfer Complexes of Pyridinium Ions and Methyl- and Methoxy-Substituted Benzenes as Photoinitiators for the Cationic Polymerization of Cyclohexene Oxide and Related Compounds. *Polymer* **1994**, *35*, 2428–2431, doi:10.1016/0032-3861(94)90783-8.

27. Hizal, G.; Emiroglu, S.E.; Yagci, Y. Photoinitiated Radical Polymerization Using Charge Transfer Complex of N-ethoxy-p-cyanopyridinium Salt and 1,2,4-trimethoxybenzene. *Polymer International* **1998**, *47*, 391–392, doi:10.1002/(sici)1097-0126(199812)47:4<391::aid-pi114>3.3.co;2-r.

28. Crivello, J. v.; Lam, J.H.W. Photoinitiated Cationic Polymerization By Dialkylphenacylsulfonium Salts. *Journal of polymer science. Part A-1, Polymer chemistry* **1979**, *17*, 2877–2892, doi:10.1002/pol.1979.170170924.

29. Yagci, Y.; Durmaz, Y.Y.; Aydogan, B. Phenacyl Onium Salt Photoinitiators: Synthesis, Photolysis, and Applications. *Chemical Record* **2007**, *7*, 78–90, doi:10.1002/tcr.20110.

30. Yağci, Y.; Kornowski, A.; Schnabel, W. N-alkoxy-pyridinium and N-alkoxy-quinolinium Salts as Initiators for Cationic Photopolymerizations. *Journal of Polymer Science Part A: Polymer Chemistry* **1992**, *30*, 1987–1991, doi:10.1002/pola.1992.080300922.

31. Abdallah, M.; Magaldi, D.; Hijazi, A.; Graff, B.; Dumur, F.; Fouassier, J.P.; Bui, T.T.; Goubard, F.; Lalevée, J. Development of New High-Performance Visible Light Photoinitiators Based on Carbazole Scaffold and Their Applications in 3d Printing and Photocomposite Synthesis. *Journal of Polymer Science, Part A: Polymer Chemistry* 2019, *57*, 2081–2092.

32. Hola, E.; Topa, M.; Chachaj-Brekiesz, A.; Pilch, M.; Fiedor, P.; Galek, M.; Ortyl, J. New, Highly Versatile Bimolecular Photoinitiating Systems for Free-Radical, Cationic and Thiol-Ene Photopolymerization Processes under Low Light Intensity UV and Visible LEDs for 3D Printing Application. *RSC Advances* **2020**, *10*, 7509–7522, doi:10.1039/c9ra10212d.

33. Breloy, L.; Brezová, V.; Blacha-Grzechnik, A.; Presset, M.; Yildirim, M.S.; Yilmaz, I.; Yagci, Y.; Versace, D.L. Visible Light Anthraquinone Functional Phthalocyanine Photoinitiator for Free-Radical and Cationic

Polymerizations. *Macromolecules* **2020**, *53*, 112–124, doi:10.1021/acs.macromol.9b01630.

34. Shi, S.; Croutxé-Barghorn, C.; Allonas, X. Photoinitiating Systems for Cationic Photopolymerization: Ongoing Push toward Long Wavelengths and Low Light Intensities. *Progress in Polymer Science* **2017**, *65*, 1–41, doi:10.1016/j.progpolymsci.2016.09.007.

35. Zhang, J.; Xiao, P.; Dietlin, C.; Campolo, D.; Dumur, F.; Gigmes, D.; Morlet-Savary, F.; Fouassier, J.P.; Lalevée, J. Cationic Photoinitiators for Near UV and Visible LEDs: A Particular Insight into One-Component Systems. *Macromolecular Chemistry and Physics* **2016**, *217*, 1214–1227, doi:10.1002/macp.201500546.

36. Sangermano, M. Recent Advances in Cationic Photopolymerization. *Journal of Photopolymer Science and Technology* **2019**, *32*, 233–236.

37. Sangermano, M.; Malucelli, G.; Morel, F.; Decker, C.; Priola, A. Cationic Photopolymerization of Vinyl Ether Systems: Influence of the Presence of Hydrogen Donor Additives. *European Polymer Journal* **1999**, *35*, 639–645, doi:10.1016/S0014-3057(98)00168-2.

38. Crivello, J. v.; Liu, S. Photoinitiated Cationic Polymerization of Epoxy Alcohol Monomers. *Journal of Polymer Science Part A: Polymer Chemistry* **2000**, *38*, 389–401, doi:10.1002/(SICI)1099-0518(20000201)38:3<389::AID-POLA1>3.0.CO;2-G.

39. Crivello, J. v.; Bi, D.; Lu, Y. Cationic Photopolymerization of Ambifunctional Monomers. *Macromolecular Symposia* **1995**, *95*, 79–89, doi:10.1002/masy.19950950109.

40. Sangermano, M. UV-Cured Nanostructured Epoxy Coatings. In *Epoxy Polymers*; Wiley-VCH Verlag GmbH & Co. KGaA: Weinheim, Germany, 2010; pp. 235–251 ISBN 9783527324804.

41. Sangermano, M.; Pegel, S.; Pötschke, P.; Voit, B. Antistatic Epoxy Coatings with Carbon Nanotubes Obtained by Cationic Photopolymerization. *Macromolecular Rapid Communications* **2008**, *29*, 396–400, doi:10.1002/marc.200700720.

42. Sangermano, M.; Voit, B.; Sordo, F.; Eichhorn, K.J.; Rizza, G. High Refractive Index Transparent Coatings Obtained via UV/Thermal Dual-Cure Process. *Polymer* **2008**, *49*, 2018–2022, doi:10.1016/j.polymer.2008.03.010.

43. Sangermano, M.; Messori, M. Scratch Resistance Enhancement of Polymer Coatings. *Macromolecular Materials and Engineering* **2010**, *295*, 603–612, doi:10.1002/mame.201000025.

44. Sangermano, M.; Yagci, Y.; Rizza, G. In Situ Synthesis of Silver-Epoxy Nanocomposites by Photoinduced Electron Transfer and Cationic

Polymerization Processes. *Macromolecules* **2007**, *40*, 8827–8829, doi:10.1021/ma702051g.

45. Yagci, Y.; Sangermano, M.; Rizza, G. Synthesis and Characterization of Gold - Epoxy Nanocomposites by Visible Light Photoinduced Electron Transfer and Cationic Polymerization Processes. *Macromolecules* **2008**, *41*, 7268–7270, doi:10.1021/ma801776y.

46. Yagci, Y.; Sangermano, M.; Rizza, G. A Visible Light Photochemical Route to Silver–Epoxy Nanocomposites by Simultaneous Polymerization–Reduction Approach. *Polymer* **2008**, *49*, 5195–5198, doi:10.1016/j.polymer.2008.09.068.

47. Sangermano, M.; Borella, E.; Priola, A.; Messori, M.; Taurino, R.; Pötschke, P. Use of Single-Walled Carbon Nanotubes as Reinforcing Fillers in UV-Curable Epoxy Systems. *Macromolecular Materials and Engineering* **2008**, *293*, 708–713, doi:10.1002/mame.200800126.

48. Sangermano, M.; Messori, M.; Galleco, M.M.; Rizza, G.; Voit, B. Scratch Resistant Tough Nanocomposite Epoxy Coatings Based on Hyperbranched Polyesters. *Polymer* **2009**, *50*, 5647–5652, doi:10.1016/j.polymer.2009.10.009.

49. Sangermano, M.; Tonin, M.; Yagci, Y. Degradable Epoxy Coatings by Photoinitiated Cationic Copolymerization of Bisepoxide with ε-Caprolactone. *European Polymer Journal* **2010**, *46*, 254–259, doi:10.1016/j.eurpolymj.2009.10.023.

50. Miao, S.; Wang, P.; Su, Z.; Zhang, S. Vegetable-Oil-Based Polymers as Future Polymeric Biomaterials. *Acta Biomaterialia* **2014**, *10*, 1692–1704, doi:10.1016/j.actbio.2013.08.040.

51. Crivello, J. v.; Narayan, R. Epoxidized Triglycerides as Renewable Monomers in Photoinitiated Cationic Polymerization. *Chemistry of Materials* **1992**, *4*, 692–699, doi:10.1021/cm00021a036.

52. Behera, D.; Banthia, A.K. Synthesis, Characterization, and Kinetics Study of Thermal Decomposition of Epoxidized Soybean Oil Acrylate. *Journal of Applied Polymer Science* **2008**, *109*, 2583–2590, doi:10.1002/app.28350.

53. Yang, Z.; Peng, H.; Wang, W.; Liu, T. Biocomposites Composed of Epoxidized Soybean Oil Cured with Terpene-Based Acid Anhydride and Cellulose Fibers. *Journal of Applied Polymer Science* **2010**, *116*, 2658–2667, doi:10.1002/app.

54. Miyagawa, H.; Misra, M.; Drzal, L.T.; Mohanty, A.K. Fracture Toughness and Impact Strength of Anhydride-Cured Biobased Epoxy. *Polymer Engineering and Science* **2005**, *45*, 487–495, doi:10.1002/pen.20290.

55. Aluyor, E.O.; Obahiagbon, K. O., & Ori-Jesu, M. Biodegradation of Vegetable Oils: A Review. In *Scientific Research and Essays*; 2009; Vol. 4, pp. 543–548.

56. Hassan, B.; Chatha, S.A.S.; Hussain, A.I.; Zia, K.M.; Akhtar, N. Recent Advances on Polysaccharides, Lipids and Protein Based Edible Films and Coatings: A Review. *International Journal of Biological Macromolecules* **2018**, *109*, 1095–1107, doi:10.1016/j.ijbiomac.2017.11.097.

57. Dastpak, A.; Yliniemi, K.; Monteiro, M.C. de O.; Höhn, S.; Virtanen, S.; Lundström, M.; Wilson, B.P. From Waste to Valuable Resource: Lignin as a Sustainable Anti-Corrosion Coating. *Coatings* **2018**, *8*, doi:10.3390/COATINGS8120454.

58. Lacroix, M.; Tien, C. le Edible Films and Coat ~ Ngs Trom Non- Starch Polysaccharides. *Innovations in Food Packaging: Overiew* **2005**, 0–12, doi:10.1016/B978-0-12-311632-1.50052-8.

59. Athawale, V.D.; Lele, V. Graft Copolymerization onto Starch. II. Grafting of Acrylic Acid and Preparation of It's Hydrogels. *Carbohydrate Polymers* **1998**, *35*, 21–27, doi:10.1016/S0144-8617(97)00138-0.

60. Lee, J.S.; Kumar, R.N.; Rozman, H.D.; Azemi, B.M.N. Pasting, Swelling and Solubility Properties of UV Initiated Starch-Graft-Poly(AA). *Food Chemistry* **2005**, *91*, 203–211, doi:10.1016/j.foodchem.2003.08.032.

61. Saboktakin, M.R.; Maharramov, A.; Ramazanov, M.A. PH-Sensitive Starch Hydrogels via Free Radical Graft Copolymerization, Synthesis and Properties. *Carbohydrate Polymers* **2009**, *77*, 634–638, doi:10.1016/j.carbpol.2009.02.004.

62. Melilli, G.; Carmagnola, I.; Tonda-Turo, C.; Pirri, F.; Ciardelli, G.; Sangermano, M.; Hakkarainen, M.; Chiappone, A. DLP 3D Printing Meets Lignocellulosic Biopolymers: Carboxymethyl Cellulose Inks for 3D Biocompatible Hydrogels. *Polymers* **2020**, *12*, 1–11, doi:10.3390/POLYM12081655.

63. Han, T.L.; Kumar, R.N.; Rozman, H.D.; Noor, M.A.M. GMA Grafted Sago Starch as a Reactive Component in Ultra Violet Radiation Curable Coatings. *Carbohydrate Polymers* **2003**, *54*, 509–516, doi:10.1016/j.carbpol.2003.08.001.

64. Cho, J.K.; Lee, J.S.; Jeong, J.; Kim, B.; Kim, B.; Kim, S.; Shin, S.; Kim, H.J.; Lee, S.H. Synthesis of Carbohydrate Biomass-Based Furanic Compounds Bearing Epoxide End Group(s) and Evaluation of Their Feasibility as Adhesives. *Journal of Adhesion Science and Technology* **2013**, *27*, 2127–2138, doi:10.1080/01694243.2012.697700.

65. Nameer, S.; Larsen, D.B.; Duus, J.O.; Daugaard, A.E.; Johansson, M. Biobased Cationically Polymerizable Epoxy Thermosets from Furan and

Fatty Acid Derivatives. *ACS Sustainable Chemistry and Engineering* **2018**, *6*, 9442–9450, doi:10.1021/acssuschemeng.8b01817.

66. Alsulami, Q.A.; Albukhari, S.M.; Hussein, M.A.; Tay, G.S.; Rozman, H.D. Biodegradable Lignin as a Reactive Raw Material in UV Curable Systems. *Polymer-Plastics Technology and Materials* **2020**, *59*, 1387–1406, doi:10.1080/25740881.2020.1750649.

67. Yan, R.; Yang, D.; Zhang, N.; Zhao, Q.; Liu, B.; Xiang, W.; Sun, Z.; Xu, R.; Zhang, M.; Hu, W. Performance of UV Curable Lignin Based Epoxy Acrylate Coatings. *Progress in Organic Coatings* **2018**, *116*, 83–89, doi:10.1016/j.porgcoat.2017.11.011.

68. Hajirahimkhan, S.; Xu, C.C.; Ragogna, P.J. Ultraviolet Curable Coatings of Modified Lignin. *ACS Sustainable Chemistry and Engineering* **2018**, *6*, 14685–14694, doi:10.1021/acssuschemeng.8b03252.

69. Pezzana, L.; Malmström, E.; Johansson, M.; Sangermano, M. Uv-Curable Bio-Based Polymers Derived from Industrial Pulp and Paper Processes. *Polymers* **2021**, *13*, doi:10.3390/polym13091530.

70. Wang, S.; Ma, S.; Xu, C.; Liu, Y.; Dai, J.; Wang, Z.; Liu, X.; Chen, J.; Shen, X.; Wei, J.; et al. Vanillin-Derived High-Performance Flame Retardant Epoxy Resins: Facile Synthesis and Properties. *Macromolecules* **2017**, *50*, 1892–1901, doi:10.1021/acs.macromol.7b00097.

71. Navaruckiene, A.; Skliutas, E.; Kasetaite, S.; Rekštyte, S.; Raudoniene, V.; Bridziuviene, D.; Malinauskas, M.; Ostrauskaite, J. Vanillin Acrylate-Based Resins for Optical 3D Printing. *Polymers* **2020**, *12*, doi:10.3390/polym12020397.

72. Steinmetz, Z.; Kurtz, M.P.; Zubrod, J.P.; Meyer, A.H.; Elsner, M.; Schaumann, G.E. Biodegradation and Photooxidation of Phenolic Compounds in Soil—A Compound-Specific Stable Isotope Approach. *Chemosphere* **2019**, *230*, 210–218, doi:10.1016/j.chemosphere.2019.05.030.

73. Fitzgerald, D.J.; Stratford, M.; Gasson, M.J.; Ueckert, J.; Bos, A.; Narbad, A. Mode of Antimicrobial of Vanillin against Escherichia Coli, Lactobacillus Plantarum and Listeria Innocua. *Journal of Applied Microbiology* **2004**, *97*, 104–113, doi:10.1111/j.1365-2672.2004.02275.x.

74. Crivello, J. v.; Yang, B. Studies of Synthesis and Cationic Photopolymerization of Three Isomeric Monoterpene Diepoxides. *Journal of Polymer Science Part A: Polymer Chemistry* **1995**, *33*, 1881–1890, doi:10.1002/pola.1995.080331116.

75. Han Jin Park, Chang Y. Ryu, J.V.C. Photoinitiated Cationic Polymerization of Limonene 1,2-oxide and A-pinene Oxide.

76. Breloy, L.; Ouarabi, C.A.; Brosseau, A.; Dubot, P.; Brezova, V.; Abbad Andaloussi, S.; Malval, J.-P.; Versace, D.-L. β-Carotene/Limonene Derivatives/Eugenol: Green Synthesis of Antibacterial Coatings under Visible-Light Exposure. *ACS Sustainable Chemistry & Engineering* **2019**, *7*, 19591–19604, doi:10.1021/acssuschemeng.9b04686.

77. Acosta Ortiz, R.; García Valdez, A.E.; Hernández Cruz, D.; Nestoso Jiménez, G.; Hernández Jiménez, A.I.; Téllez Padilla, J.G.; Guerrero Santos, R. Highly Reactive Novel Biobased Cycloaliphatic Epoxy Resins Derived from Nopol and a Study of Their Cationic Photopolymerization. *Journal of Polymer Research* **2020**, *27*, doi:10.1007/s10965-020-02106-4.

78. Aggarwal, L.K.; Thapliyal, P.C.; Karade, S.R. Anticorrosive Properties of the Epoxy-Cardanol Resin Based Paints. *Progress in Organic Coatings* **2007**, doi:10.1016/j.porgcoat.2007.01.010.

79. Chen, Z.; Chisholm, B.J.; Webster, D.C.; Zhang, Y.; Patel, S. Study of Epoxidized-Cardanol Containing Cationic UV Curable Materials. *Progress in Organic Coatings* **2009**, *65*, 246–250, doi:10.1016/j.porgcoat.2008.11.008.

80. Zou, Y.; Zhang, L.; Yang, L.; Zhu, F.; Ding, M.; Lin, F.; Wang, Z.; Li, Y. "Click" Chemistry in Polymeric Scaffolds: Bioactive Materials for Tissue Engineering. *Journal of Controlled Release* **2018**, *273*, 160–179, doi:10.1016/j.jconrel.2018.01.023.

81. Wang, C.; Wang, D.; Dai, T.; Xu, P.; Wu, P.; Zou, Y.; Yang, P.; Hu, J.; Li, Y.; Cheng, Y. Skin Pigmentation-Inspired Polydopamine Sunscreens. *Advanced Functional Materials* **2018**, *28*, doi:10.1002/adfm.201802127.

82. Li, M.; Wang, H.; Hu, J.; Hu, J.; Zhang, S.; Yang, Z.; Li, Y.; Cheng, Y. Smart Hydrogels with Antibacterial Properties Built from All Natural Building Blocks. *Chemistry of Materials* **2019**, *31*, 7678–7685, doi:10.1021/acs.chemmater.9b02547.

83. van Vlierberghe, S.; Dubruel, P.; Schacht, E. Biopolymer-Based Hydrogels as Scaffolds for Tissue Engineering Applications: A Review. *Biomacromolecules* **2011**, *12*, 1387–1408, doi:10.1021/bm200083n.

84. Peppas, N.A.; Bures, P.; Leobandung, W.; Ichikawa, H. Hydrogels in Pharmaceutical Formulations. *European Journal of Pharmaceutics and Biopharmaceutics* **2000**, *50*, 27–46, doi:10.1016/S0939-6411(00)00090-4.

85. Piluso, S.; Labet, M.; Zhou, C.; Seo, J.W.; Thielemans, W.; Patterson, J. Engineered Three-Dimensional Microenvironments with Starch Nanocrystals as Cell-Instructive Materials. *Biomacromolecules* **2019**, *20*, 3819–3830, doi:10.1021/acs.biomac.9b00907.

86. Feng, Z.; Danjo, T.; Odelius, K.; Hakkarainen, M.; Iwata, T.; Albertsson, A.C. Recyclable Fully Biobased Chitosan Adsorbents Spray-Dried in One

Pot to Microscopic Size and Enhanced Adsorption Capacity. *Biomacromolecules* **2019**, *20*, 1956–1964, doi:10.1021/acs.biomac.9b00186.

87. Zhang, X.; Morits, M.; Jonkergouw, C.; Ora, A.; Valle-Delgado, J.J.; Farooq, M.; Ajdary, R.; Huan, S.; Linder, M.; Rojas, O.; et al. Three-Dimensional Printed Cell Culture Model Based on Spherical Colloidal Lignin Particles and Cellulose Nanofibril-Alginate Hydrogel. *Biomacromolecules* **2020**, doi:10.1021/acs.biomac.9b01745.

88. van Nieuwenhove, I.; Salamon, A.; Adam, S.; Dubruel, P.; van Vlierberghe, S.; Peters, K. Gelatin- and Starch-Based Hydrogels. Part B: In Vitro Mesenchymal Stem Cell Behavior on the Hydrogels. *Carbohydrate Polymers* **2017**, *161*, 295–305, doi:10.1016/j.carbpol.2017.01.010.

89. Lawal, O.S.; Storz, J.; Storz, H.; Lohmann, D.; Lechner, D.; Kulicke, W.M. Hydrogels Based on Carboxymethyl Cassava Starch Cross-Linked with Di- or Polyfunctional Carboxylic Acids: Synthesis, Water Absorbent Behavior and Rheological Characterizations. *European Polymer Journal* **2009**, *45*, 3399–3408, doi:10.1016/j.eurpolymj.2009.09.019.

90. Uddin, M.T.; Islam, M.A.; Mahmud, S.; Rukanuzzaman, M. Adsorptive Removal of Methylene Blue by Tea Waste. *Journal of Hazardous Materials* **2009**, *164*, 53–60, doi:10.1016/j.jhazmat.2008.07.131.

91. Ho, Y.S.; McKay, G. Pseudo-Second Order Model for Sorption Processes. *Process Biochemistry* **1999**, *34*, 451–465, doi:10.1016/S0032-9592(98)00112-5.

92. Noè, C.; Tonda-Turo, C.; Chiappone, A.; Sangermano, M.; Hakkarainen, M. Light Processable Starch Hydrogels. *Polymers* **2020**, *12*, 1359, doi:10.3390/POLYM12061359.

93. Wu, D.; Samanta, A.; Srivastava, R.K.; Hakkarainen, M. Starch-Derived Nanographene Oxide Paves the Way for Electrospinnable and Bioactive Starch Scaffolds for Bone Tissue Engineering. *Biomacromolecules* **2017**, *18*, 1582–1591, doi:10.1021/acs.biomac.7b00195.

94. Hedin, J.; Östlund, Å.; Nydén, M. UV Induced Cross-Linking of Starch Modified with Glycidyl Methacrylate. *Carbohydrate Polymers* **2010**, *79*, 606–613, doi:10.1016/j.carbpol.2009.09.019.

95. Kizil, R.; Irudayaraj, J.; Seetharaman, K. Characterization of Irradiated Starches by Using FT-Raman and FTIR Spectroscopy. *Journal of Agricultural and Food Chemistry* **2002**, *50*, 3912–3918, doi:10.1021/jf011652p.

96. Wu, D.; Hakkarainen, M. A Closed-Loop Process from Microwave-Assisted Hydrothermal Degradation of Starch to Utilization of the Obtained

Degradation Products as Starch Plasticizers. *ACS Sustainable Chemistry and Engineering* **2014**, *2*, 2172–2181, doi:10.1021/sc500355w.

97. Reis, A. v; Guilherme, M.R.; Moia, T.A.; Mattoso, L.H.C.; Muniz, E.C.; Tambourgi, E.B. Synthesis and Characterization of a Starch-Modified Hydrogel as Potential Carrier for Drug Delivery System. *Journal of Polymer Science Part A: Polymer Chemistry* **2008**, *46*, 2567–2574, doi:10.1002/pola.22588.

98. Bayramoglu, G. Methacrylated Chitosan Based UV Curable Support for Enzyme Immobilization. *Materials Research* **2017**, *20*, 452–459, doi:10.1590/1980-5373-MR-2016-0789.

99. Hajirahimkhan, S.; Ragogna, P.J.; Xu, C. (Charles) Methacrylation of Kraft Lignin for UV-Curable Coatings: Process Optimization Using Response Surface Methodology. *Biomass and Bioenergy* **2019**, *120*, 332–338, doi:10.1016/j.biombioe.2018.11.038.

100. Han, F.; Zhu, C.; Guo, Q.; Yang, H.; Li, B. Cellular Modulation by the Elasticity of Biomaterials. *Journal of Materials Chemistry B* **2016**, *4*, 9–26, doi:10.1039/c5tb02077h.

101. Seidel, C.; Kulicke, W.M.; Heß, C.; Hartmann, B.; Lechner, M.D.; Lazik, W. Synthesis and Characterization of Cross-Linked Carboxymethyl Potato Starch Ether Gels. *Starch/Staerke* **2004**, *56*, 157–166, doi:10.1002/star.200200165.

102. Seidel, C.; Kulicke, W.M.; Heß, C.; Hartmann, B.; Lechner, M.D.; Lazik, W. Influence of the Cross-Linking Agent on the Gel Structure of Starch Derivatives. *Starch/Staerke* **2001**, *53*, 305–310, doi:10.1002/1521-379X(200107)53:7<305::AID-STAR305>3.0.CO;2-Z.

103. Kowalski, G.; Ptaszek, P. The Effect of Swelling Time on Rheological Properties of Hydrogels, Consisting of High -Amylose Carboxymethyl Corn Starch and Acrylic Polymers. *Starch/Staerke* **2016**, *68*, 381–388, doi:10.1002/star.201400253.

104. Frascella, F.; González, G.; Bosch, P.; Angelini, A.; Chiappone, A.; Sangermano, M.; Pirri, C.F.; Roppolo, I. Three-Dimensional Printed Photoluminescent Polymeric Waveguides. *ACS Applied Materials & Interfaces* **2018**, *10*, 39319–39326, doi:10.1021/acsami.8b16036.

105. Noè, C.; Cosola, A.; Chiappone, A.; Hakkarainen, M.; Grützmacher, H.; Sangermano, M. From Polysaccharides to UV-Curable Biorenewable Organo/Hydrogels for Methylene Blue Removal. *Polymer* **2021**, *235*, doi:10.1016/j.polymer.2021.124257.

106. Cosola, A.; Conti, R.; Grützmacher, H.; Sangermano, M.; Roppolo, I.; Pirri, C.F.; Chiappone, A. Multiacrylated Cyclodextrin: A Bio-Derived

Photocurable Macromer for VAT 3D Printing. *Macromolecular Materials and Engineering* **2020**, *305*, 1–6, doi:10.1002/mame.202000350.

107. Nielsen, L.E. Cross-Linking–Effect on Physical Properties of Polymers. *Journal of Macromolecular Science, Part C* **1969**, *3*, 69–103, doi:10.1080/15583726908545897.

108. Ceccaldi, C.; Fullana, S.G.; Alfarano, C.; Lairez, O.; Calise, D.; Cussac, D.; Parini, A.; Sallerin, B. Alginate Scaffolds for Mesenchymal Stem Cell Cardiac Therapy: Influence of Alginate Composition. *Cell Transplantation* **2012**, *21*, 1969–1984, doi:10.3727/096368912X647252.

109. Ren, F.; Li, Z.; Tan, W.Z.; Liu, X.H.; Sun, Z.F.; Ren, P.G.; Yan, D.X. Facile Preparation of 3D Regenerated Cellulose/Graphene Oxide Composite Aerogel with High-Efficiency Adsorption towards Methylene Blue. *Journal of Colloid and Interface Science* **2018**, *532*, 58–67, doi:10.1016/j.jcis.2018.07.101.

110. Liu, J.; Chu, H.; Wei, H.; Zhu, H.; Wang, G.; Zhu, J.; He, J. Facile Fabrication of Carboxymethyl Cellulose Sodium/Graphene Oxide Hydrogel Microparticles for Water Purification. *RSC Advances* **2016**, *6*, 50061–50069, doi:10.1039/c6ra06438h.

111. Yao, J.; Odelius, K.; Hakkarainen, M. Carbonized Lignosulfonate-Based Porous Nanocomposites for Adsorption of Environmental Contaminants. *Functional Composite Materials* **2020**, *1*, 1–12, doi:10.1186/s42252-020-00008-8.

112. Ma, D.; Zhu, B.; Cao, B.; Wang, J.; Zhang, J. Fabrication of the Novel Hydrogel Based on Waste Corn Stalk for Removal of Methylene Blue Dye from Aqueous Solution. *Applied Surface Science* **2017**, *422*, 944–952, doi:10.1016/j.apsusc.2017.06.072.

113. Jeon, Y.S.; Lei, J.; Kim, J.H. Dye Adsorption Characteristics of Alginate/Polyaspartate Hydrogels. *Journal of Industrial and Engineering Chemistry* **2008**, *14*, 726–731, doi:10.1016/j.jiec.2008.07.007.

114. Ersali, S.; Hadadi, V.; Moradi, O.; Fakhri, A. Pseudo-Second-Order Kinetic Equations for Modeling Adsorption Systems for Removal of Ammonium Ions Using Multi-Walled Carbon Nanotube. *Fullerenes, Nanotubes and Carbon Nanostructures* **2013**, 150527104639002, doi:10.1080/1536383x.2013.787610.

115. Raquez, J.M.; Deléglise, M.; Lacrampe, M.F.; Krawczak, P. Thermosetting (Bio)Materials Derived from Renewable Resources: A Critical Review. *Progress in Polymer Science (Oxford)* **2010**, *35*, 487–509, doi:10.1016/j.progpolymsci.2010.01.001.

116. Auvergne, R.; Caillol, S.; David, G.; Boutevin, B.; Pascault, J.P. Biobased Thermosetting Epoxy: Present and Future. *Chemical Reviews* **2014**, *114*, 1082–1115, doi:10.1021/cr3001274.

117. Flory, P.J. Molecular Theory of Rubber Elasticity. *Polymer Journal* **1985**, *17*, 1–12, doi:10.1295/polymj.17.1.

118. Papadakis, V.G. Estimation of Estimation of Surface Free Energy of Polymres. *Journal of Applied Polymer Science* **1969**, *13*, 1741–1747.

119. Hasan, W. Rheological Characterization of Vegetable Oil Blends : Effect of Shear Rate , Temperature , and Short-Term Heating. *J Food Process Eng.* **2020**, doi:10.1111/jfpe.13396.

120. ASTM International Standard Test Method for Film Hardness by Pencil Test 1. *ASTM D3363–05 Standard* 2010, *05*, 5–7.

121. Coatings, C.; Products, R.C.; Applica-, E.; Tape, S.; Paint, T.; Materials, R. Standard Test Methods for Measuring Adhesion by Tape Test 1 2012, 1–8.

122. Means, S.; Metals, F.; Coat-, N. Standard Practice for Assessing the Solvent Resistance of Organic Coatings Using Solvent Rubs 1 2015, *i*, 1–5.

123. Iannucci, L.; Parvis, M.; di Francia, E.; Grassini, S. IHomeX: An Internet-Enabled Laboratory for Long-Term Experiment Management. *IEEE Transactions on Instrumentation and Measurement* **2018**, *67*, 1142–1149, doi:10.1109/TIM.2017.2786740.

124. Noè, C.; Malburet, S.; Bouvet-Marchand, A.; Graillot, A.; Loubat, C.; Sangermano, M. Cationic Photopolymerization of Bio-Renewable Epoxidized Monomers. *Progress in Organic Coatings* **2019**, *133*, 131–138, doi:10.1016/j.porgcoat.2019.03.054.

125. Nielsen, L.E.; Landel, R.F. *Mechanical Properties of Polymers and Composites, Second Edition, Revised and Expanded*; 1993; ISBN 9781482277432.

126. Ranoux, G.; Molinari, M.; Coqueret, X. Thermo-Mechanical Properties and Structural Features of Diglycidyl Ether of BIS Phenol a Cationically Cured by Electron Beam Radiation. *Radiation Physics and Chemistry* **2012**, *81*, 1297–1302, doi:10.1016/j.radphyschem.2011.12.009.

127. Noè, C.; Malburet, S.; Milani, E.; Bouvet-Marchand, A.; Graillot, A.; Sangermano, M. Cationic UV-Curing of Epoxidized Cardanol Derivatives. *Polymer International* **2020**, doi:10.1002/pi.6031.

128. Caillol, S. Cardanol: A Promising Building Block for Biobased Polymers and Additives. *Current Opinion in Green and Sustainable Chemistry* **2018**, *14*, 26–32, doi:10.1016/j.cogsc.2018.05.002.

129. Malburet, S.; Mauro, D.; Noè, C.; Mija, A. Sustainable Access to Fully Biobased Epoxidized Vegetable Oil Thermoset Materials Prepared by Thermal or UV-Cationic Processes. *RSC Advances* **2020**, 41954–41966, doi:10.1039/d0ra07682a.

130. Shenoy, P.A.; Khot, S.S.; Chavan, M.C.; Takawale, J. v.; Singh, S. Study of Sunscreen Activity of Aqueous, Methanol and Acetone Extracts of Leaves of Pongamia Pinnata (L.) Pierre, Fabaceae. *International Journal of Green Pharmacy* **2010**, *4*, 270–274, doi:10.4103/0973-8258.74137.

131. Jin, F.; Park, S. Thermal Andd Rheological Properties of Vegetable Oil-Based Epoxy Resins with Thermally Latent Initiator. **2007**.

132. Tan, S.G.; Chow, W.S. Curing Characteristics and Thermal Properties of Epoxidized Soybean Oil Based Thermosetting Resin. *JAOCS, Journal of the American Oil Chemists' Society* **2011**, *88*, 915–923, doi:10.1007/s11746-010-1748-x.

133. Noè, C.; Iannucci, L.; Malburet, S.; Graillot, A.; Sangermano, M.; Grassini, S. New UV-Curable Anticorrosion Coatings from Vegetable Oils. *Macromolecular Materials and Engineering* **2021**, *2100029*, 2100029, doi:10.1002/mame.202100029.

134. Allen, C.A.W.; Watts, K.C.; Ackman, R.G.; Pegg, M.J. Predicting the Viscosity of Biodiesel Fuels from Their Fatty Acid Ester Composition. **1999**, *78*, 1319–1326.

135. Sinadinović-Fišer, S.; Janković, M.; Petrović, Z.S. Kinetics of in Situ Epoxidation of Soybean Oil in Bulk Catalyzed by Ion Exchange Resin. *JAOCS, Journal of the American Oil Chemists' Society* **2001**, *78*, 725–731, doi:10.1007/s11746-001-0333-9.

136. Yang, L.; Dai, H.; Yi, A.; Lin, B.; Li, G. Structure and Properties of Partially Epoxidized Soybean Oil. *Journal of Thermal Analysis and Calorimetry* **2008**, *93*, 875–879, doi:10.1007/s10973-008-9043-x.

137. Yan, M.; Frank, E.M.; Cochran, E.W. Effects of Vegetable Oil Composition on Epoxidation Kinetics and Physical Properties. *JAOCS, Journal of the American Oil Chemists' Society* **2018**, *95*, 209–216, doi:10.1002/aocs.12014.

138. Ng, F.; Couture, G.; Philippe, C.; Boutevin, B.; Caillol, S. Bio-Based Aromatic Epoxy Monomers for Thermoset Materials. *Molecules* **2017**, *22*, doi:10.3390/molecules22010149.

139. Marco Sangermano, Alexandre Perrot, Arnaud Gigot, Paola Rivolo, Fabrizio Pirri, M.M. Hydrophobic Scratch Resistant UV-Cured Epoxy Coating. *Macromol. Mater. Eng.* **2016**, *301*, 93–98, doi:10.1002/mame.20150023893.

140. Awaja, F.; Gilbert, M.; Kelly, G.; Fox, B.; Pigram, P.J. Adhesion of Polymers. *Progress in Polymer Science (Oxford)* **2009**, *34*, 948–968, doi:10.1016/j.progpolymsci.2009.04.007.

141. Amirudin, A.; Thierry, D. Application of Electrochemical Impedance Spectroscopy to Study the Atmospheric Corrosion of Painted Metals. *Materials Science Forum* **1995**, *192–194*, 317–334, doi:10.4028/www.scientific.net/msf.192-194.317.

142. Delville, J.; Joly, C.; Dole, P.; Bliard, C. Solid State Photocrosslinked Starch Based Films: A New Family of Homogeneous Modified Starches. *Carbohydrate Polymers* **2002**, *49*, 71–81, doi:10.1016/S0144-8617(01)00302-2.

143. Liu, X.; Lan, C.; Al, A.; Yu, L.; Zhou, S. Preparation of Cross-Linked High Amylose Corn-Starch and Its Effects on Self-Reinforced Starch Films. **2016**, *12*, 673–680, doi:10.1515/ijfe-2015-0139.

144. Detduangchan, N.; Wittaya, T. Effect of UV-Treatment on Properties of Biodegradable Film from Rice Starch. *World Academy of Science, Engineering and Technology* **2011**, *81*, 464–469.

145. Gadhave, R. v; Mahanwar, P.A.; Gadekar, P.T. Effect of Glutaraldehyde on Thermal and Mechanical Properties of Starch and Polyvinyl Alcohol Blends. *Designed Monomers and Polymers* **2019**, *22*, 164–170, doi:10.1080/15685551.2019.1678222.

146. Ma, S.; Jr, C.S.K.; Webster, D.C. Effect of Solvents on the Curing and Properties of Fully Bio-Based Thermosets for Coatings Effect of Solvents on the Curing and Properties of Fully Bio-Based Thermosets for Coatings. *Journal of Coatings Technology and Research* **2017**, doi:10.1007/s11998-016-9863-8.

147. Nelson, T.J.; Galhenage, T.P.; Webster, D.C. Catalyzed Crosslinking of Highly Functional Biobased Epoxy Resins Catalyzed Crosslinking of Highly Functional Biobased Epoxy Resins. *J. Coat. Technol. Res.* **2013**, *10*, 589–600, doi:10.1007/s11998-013-9488-0.

148. Dalvi, V.H.; Rossky, P.J. Molecular Origins of Fluorocarbon Hydrophobicity. *Proceedings of the National Academy of Sciences of the United States of America* **2010**, *107*, 13603–13607, doi:10.1073/pnas.0915169107.

149. Sagnelli; Cavanagh; Xu; Swainson; Blennow; Duncan; Taresco; Howdle Starch/Poly (Glycerol-Adipate) Nanocomposite Film as Novel Biocompatible Materials. *Coatings* **2019**, *9*, 482, doi:10.3390/coatings9080482.

150. Nawaz, M.A.; Pervez, S.; Jamal, M.; Jan, T.; Khan, W.; Rauf, A.; Aman, A.; Qader, S.A.U. Maltose Deterioration Approach: Catalytic Behavior

Optimization and Stability Profile of Maltase from Bacillus Licheniformis KIBGE-IB4. *Biotechnology Reports* **2019**, *24*, e00400, doi:10.1016/j.btre.2019.e00400.

151. Rajagopalan, G.; Krishnan, C. α-Amylase Production from Catabolite Derepressed Bacillus Subtilis KCC103 Utilizing Sugarcane Bagasse Hydrolysate. *Bioresource Technology* **2008**, *99*, 3044–3050, doi:10.1016/j.biortech.2007.06.001.

152. Scarponi, C.; Sarasini, F.; Tirillò, J.; Lampani, L.; Valente, T.; Gaudenzi, P. Low-Velocity Impact Behaviour of Hemp Fibre Reinforced Bio-Based Epoxy Laminates. *Composites Part B: Engineering* **2016**, *91*, 162–168, doi:10.1016/j.compositesb.2016.01.048.

153. Sobczak, L.; Lang, R.W.; Haider, A. Polypropylene Composites with Natural Fibers and Wood - General Mechanical Property Profiles. *Composites Science and Technology* **2012**, *72*, 550–557, doi:10.1016/j.compscitech.2011.12.013.

154. Alsubari, S.; Zuhri, M.Y.M.; Sapuan, S.M.; Ishak, M.R.; Ilyas, R.A.; Asyraf, M.R.M. Potential of Natural Fiber Reinforced Polymer Composites in Sandwich Structures: A Review on Its Mechanical Properties. *Polymers* **2021**, *13*, 423, doi:10.3390/polym13030423.

155. Mohanty, A.K.; Misra, M.; Drzal, L.T.; Selke, S.E.; Harte, B.R.; Hinrichsen, G. *Natural Fibers, Biopolymers, and Biocomposites*; Mohanty, A.K., Misra, M., Drzal, L.T., Eds.; CRC Press, 2005; ISBN 9780203508206.

156. Joshi, S. v.; Drzal, L.T.; Mohanty, A.K.; Arora, S. Are Natural Fiber Composites Environmentally Superior to Glass Fiber Reinforced Composites? *Composites Part A: Applied Science and Manufacturing* **2004**, *35*, 371–376, doi:10.1016/j.compositesa.2003.09.016.

157. Specimens, P.; Specimens, T. Standard Test Method for Tensile Properties of Plastics By Use of Microtensile. **2002**, *08*, 1–5, doi:10.1520/D1708-18.2.

158. Bryen, L.; Mcconachie, I.; Vock, N. Macadamia Variety Identifier. *Agriculture* **1998**.

159. Wilts, E.M.; Gula, A.; Davis, C.; Chartrain, N.; Williams, C.B.; Long, T.E. Vat Photopolymerization of Liquid, Biodegradable PLGA-Based Oligomers as Tissue Scaffolds. *European Polymer Journal* **2020**, *130*, 109693, doi:10.1016/j.eurpolymj.2020.109693.

160. Simon, G.P.; Allen, P.E.M.; Williams, D.R.G. Properties of Dimethacrylate Copolymers of Varying Crosslink Density. *Polymer* **1991**, *32*, 2577–2587, doi:10.1016/0032-3861(91)90337-I.

161. Savini, G.; Oréfice, R.L. Comparative Study of HDPE Composites Reinforced with Microtalc and Nanotalcs: High Performance Filler for

Improving Ductility at Low Concentration Levels. *Journal of Materials Research and Technology* **2020**, *9*, 16387–16398, doi:10.1016/j.jmrt.2020.11.090.

162. Zamani, Y.; Amoabediny, G.; Mohammadi, J.; Seddiqi, H.; Helder, M.N.; Zandieh-Doulabi, B.; Klein-Nulend, J.; Koolstra, J.H. 3D-Printed Poly(Ɛ-Caprolactone) Scaffold with Gradient Mechanical Properties According to Force Distribution in the Mandible for Mandibular Bone Tissue Engineering. *Journal of the Mechanical Behavior of Biomedical Materials* **2020**, *104*, 103638, doi:10.1016/j.jmbbm.2020.103638.

163. Wang, S.-F.; Wu, Y.-C.; Cheng, Y.-C.; Hu, W.-W. The Development of Polylactic Acid/Multi-Wall Carbon Nanotubes/Polyethylene Glycol Scaffolds for Bone Tissue Regeneration Application. *Polymers* **2021**, *13*, 1740, doi:10.3390/polym13111740.

164. Etemad-Shahidi, Y.; Qallandar, O.B.; Evenden, J.; Alifui-Segbaya, F.; Ahmed, K.E. Accuracy of 3-Dimensionally Printed Full-Arch Dental Models: A Systematic Review. *Journal of Clinical Medicine* **2020**, *9*, 1–18, doi:10.3390/jcm9103357.

165. Noè, C.; Hakkarainen, M.; Malburet, S.; Graillot, A.; Adekunle, K.; Skrifvars, M.; Sangermano, M. Frontal-Photopolymerization of Fully Biobased Epoxy Composites. *Macromolecular Materials and Engineering* **2022**, 2100864, doi:10.1002/mame.202100864.

166. Mariani, A.; Bidali, S.; Fiori, S.; Sangermano, M.; Malucelli, G.; Bongiovanni, R.; Priola, A. UV-Ignited Frontal Polymerization of an Epoxy Resin. *Journal of Polymer Science, Part A: Polymer Chemistry* **2004**, *42*, 2066–2072, doi:10.1002/pola.20051.

167. Malik, M.S.; Schlögl, S.; Wolfahrt, M.; Sangermano, M. Review on UV-Induced Cationic Frontal Polymerization of Epoxy Monomers. *Polymers* **2020**, *12*, 2146, doi:10.3390/POLYM12092146.

168. Goli, E.; Robertson, I.D.; Agarwal, H.; Pruitt, E.L.; Grolman, J.M.; Geubelle, P.H.; Moore, J.S. Frontal Polymerization Accelerated by Continuous Conductive Elements. *Journal of Applied Polymer Science* **2019**, *136*, 47418, doi:10.1002/app.47418.

169. Bomze, D.; Knaack, P.; Liska, R. Successful Radical Induced Cationic Frontal Polymerization of Epoxy-Based Monomers by C-C Labile Compounds. *Polymer Chemistry* **2015**, *6*, 8161–8167, doi:10.1039/c5py01451d.

170. Bomze, D.; Knaack, P.; Liska, R. Successful Radical Induced Cationic Frontal Polymerization of Epoxy-Based Monomers by C-C Labile Compounds. *Polymer Chemistry* **2015**, *6*, 8161–8167, doi:10.1039/c5py01451d.

171. Švajdlenková, H.; Kleinová, A.; Šauša, O.; Rusnák, J.; Dung, T.A.; Koch, T.; Knaack, P. Microstructural Study of Epoxy-Based Thermosets Prepared by "Classical" and Cationic Frontal Polymerization. *RSC Advances* **2020**, *10*, 41098–41109, doi:10.1039/d0ra08298h.

172. Bomze, D.; Knaack, P.; Koch, T.; Jin, H.; Liska, R. Radical Induced Cationic Frontal Polymerization as a Versatile Tool for Epoxy Curing and Composite Production. *Journal of Polymer Science, Part A: Polymer Chemistry* **2016**, *54*, 3751–3759, doi:10.1002/pola.28274.

173. Cherdoud-Chihani, A.; Mouzali, M.; Abadie, M.J.M. Study of Crosslinking AMS/DGEBA System by FTIR. *Journal of Applied Polymer Science* **1998**, *69*, 1167–1178, doi:10.1002/(sici)1097-4628(19980808)69:6<1167::aid-app14>3.0.co;2-q.

174. Hu, Y.; Shang, Q.; Wang, C.; Feng, G.; Liu, C.; Xu, F.; Zhou, Y. Renewable Epoxidized Cardanol-Based Acrylate as a Reactive Diluent for UV-Curable Resins. *Polymers for Advanced Technologies* **2018**, *29*, 1852–1860, doi:10.1002/pat.4294.

175. Ruiz De Luzuriaga, A.; Martin, R.; Markaide, N.; Rekondo, A.; Cabañero, G.; Rodríguez, J.; Odriozola, I. Epoxy Resin with Exchangeable Disulfide Crosslinks to Obtain Reprocessable, Repairable and Recyclable Fiber-Reinforced Thermoset Composites. *Materials Horizons* **2016**, *3*, 241–247, doi:10.1039/c6mh00029k.

176. Hassan, A.; Rahman, N.A.; Yahya, R. Moisture Absorption Effect on Thermal, Dynamic Mechanical and Mechanical Properties of Injection-Molded Short Glass-Fiber/Polyamide 6,6 Composites. *Fibers and Polymers* **2012**, *13*, 899–906, doi:10.1007/s12221-012-0899-9.

177. Costa, C.S.M.F.; Fonseca, A.C.; Serra, A.C.; Coelho, J.F.J. Dynamic Mechanical Thermal Analysis of Polymer Composites Reinforced with Natural Fibers. *Polymer Reviews* **2016**, *56*, 362–383, doi:10.1080/15583724.2015.1108334.

178. Ratim, S.; Bonnia, N.N.; Surip, N.S. The Effect of Woven and Non-Woven Fiber Structure on Mechanical Properties Polyester Composite Reinforced Kenaf. *AIP Conference Proceedings* **2012**, *1455*, 131–135, doi:10.1063/1.4732481.

179. Indra Reddy, M.; Anil Kumar, M.; Rama Bhadri Raju, C. Tensile and Flexural Properties of Jute, Pineapple Leaf and Glass Fiber Reinforced Polymer Matrix Hybrid Composites. *Materials Today: Proceedings* **2018**, *5*, 458–462, doi:10.1016/j.matpr.2017.11.105.

180. Saba, N.; Alothman, O.Y.; Almutairi, Z.; Jawaid, M. Magnesium Hydroxide Reinforced Kenaf Fibers/Epoxy Hybrid Composites: Mechanical and

Thermomechanical Properties. *Construction and Building Materials* **2019**, *201*, 138–148, doi:10.1016/j.conbuildmat.2018.12.182.

181. Chaudhary, V.; Bajpai, P.K.; Maheshwari, S. Studies on Mechanical and Morphological Characterization of Developed Jute/Hemp/Flax Reinforced Hybrid Composites for Structural Applications. *Journal of Natural Fibers* **2018**, *15*, 80–97, doi:10.1080/15440478.2017.1320260.

182. Sekaran, A.S.J.; Kumar, K.P.; Pitchandi, K. Evaluation on Mechanical Properties of Woven Aloevera and Sisal Fibre. **2015**, *38*, 1183–1193.

183. Shrivastava, R.; Telang, A.; Rana, R.S.; Purohit, R. Mechanical Properties of Coir/ G Lass Fiber Epoxy Resin Hybrid Composite. *Materials Today: Proceedings* **2017**, *4*, 3477–3483, doi:10.1016/j.matpr.2017.02.237.

184. Sumesh, K.R.; Kanthavel, K.; Kavimani, V. Peanut Oil Cake-Derived Cellulose Fiber: Extraction, Application of Mechanical and Thermal Properties in Pineapple/Flax Natural Fiber Composites. *International Journal of Biological Macromolecules* **2020**, *150*, 775–785, doi:10.1016/j.ijbiomac.2020.02.118.

185. Wells, J.K.; Beaumont, P.W.R. Debonding and Pull-out Processes in Fibrous Composites. *Journal of Materials Science* **1985**, *20*, 1275–1284, doi:10.1007/BF01026323.